

MASTER OF SCIENCE THESIS

# Effects of Defects in Thermoplastic Composite Pipes

The Assessment of Mechanical Performance Reduction  
due to Manufacturing-Induced Defects in Thermoplastic  
Composite Pipes

**D.A. Smit**

Faculty of Aerospace Engineering · Delft University of Technology





# **Effects of Defects in Thermoplastic Composite Pipes**

**The Assessment of Mechanical Performance Reduction due to  
Manufacturing-Induced Defects in Thermoplastic Composite Pipes**

MASTER OF SCIENCE THESIS

For obtaining the degree of Master of Science in Aerospace Engineering  
at Delft University of Technology

D.A. Smit

20 July 2020

The work in this thesis was supported by Airborne Oil and Gas. Their cooperation is gratefully acknowledged.



Copyright © D.A. Smit  
All rights reserved.





DELFT UNIVERSITY OF TECHNOLOGY  
FACULTY OF AEROSPACE ENGINEERING  
DEPARTMENT OF AEROSPACE STRUCTURES AND MATERIALS

**GRADUATION COMMITTEE**

Dated: 20 July 2020

Chair holder:

---

Prof. dr. ir. Clemens A. Dransfeld

Committee members:

---

Ir. Jos Sinke

---

Dr. ir. Otto K. Bergsma

---

Dr. ir. A.P.D. Weustink



“Projects we have completed demonstrate what we know - future projects decide what we will learn.”

— *Mohsin Tiwana*



---

# Preface

The thesis you have in front of you is the result of my research in combination with a literature study for obtaining the degree of Master of Science in Aerospace Engineering at Delft University of Technology. This research took place from September 2019 until July 2020 at Airborne Oil and Gas (AOG) in IJmuiden, The Netherlands.

First I would like to express my gratitude to AOG for providing me the opportunity to conduct my research and for using their facility and resources. I am proud of the fact I was part of, and contributed to, such an innovative company with an incredible knowledge in composites. AOG is ideally suited to gain experience in the field of composite engineering and therefore I consider this time as highly valuable for my development and future career.

I can look back on a wonderful time at AOG, in which I acquired a lot of knowledge and skills and, on top of that, had a lot of fun. Despite the given unusual circumstances of being forced to work from home due to the Covid-19 situation, I still felt very involved with the company. I want to thank my colleagues for their help and support during my research. My special thanks goes to my supervisor Teun Weustink, who always challenged me to get the most out of it and thus contributed to achieve the best possible results. In addition I would like to thank Jos Sinke for being my supervisor from the university and ensuring the interests of Delft University of Technology and AOG were aligned.

Finally, I would like to thank my friends, girlfriend and family for the constant encouragement and support.

Thank you for showing interest in my research and reading my thesis. I hope you enjoy it as much as I enjoyed writing it.



---

# Summary

In the production of thermoplastic composite pipes (TCPs), manufacturing-induced defects can occur. The aim of this study was to obtain a thorough understanding of the effects of defects in TCPs. Gaps and voids are the most frequently observed defects in the manufacturing and therefore the assessment of the mechanical performance in their presence is studied.

Gaps can occur due to deviations in the winding process and are matrix rich areas in which no reinforcement is present, reducing the stiffness and strength of the structure. For the assessment of gaps in TCPs, a finite element (FE) model was created for a 6 inch 40-layer EGF-HDPE TCP with a  $\pm 55^\circ$  layup. Gaps were modeled by assigning matrix properties to the gap area. A specific meshing technique was used, such that the elements follow the winding angle of the fibers, allowing the modeling of gaps the way they occur in TCPs. Internal pressure, a fiber dominated failure mode, was considered and the use of a submodeling technique allowed the assessment of the effect of gaps for various geometries and configurations. It was found that the presence of a gap provokes an equal stress increment in all layers having the same winding angle as the gap layer, with a slightly more pronounced effect in the first layer below the damaged ply having the same winding angle. The critical layer in having a gap is therefore found to be the second critical layer in the laminate, which has the same winding angle as the critical layer (highest loaded layer). The stress increment varies linear with the gap width and multiplies with the amount of overlapping gaps. The stress increment for multiple gaps rapidly diminishes when the longitudinal position between the gaps increases.

Tensile specimens ( $[(90/0)_2]_s$ ) with and without gaps were successfully manufactured and experimentally and virtually tested to study the mechanical properties. The decrease in mechanical properties in the case of a gap was found to be linear proportional to the gap size. More important, a good agreement was found between the experimental and virtual test results, which validated the gap modeling technique. Therefore it was concluded that the assessment on gaps in TCP level was correct.

Currently a tool is present to predict the effect of gaps on TCP level, based on a linear relationship as observed in flat laminates, in which the stress in the presence of a gap is evenly redistributed over the defect free cross-sectional area. From the modeling of gaps in TCPs, it was found that this assumption is invalid and therefore a new tool to assess the effect

of gaps is proposed. The proposed tool is based on a Python script, which can be executed in an FE TCP model in Abaqus. Using an element selection method, for each element it is calculated if, and what percentage of, the element is in the gap and the material properties of the element is reduced accordingly. This universal tool allows for a fast and computational inexpensive assessment of the effect of gaps in TCPs and can be used as an integral part of the design process and integrity management.

Voids are air inclusions in the laminate and can occur due to insufficient compaction or heating. In the TCP manufacturing, voids are generally the result of a gap in which the subsequent layer does not bond. A void is therefore defined as a delamination which follows the winding angle.

Two load cases were studied in the assessment of delaminations in TCPs. An external pressure load case was considered for the aforementioned TCP design. A delamination with an exceptional large dimension (30 x 200 mm) was modeled at different thickness positions and compared with a defect free case. The modeling of a delamination was done using tie constraints in the defect free area and double nodes in the delamination area. A contact condition was established between the delaminating layer and substrate surfaces. No significant differences were found in the buckling loads and only minor increases in maximum fiber stress were observed, which were still 50 % below the allowable stress. The geometry of the delamination, which follows the fiber orientation, in combination with the pressure keeping the delamination closed are expected to be the reasons of the absence of a performance decrease.

A lateral crushing load case, in which the through-thickness matrix properties are of importance, was both virtually and experimentally tested. A 2.5 inch, 80-layer EGF-HDPE TCP with three different delamination sizes in the midplane of the laminate was considered. Decreases in stiffness and an onset of delamination growth were observed in experimental testing. However, no significant decreases in the maximum load capacity were observed in the presence of a single (growing) delamination, indicating a damage tolerant design. A mismatch between the experimental results and the FE modeling was however present. The used modeling technique did not allow the delamination edge to grow and stress peaks, dependent on the mesh size, were observed. Effort has been made to predict the onset of delamination growth based on the value of the global stress field in which a defect free TCP fails, but no correlation was found. A correct failure indicator to predict the onset of delamination growth is missing. It is expected that the onset of delamination growth is determined by the material fracture toughness and fracture mechanics need to be involved for an accurate assessment, which is left for future studies.

In this study a tool is proposed for the assessment of manufacturing-induced gaps in TCPs to improve the design and manufacturing process and contributes to an improved integrity management system. Although future work is required for the assessment of voids in TCPs, an insight is provided on their effects on TCPs and recommendations for future research are made.



---

# Table of Contents

<b>1</b>	<b>Introduction</b>	<b>1</b>
1.1	Project background . . . . .	1
1.2	Thermoplastic composite pipe . . . . .	2
1.2.1	TCP principle . . . . .	2
1.2.2	Material . . . . .	3
1.2.3	Loads . . . . .	3
1.2.4	Manufacturing . . . . .	4
<b>2</b>	<b>Literature Review</b>	<b>5</b>
2.1	Defects . . . . .	5
2.2	Gaps in composite structures . . . . .	6
2.2.1	Current gap assessment tool . . . . .	7
2.2.2	FE modeling of gaps . . . . .	8
2.2.3	Effect of gaps on mechanical performance . . . . .	8
2.3	Delaminations in composite structures . . . . .	9
2.3.1	Analytical calculation . . . . .	10
2.3.2	FE modeling of delaminations . . . . .	12
2.3.3	Failure prediction . . . . .	13
2.3.4	Influencing factors . . . . .	13
2.4	Conclusions . . . . .	15
2.5	Thesis outline . . . . .	16
<b>3</b>	<b>Modeling of defects in TCPs</b>	<b>19</b>
3.1	TCP model . . . . .	19
3.1.1	Research TCP definition . . . . .	19
3.1.2	Cylindrical coordinate system . . . . .	20
3.1.3	Geometry . . . . .	22

3.1.4	Material . . . . .	22
3.1.5	Boundary conditions . . . . .	23
3.2	Tensile specimen with gaps . . . . .	23
3.2.1	Model . . . . .	23
3.2.2	Results . . . . .	24
3.3	TCP model including gaps - internal pressure . . . . .	25
3.3.1	Internal pressure load case . . . . .	25
3.3.2	Mesh convergence study global model - defect free . . . . .	26
3.3.3	Submodel - defect free . . . . .	27
3.3.4	TCP model including gaps . . . . .	27
3.3.5	Results . . . . .	30
3.4	TCP model including voids - external pressure . . . . .	33
3.4.1	TCP model including voids . . . . .	35
3.4.2	External pressure load case . . . . .	35
3.4.3	Linear buckling analysis . . . . .	35
3.4.4	Geometric imperfection . . . . .	36
3.4.5	Non-linear buckling analysis . . . . .	36
3.4.6	Results . . . . .	37
3.5	TCP model including voids - lateral crushing . . . . .	38
3.5.1	TCP model . . . . .	38
3.5.2	Lateral crushing load case . . . . .	39
3.5.3	Results . . . . .	40
3.6	Conclusions . . . . .	42
<b>4</b>	<b>Testing of defects in TCPs</b>	<b>43</b>
4.1	Gaps in specimens . . . . .	43
4.1.1	Plate manufacturing . . . . .	43
4.1.2	Coupon extraction . . . . .	44
4.1.3	Tensile test . . . . .	45
4.1.4	Results . . . . .	45
4.2	Voids in TCPs . . . . .	46
4.2.1	Pipe manufacturing . . . . .	46
4.2.2	Test specimens . . . . .	46
4.2.3	Lateral crushing test . . . . .	47
4.2.4	Results . . . . .	48
4.3	Conclusions . . . . .	49
<b>5</b>	<b>Validation of defect modeling in TCPs</b>	<b>51</b>
5.1	Validation gap modeling . . . . .	51
5.2	Validation void modeling . . . . .	52
5.3	Conclusions . . . . .	54

---

<b>6</b>	<b>Tool to assess the effects of defects in TCPs</b>	<b>55</b>
6.1	Current gap assessment tool . . . . .	55
6.1.1	Current gap assessment tool used for tensile coupons . . . . .	55
6.1.2	Current gap assessment tool used for TCPs . . . . .	56
6.2	Proposed gap assessment tool . . . . .	57
6.3	Proposed gap assessment tool analysis and validation . . . . .	61
6.3.1	Normal mesh method . . . . .	61
6.3.2	Defect layer method . . . . .	63
6.3.3	Biased mesh method . . . . .	65
6.3.4	Results . . . . .	66
6.4	Use of the proposed gap assessment tool . . . . .	67
6.5	Conclusions . . . . .	68
<b>7</b>	<b>Conclusions and recommendations</b>	<b>71</b>
7.1	Conclusions . . . . .	71
7.1.1	Effect of gaps on the performance of TCPs . . . . .	71
7.1.2	Effect of voids on the performance of TCPs . . . . .	72
7.2	Recommendations . . . . .	73
	<b>References</b>	<b>75</b>
<b>A</b>	<b>Thick walled cylinder stresses</b>	<b>81</b>
<b>B</b>	<b>Gap assessment tool - Python code</b>	<b>85</b>



---

# List of Figures

1.1	TCP principle [11]. . . . .	2
1.2	Hoop-, radial-, axial- and shear stresses in a cylinder (adopted from [12]). . . . .	3
1.3	TCP production line layout. . . . .	4
2.1	Defect size versus residual strength. . . . .	5
2.2	Picture of a gap. . . . .	6
2.3	Schematic gap in a pipe (top) and in a laminate cross-section (bottom). . . . .	6
2.4	Picture of a void. . . . .	7
2.5	Schematic void in a pipe (top) and in a laminate cross-section (bottom). . . . .	7
2.6	Normalized properties with respect to the gap area percentage for a gap-modified defect layer [19]. . . . .	8
2.7	Error in calculating gap area percentage using the approach explained in [18] and the defect layer method [19]. . . . .	8
2.8	Top view of a laminate containing gaps in the $0^\circ$ direction (adopted from [15]). . . . .	10
2.9	Delamination buckling modes: local buckling (top), mixed buckling (middle) and global buckling (bottom). . . . .	11
2.10	Delamination in a cylinder subjected to external pressure [35]. . . . .	11
2.11	Critical load parameter for delaminated cylinders [35]. . . . .	11
2.12	Linear and non-linear buckling analysis. . . . .	12
2.13	2-Dimensional FE model of a delamination using solid elements. . . . .	12
2.14	FE prediction of the maximum compression stress in the fiber direction for local buckling (left) and global buckling (right) in case of a delamination (indicated with a dashed square) [43]. . . . .	13
2.15	Effect of a rectangular delamination size on the critical buckling load of composite cylindrical shells subjected to axial compression for thickness positions $\bar{h} = 0.5$ (left) and $\bar{h} = 0.1$ (right) [49]. . . . .	14

2.16	Effect of a rectangular delamination size on the critical buckling load of composite cylindrical shells subjected to external pressure for thickness positions $\bar{h} = 0.5$ (left) and $\bar{h} = 0.1$ (right) [50]. . . . .	14
3.1	Schematic determination of the winding angle ( $\phi$ ) over a pipe in 2-dimensional (left) and 3-dimensional (right). . . . .	20
3.2	TCP geometry, in mm. . . . .	21
3.3	FE TCP model with a helix definition (left) and the associated mesh representing the winding angle of the $+\phi$ layers (right). . . . .	22
3.4	FE tensile model. The modeled section is highlighted in red and the section indicated in orange is used to assign gap properties to. Load is applied in the $z$ -direction. . . . .	24
3.5	Stress strain plot for the defect free and gap model to determine the $E$ -modulus. . . . .	25
3.6	Visualization of the fiber tensile stress in the gauge section of a tensile coupon for the defect free model (top) and the gap model (bottom) for the same applied load. . . . .	26
3.7	The application of internal pressure. . . . .	26
3.8	Global TCP model with the submodel location indicated in red (left), the submodel part (middle) and its converged mesh size for gaps (right). . . . .	28
3.9	Representation of a 10 mm gap in a global TCP model (left) and the corresponding submodel (right), in which green represents the defect free material and beige the gap. For clarity only the element layer which includes the gap is shown. . . . .	29
3.10	Visualization of the fiber tensile stress in layer 21 (left) and the other uneven layer numbers (right) for a 10 mm gap in layer 21. . . . .	30
3.11	Visualization of the fiber tensile stress in layer 21 (left), 20 (middle) and 19 (right) for a 10 mm gap in layer 21. . . . .	31
3.12	Fiber tensile stress per layer for the defect free model and a 10 mm gap in layer 21. . . . .	32
3.13	Stress increase per layer for a 10 mm gap at layer 21 compared with the defect free model. . . . .	32
3.14	Increase in maximum fiber tension stress for different gap widths and thickness positions. . . . .	33
3.15	The effect of longitudinal distance between two gaps on the increase in maximum fiber tension stress. . . . .	34
3.16	Schematic representation of the cross-section of the laminate in the longitudinal direction with a gap in layer 3 and in layer 5. . . . .	34
3.17	Location of the delamination area on the TCP (left) and the modeling technique of a delamination (right). . . . .	35
3.18	The application of external pressure. . . . .	36
3.19	Visualization of the stress state in the entire TCP (left) and cross-sectional (right) reinforcement for external pressure for a TCP with a delamination at $\bar{h} = 0.5$ . . . . .	37
3.20	Fiber compression stress for a TCP subjected to external pressure. . . . .	38
3.21	Lateral crushing model including load application. TCP characteristic colors are included for clarification. . . . .	39
3.22	Location delaminations for lateral crushing models (left) and the submodel for the 13 mm delamination (top right) with its mesh (bottom right). . . . .	40
3.23	Visualization of the matrix equivalent stress state in the reinforcement of a defect free TCP subjected to lateral crushing. . . . .	41

3.24	Visualization of the matrix equivalent stress state in the reinforcement of a TCP with a 13 mm delamination subjected to lateral crushing. . . . .	42
4.1	Schematic layout for the control (left) and test (right) plates including the location of the specimens. . . . .	44
4.2	Photo of a control (top) and a test (bottom) specimen. . . . .	44
4.3	Tensile test setup. . . . .	45
4.4	Lateral crushing test setup with a delamination at $\bar{h} = 0.5$ with a $45^\circ$ anticlockwise angle towards the direction of loading. . . . .	47
4.5	Load displacements curves for one specimen of the control group and one per test series. . . . .	49
5.1	Comparison load displacement curves of experimental and virtual tested lateral crushing specimens. . . . .	53
5.2	Visualization of the matrix equivalent stress state in the reinforcement of a TCP with a delamination $\alpha = \pi$ at $\bar{h} = 0.5$ subjected to lateral crushing. . . . .	53
6.1	Comparison of FE modeling results with the current gap tool for the increase in the maximum fiber tension stress for different gap widths and thickness positions. . . . .	56
6.2	Cylindrical coordinate system. . . . .	58
6.3	2-Dimensional representation of a TCP including elements and a helix in the winding direction. . . . .	59
6.4	TCP with a 10 mm gap in layer 21 with the gap set highlighted (left) and the defined composites layups for R6 (right), in which green represents the defect free layup and beige the layup for the gap set. . . . .	60
6.5	Abaqus composite layup definition for the gap set for a gap in layer 21. . . . .	61
6.6	Visualization of the fiber tensile stress in layer 1 for a 10 mm gap in layer 21 for the gap tool using an arbitrary mesh size (left) and a mesh size with an aspect ratio of 0.7 (right). . . . .	63
6.7	2-Dimensional representation of an element to calculate the distance from a node to the diagonal. . . . .	63
6.8	Mesh sensitivity study of the increase in the maximum fiber tension stress for a 10 mm gap in layer 21 for three different methods. . . . .	64
6.9	Visualization of the fiber tensile stress in layer 1 for a 10 mm gap in layer 21 for the gap tool using the defect layer method (left) and the biased mesh method (right). . . . .	65
6.10	Comparison of FE modeling results using the proposed gap tool for the increase in the maximum fiber tension stress for different gap widths in layer 21 using three different methods. . . . .	66
6.11	Fiber compression stress for a TCP subjected to external pressure predicted with the proposed gap tool. . . . .	67
6.12	Predicted increase in the maximum fiber tension stress for different gap widths in layer 21 using the proposed gap tool. . . . .	68
6.13	Four schematic representations of the cross-section of a TCP laminate in the longitudinal direction with gaps in the $+\phi$ layers (blue) and $-\phi$ layers (orange). Dimensions in mm. . . . .	69





---

# List of Tables

1.1	TCP materials. . . . .	3
2.1	Effect of gaps with different gap width ratios ( $\beta$ ) on normalized stiffness and strength related properties of a lamina, observed by Heinecke et al. [15]. . . . .	10
3.1	TCP geometry. . . . .	21
3.2	TCP layup laminate. . . . .	21
3.3	Predicted $E$ -modulus and failure load difference for the gap model with respect to the defect free model. . . . .	24
3.4	Helix mesh convergence study baseline global model. . . . .	27
3.5	Helix mesh convergence study baseline submodel. . . . .	28
3.6	Helix mesh convergence study submodel including a 10 mm gap in layer 21. . . . .	29
3.7	Maximum fiber stress increase of an infinitely large gap. . . . .	32
3.8	Differences in external pressure and fiber compression stress for a TCP containing a delamination at different thickness positions with respect to a defect free situation. . . . .	38
3.9	Differences in lateral crushing failure predictions for a TCP containing a delamination with different widths with respect to a defect free situation. . . . .	41
4.1	Summary experimental tensile test data. Differences of the test group with respect to the control group. . . . .	46
4.2	Lateral crushing test series. . . . .	47
4.3	Summary experimental lateral crushing test data. Differences in mean values for the test series with respect to the control defect free group. . . . .	49
5.1	Comparison FE modeling and experimentally obtained decreases in $E$ -moduli and failure loads for tensile specimens containing gaps with respect to defect free specimens. . . . .	51
5.2	Comparison FE modeling and experimentally obtained decreases in the crushing load at the onset of delamination growth for lateral crushing specimens with respect to defect free specimens. . . . .	52

6.1	Comparison of the strength decrease obtained by FE modeling, experimental testing and using the current gap tool, for tensile specimens containing gaps with respect to defect free specimens. . . . .	56
6.2	Proposed gap tool sensitivity study for different methods. . . . .	62

---

# Nomenclature

## Glossary

Abaqus	Finite element package from Simulia Dassault Systèmes used for predictive engineering
Coupon	Specimen to determine material properties by testing
Delaminating layer	The sublaminates above a delamination (or towards the outside in a cylindrical structure)
Gap	An area in a composite structure where reinforcement fibers are missing
Global buckling	A mode in which the delaminating layer and the substrate buckle in the same direction
Local buckling	A mode in which the delaminating layer buckles, but not the substrate
Matrix	Material that embeds the reinforcement fibers
Mixed buckling	A mode in which the delaminating layer and the substrate buckle in the opposite direction
Substrate	The sublaminates below a delamination (or towards the inside in a cylindrical structure)
Thickness position	The thickness of the delaminating layer divided by the thickness of the total laminate
Void	An air inclusion in a TCP as a result of a gap when the subsequent layer is not bonded in the gap area

## Abbreviations

AOG	Airborne Oil and Gas B.V.
AR	Aspect Ratio
EGF	E-Glass Fiber
FE	Finite Element
FEM	Finite Element Modeling
HDPE	High Density Polyethylene
ID	Inner Diameter
OD	Outer Diameter
PA12	Polyamide 12
PVDF	Polyvinylidene Fluoride
SF	Safety Factor
TCP	Thermoplastic Composite Pipe
UD	Unidirectional
WT	Thickness

## Symbols

$\alpha$	Delamination width (angle)
$\bar{h}$	Delamination thickness position
$\beta$	Ratio between gap width and total laminate width
$\Delta y$	Change in inside diameter
$\epsilon$	Strain
$\phi$	Winding angle
$\sigma$	Stress
$E$	Young's modulus
$P$	Strength
$P_{crush}$	Crushing resistance
$S33$	Fiber stress in a TCP model

---

# Chapter 1

---

## Introduction

This chapter introduces the project. The project background is described in Section 1.1 and in Section 1.2 the principle and basics of a thermoplastic composite pipe (TCP) are discussed.

### 1.1 Project background

Fiber reinforced plastics are extensively used in many industries due to their benefits as a high strength-to-weight ratio, environmental resistance and their anisotropic behavior giving them design flexibility [1, 2]. In the oil and gas industry, traditional metallic pipes have difficulties to fulfill the requirements of high corrosive media and environmental influences in deepwater applications [3]. The use of composite based alternatives is therefore becoming an important solution in this industry [4]. However, the use of anisotropic materials increases the design complexity and therefore a comprehensive understanding of the mechanics, materials and the intricacies in the manufacturing process is required [5].

Although life cycle costs of fiber reinforced plastics are in general lower compared to traditional alternatives, the production costs are often higher [6, 7]. In addition, not enough attention is often given to the effects of defects in composite product development, causing work slowdowns and increased costs during product manufacturing and maintenance. In fact, no structure can be manufactured without defects and therefore a defect free design approach is not valid. Traditional design approaches consider defects as thresholds for accepting or repairing and not as variable in the material state [8].

In order to possibly reduce costs, the effects of defects must be assessed. A mechanics-based knowledge of the characterization of defects and their effects on structural performance is required to provide engineering databases to deal with manufacturing defects. Without a thorough understanding of defects, engineers are often forced to repair using conservative assumptions while alternative, cheaper solutions may be possible [9].

This research is conducted at Airborne Oil and Gas, hereafter referred to as AOG, the world's first and leading manufacturer of fully bonded TCP for primarily subsea applications.

## 1.2 Thermoplastic composite pipe

In this section the principle of a TCP is described, including the materials used, the loads it must withstand and the manufacturing process.

### 1.2.1 TCP principle

The concept of a TCP is based on a solid wall construction consisting of an inner liner, laminate and coating, as in Figure 1.1. The fiber reinforced laminate is built on an extruded liner using tape winding and a coating is extruded over the laminate. All three parts consist of the single polymer material and are melt-fused together, resulting in a bond line in between the layers which is as strong as the base materials. End fittings can be installed to connect a TCP to other applications. The use of thermoplastic material enables relatively high allowable strains and therefore gives a TCP flexible and spoolable characteristics. A TCP have to comply with the regulations according to DNVGL-ST-F119 [10], a standard describing requirements for flexible TCPs for offshore applications.

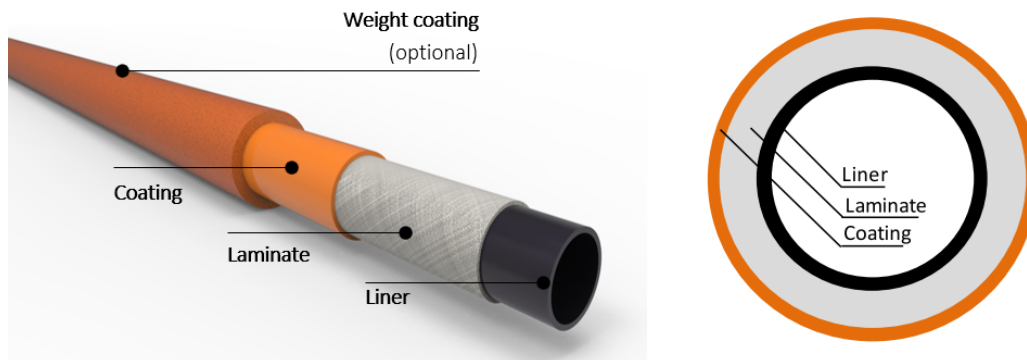


**Figure 1.1:** TCP principle [11].

The function of the liner is to act as a fluid barrier on the inside of laminate. Important parameters for liners are the level of permeability and chemical resistance. The extrusion process ensures a smooth surface, empowering high flow rates. The liner has high yield strains, enabling the liner to follow the movements of a TCP and stay within the elastic range of the polymer material.

The basic structural layer of a TCP is the laminate, a composite reinforcement providing load carrying capacity. The laminate is built up of a number of unidirectional (UD) layers of tape with a tailored orientation angle, depending on the application. The  $0^\circ$  is defined in the axial direction and the  $90^\circ$  in the circumferential. Generally two type of layups, with different winding angles ( $\phi$ ), are used in TCP manufacturing. For pressure applications a  $\pm 55^\circ$  pressure balanced layup is used while for more tensile applications a  $\pm 40^\circ$  (tensile layers) and  $\pm 80^\circ$  (hoop layers) layup is used in which the orientation accounts primarily for tension and pressure forces, respectively.

The laminate is covered with a coating, providing protection against wear, damage, environmental influences and permeation of a fluid. Optionally a weight coating can be extruded to improve the on-bottom stability.

### 1.2.2 Material

Depending on the specific requirements for an application, a different set of materials can be used (Table 1.1). For the reinforcement material a distinction is made between E-glass fiber (EGF) and carbon fiber, based on the loading requirements. High density polyethylene (HDPE) matrix polymer is used in combination with EGF and polyamide 12 (PA12) or polyvinylidene fluoride (PVDF) is used in combination with carbon. The selection of the matrix material depends primarily on temperature requirements, permeation and chemical resistance. The current knowledge, certification and database for EGF-HDPE is largest. Moreover, this material combination is most commonly used and therefore has the largest production output. EGF-HDPE is therefore identified as TCP material of interest in this study.

**Table 1.1:** TCP materials.

Component	Material		
Reinforcement	E-glass	Carbon	Carbon
Polymer	HDPE	PA12	PVDF

### 1.2.3 Loads

During manufacturing, transport, installation and operational life a TCP is subjected to pressure-, functional-, environmental- and accidental loads. Static loads include:

- Internal pressure
- External pressure
- Axial tension
- Axial compression
- Lateral compression
- Bending
- Torsion

Generally, these loads can introduce hoop- ( $\sigma_h$ ), radial- ( $\sigma_r$ ), axial- ( $\sigma_a$ ) and shear stresses ( $\tau$ ), as shown in Figure 1.2.

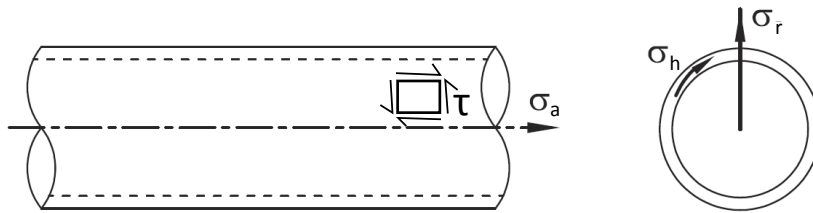


**Figure 1.2:** Hoop-, radial-, axial- and shear stresses in a cylinder (adopted from [12]).

A combination of the individual load cases are possible as well. In the long term, creep, fatigue and stress rupture are considered. Effects due to impact, fire, erosion, chemicals, UV and fluid velocities need to be taken into account as well.

Thin-walled assumptions are not valid for TCPs, as the diameter-to-thickness ratio is relatively low. A threshold for using thin-walled assumptions of  $\frac{D}{t} > 20$  is often used [13].

Stresses between the inner and outer diameter can differ significantly and this has to be taken into account. Cylinder stresses due to the above mentioned static loads are presented in Appendix A. These stresses apply when isotropic material properties are considered. The involved mathematical complexity in performance predictions urges the need for finite element (FE) analysis and therefore the FE software Abaqus is used in the design and analysis of TCPs.

### 1.2.4 Manufacturing

TCPs are manufactured in a continuous process and a schematic representation of a production line is shown in Figure 1.3. The production line consists of the following basic elements:

- |                              |                     |
|------------------------------|---------------------|
| 1. Pay off carousel          | 4. Winding station  |
| 2. Traversing unit           | 5. Caterpillar      |
| 3. Length measurement system | 6. Take up carousel |

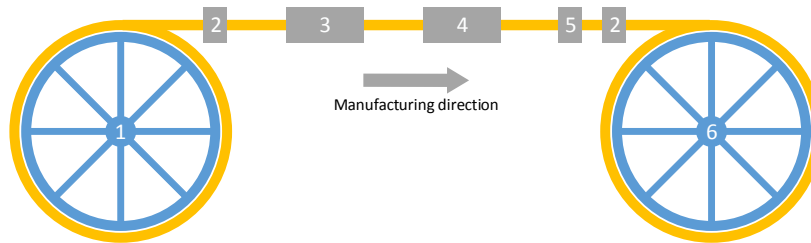


**Figure 1.3:** TCP production line layout.

The liner is extruded and connected between the take up and pay off carousels (1 and 6). The pipe manufacturing takes place between these carousels in the winding station (4), where the composite tape is wound and melt-fused. During the melt-fusion process both heat and pressure are applied to achieve a good consolidation and bonding between the layers. A caterpillar (5) regulates the manufacturing speed and pulls the pipe through the winding station, after which the pipe is coiled in the take up carousel (6). After a run, the pipe is rewound in the pay off carousel and the process is repeated for the subsequent layer(s). If all layers of the laminate are applied, the pipe is provided with a coating. The coating is applied with a different set of machinery and is heated, extruded and cooled on the pipe in one single operation. Depending on the length and laminate thickness the manufacturing process ranges from weeks to months.

During the manufacturing process, the pipe is continuously visually inspected. When a deviation from nominal (defect) is found, the process is stopped and further action is taken. Stopping the process is a costly operation and it is therefore valuable to reduce the manufacturing downtime as much as possible. On the one hand, the process can be optimized to reduce the amount of manufacturing defects. On the other hand, a thorough knowledge about the effects of defects can possibly allow certain defects in the pipe. This research is focused on the latter; to assess the mechanical performance in the presence of manufacturing-induced defects.



---

## Chapter 2

---

# Literature Review

This chapter is based on an extensive literature study from which the key topics are summarized here. The manufacturing defects of interest have been identified, through an in-house study, to be gaps and voids and are described in Section 2.1. Literature regarding gaps and voids is reviewed in Section 2.2 and Section 2.3, respectively. Conclusions are drawn in Section 2.4 and in Section 2.5 the thesis outline is presented.

### 2.1 Defects

In the broadest sense a defect can be defined as anything that deviates from an ideal and uniform structure [14]. Depending on the structure and purpose, it can be determined whether a local deviation is considered a defect or not. The size of the defect has an influence on the performance, as shown in Figure 2.1. Very small defects (size 1) may not affect the global performance while the larger the defect, the more the residual strength reduction. At some point (size 2) the residual strength equals the allowable strength, indicating the maximum defect size the structure could withstand without conflicting with the required/design loads.

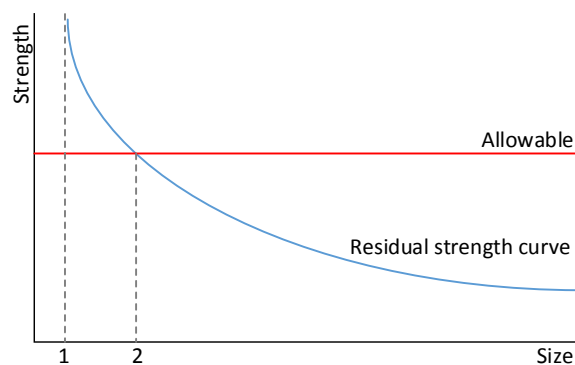


**Figure 2.1:** Defect size versus residual strength.

Important parameters in the production of a TCP are time, temperature and pressure during the melt-fusion process. The manufactured TCP can deviate from the nominal design leading to defects in the TCP. The two most common defects are gaps and voids.

During the winding process, the tapes are intended to be wound exactly side by side. This is however a complex process and the melt-fusion system can distort the position, leading to gaps. In a gap the wound reinforcement layer is not present, resulting in locally less fibers, as shown in Figure 2.2 and Figure 2.3. The tension in the tape during the melt-fusion process pulls the next layer of tape over the gap, forming a bridge and preventing out-of-plane undulations in the fibers. The gap is filled with excess matrix material from the tooling and variations in the thickness are found to be negligible. Gaps are defined by the length ( $L_g$ ) along the pipe and the width ( $W_g$ ) of the gap.



**Figure 2.2:** Picture of a gap.

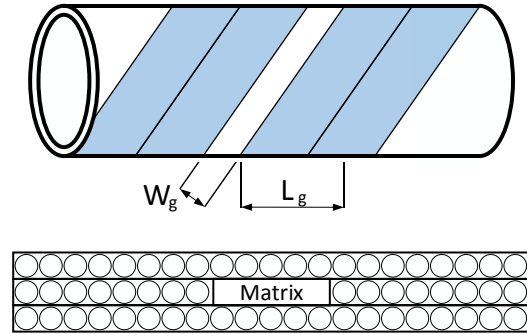


**Figure 2.3:** Schematic gap in a pipe (top) and in a laminate cross-section (bottom).

Voids are air inclusions in a composite laminate and are often the result of local insufficient compaction or heating. Randomly shaped voids are possible due to irregularities in the underlying surface. However, during the manufacturing process a void is often the result of a gap when the subsequent layer does not bond with layer in the gap during the melt-fusion process and therefore has a shape that follows the orientation of the gap, as shown in Figure 2.4 and Figure 2.5. This type of gap-induced voids differ from the standard term void content, indicating the porosity of the composite in general. Hereafter, a gap-induced void is meant when the term void is used. Similar to gaps, voids are defined by the length ( $L_v$ ) along the pipe and the width ( $W_v$ ) of the void. Whereas in a gap the interface between the plies is continued, in a void there is a discontinuity in interfaces, acting as a delamination.

## 2.2 Gaps in composite structures

For simple geometries, the effect of gaps in composite structures can be analytically calculated using for example the rule of mixtures and the classical lamination theory [15]. Currently, a statistical and straight forward approach to predict the strength decrease in TCPs containing gaps is present. In literature the use of FE modeling is widely used in the assessment of gaps on mechanical performance.



**Figure 2.4:** Picture of a void.

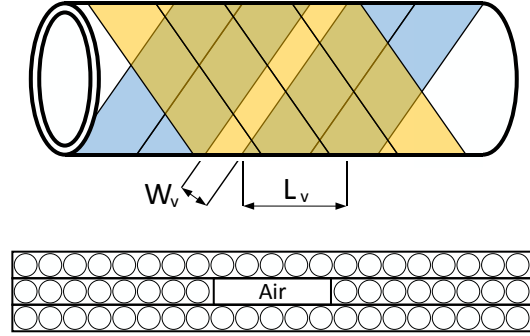


**Figure 2.5:** Schematic void in a pipe (top) and in a laminate cross-section (bottom).

### 2.2.1 Current gap assessment tool

The strength reduction in TCPs is based on area reduction and thus assumes zero stiffness in the gap area. It is assumed that the stresses a gap area would carry, are equally redistributed among the layers with the same winding angle. Based on the average gap width per winding of tape ( $W_g$ ), the tape width ( $W_t$ ) and a safety factor (SF) the layer strength reduction is calculated with:

$$\text{Layer strength reduction} = \frac{W_g}{W_t + W_g} SF. \quad (2.1)$$

Subsequently, the probability ( $p$ ) of a gap per tape width is calculated with:

$$p = \frac{W_g(\text{average number of gaps per wrap})}{W_t}, \quad (2.2)$$

where the average number of gaps per wrap is counted manually during manufacturing. With the layer strength reduction and the gap probability, the strength reduction of a TCP is predicted based on the amount of overlapping gaps. For this, a binomial distribution is assumed [16]:

$$P(r) = \frac{n!}{r!(n-r)!} p^r (1-p)^{n-r}, \quad (2.3)$$

where  $P(r)$  is the probability of exactly  $r$  successes (i.e. the amount of overlapping gaps),  $n$  is the number of events (i.e. number of  $+\phi$  or  $-\phi$  layers) and  $p$  is the probability of a single gap.

Finally, the strength reduction of a TCP is predicted using:

$$\text{Total strength reduction} = \frac{r (\text{layer strength reduction})}{n}. \quad (2.4)$$

The higher the amount of overlapping gaps ( $r$ ), the larger the total strength reduction but the lower the probability of that amount of overlapping gaps.

### 2.2.2 FE modeling of gaps

Although analytical methods provide an estimation of the strength reduction in the presence of a gap, their accuracy is limited for the more complex structures. FE modeling is therefore found to be suitable and is widely present in literature. In the analysis of gaps in composite structures, Cairns et al. [17] and Blom et al. [18] modeled gaps as matrix regions. However, it was found a very small element size is required to capture the gap area accurately, provoking high computational costs.

A method to reduce the computational costs without sacrificing accuracy was proposed by Fayazbakhsh et al. [19]. In this so called defect layer method, the defect percentage area per element is calculated and divided by the total element area to identify the amount of reduction in the material properties. The properties of the gap-modified defect layer are calculated for various gap percentages between 0 and 100 % and normalized with respect to the defect free layer (Figure 2.6). In the analysis of a structure containing a gap, the normalized properties for the defect layer are multiplied with the elements, and based on the defect percentage, the properties of the specific elements are reduced accordingly. The proposed method uses a significantly lower amount of elements compared to the aforementioned method of Blom et al. [18], while yielding more accurate results, as shown in Figure 2.7.

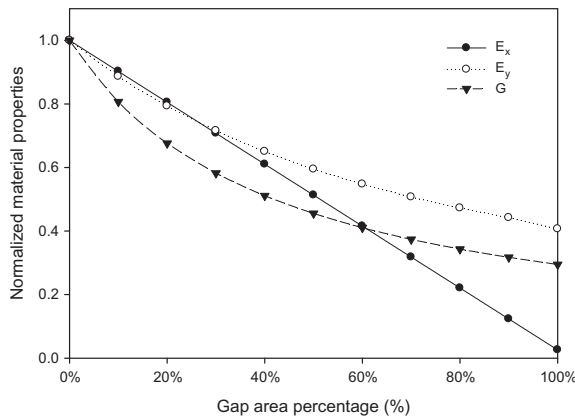


**Figure 2.6:** Normalized properties with respect to the gap area percentage for a gap-modified defect layer [19].

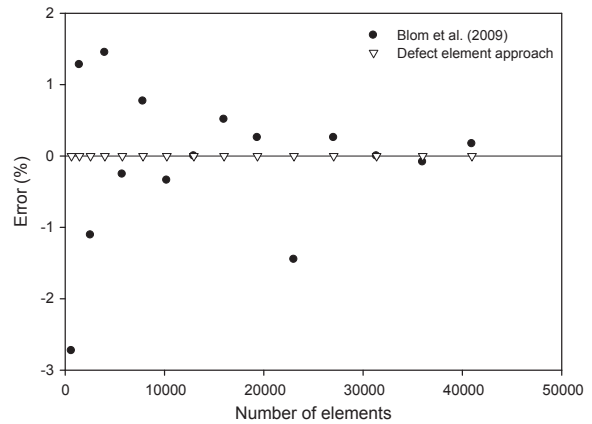


**Figure 2.7:** Error in calculating gap area percentage using the approach explained in [18] and the defect layer method [19].

### 2.2.3 Effect of gaps on mechanical performance

Several studies have been conducted in the investigation of the effect of matrix rich areas. Ghayoor et al. [20] studied the effect of intralaminar matrix rich areas on the failure initiation in carbon-epoxy samples. It was found that matrix pockets act as inconsistencies and are therefore vulnerable to stress propagation, which is predominantly important for reliability and long term behavior [21, 22]. The study concluded that failure strain is mainly determined

by the inter-fiber distance, whereas the failure stress is mainly determined by the amount of fibers. The amount of fibers (i.e. the fiber volume fraction) linearly determines the modulus of elasticity [23].

On laminate level, significant strength reductions due to gaps were also observed by Khan et al. [24] and Potter [25] in the tensile strength and flexural modulus, respectively. However, both authors claim that the decrease in strength is not due to the matrix richness itself, but due to out-of-plane fiber undulations because of the matrix richness. Similar claims have been made for the compression strength reduction of specimens containing gaps, in which the fiber waviness facilitated fiber micro-buckling [26–28]. In addition, a variation in stiffness through-the-thickness can induce an additional bending moment, which has an adverse effect on the strength [24].

Only little literature is present regarding gaps in cylindrical structures. The effect of gaps in the buckling response of composite cylindrical shells has been investigated by Broggi and Schuëller [29] and Hilburger and Starnes [30]. The authors found a significant influence on the torsional buckling moment, but both studies considered a gap as an area in which neither fibers nor matrix was present, leading to local thickness variations in the shell wall being the primary factor of the reduction in the buckling moments.

The primary factors reducing the mechanical performance in the presence of gaps, fiber out-of-plane undulations and thickness variations, are both not observed in TCPs, as shown in Figure 2.3. Heinecke et al. [15] studied the structural response of flat composite laminates containing manufacturing-induced gaps in a similar way as observed in TCPs. Flat laminates with constant gap widths spanning the length were considered, as shown in Figure 2.8. Normalized strength ( $X_T$ ,  $Y_T$ ,  $S$ ) and stiffness ( $E_1$ ,  $E_2$ ,  $G_{12}$ ,  $\eta_{12}$ ) related properties were calculated for different ratios of the gap width ( $\beta$ ) and are shown in Table 2.1. The ratio was used to calculate the effective stiffness of the laminate and is defined with Equation (2.5). This equation shows similarity with Equation (2.1), which calculates the layer strength reduction in TCPs.

$$\beta = \frac{\text{width}_{\text{gap}}}{\text{width}_{\text{lamina}}} \quad (2.5)$$

It was found that gaps do not affect the shear strength ( $S$ ), transverse fiber strength ( $Y_T$ ) and material coefficient of viscosity ( $\eta$ ). The elastic and shear moduli decrease, as expected, due to the fact gaps are modeled as matrix area. The strength in the fiber direction ( $X_T$ ) decreases with increasing gap width, as there are less fibers in the loading direction. A linear relationship between the gap size and strength reduction was observed, in which the largest decrease in strength (74 %) was observed in the fiber direction for a gap width ratio of 0.76. With this it can be stated that a gap has a significant effect on the stiffness and strength on lamina level. This effect is however reduced when a larger scale (e.g. laminate) is considered.

## 2.3 Delaminations in composite structures

Delaminations primarily cause a reduction in compression strength [31, 32]. The mechanism behind this strength reduction is the out-of-plane buckling of the so-called delaminating layer,

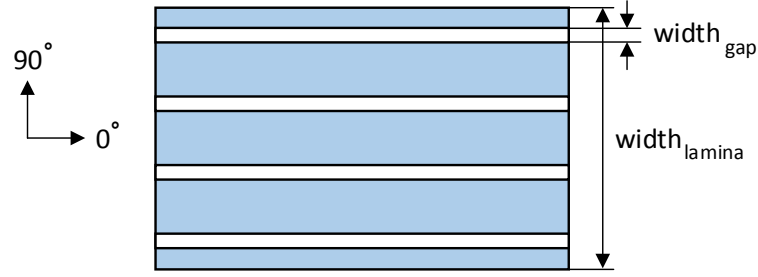


**Figure 2.8:** Top view of a laminate containing gaps in the  $0^\circ$  direction (adopted from [15]).

**Table 2.1:** Effect of gaps with different gap width ratios ( $\beta$ ) on normalized stiffness and strength related properties of a lamina, observed by Heinecke et al. [15].

$\beta$	$X_T$	$Y_T$	$S$	$E_1$	$E_2$	$G_{12}$	$\eta_{12}$
0.00	1	1	1	1	1	1	1
0.09	0.92	1	1	0.92	0.88	0.80	1
0.18	0.85	1	1	0.85	0.78	0.67	1
0.30	0.73	1	1	0.73	0.68	0.53	1
0.76	0.26	1	1	0.26	0.43	0.30	1

as shown in Figure 2.9 [33]. A delamination in a structure can cause the delaminating layer to buckle (local buckling) before the global buckling load is reached. Between local and global buckling a mixed mode is also possible, in which the relative out-of-plane displacements of the delaminating layer and substrate are in the opposite direction. These three buckling modes are shown in Figure 2.9. Delaminations are a common phenomenon in composite structures and it is therefore of high importance that a structure with delaminations can continue its operation without failure [22]. Delamination growth occurs when interlaminar stresses exceed the strength of the matrix between plies [34].

### 2.3.1 Analytical calculation

Delaminations in cylindrical structures is analytically studied by several authors [35–37]. Critical loads for delamination with a constant width along the cylinder were predicted using linear buckling analyses, as shown in Figure 2.10 and Figure 2.11. In terms of nomenclature, the thickness position of a delamination is denoted by  $\bar{h}$  and is defined as the thickness of delaminating layer divided by the thickness of the total laminate. The delamination width is defined as the angle from the midpoint of a cylinder to both ends of a delamination in the circumferential direction, denoted by  $\alpha$ .  $\bar{L}$  is the cylinder length-to-radius ratio and  $R/h$  indicate the radius-to-thickness ratio. It was found that a small width has a limited effect on the critical load parameter, regardless the thickness position. As the delamination width increases, the critical load rapidly decreases, indicating the occurrence of local buckling. Delaminations close to the surface of the shell ( $\bar{h} = 0.1$  or  $0.9$ ) were found to be more critical than delaminations in middle ( $\bar{h} = 0.5$ ). However, for a delamination close to a surface the failure is dominated by delamination growth rather than local delamination buckling.

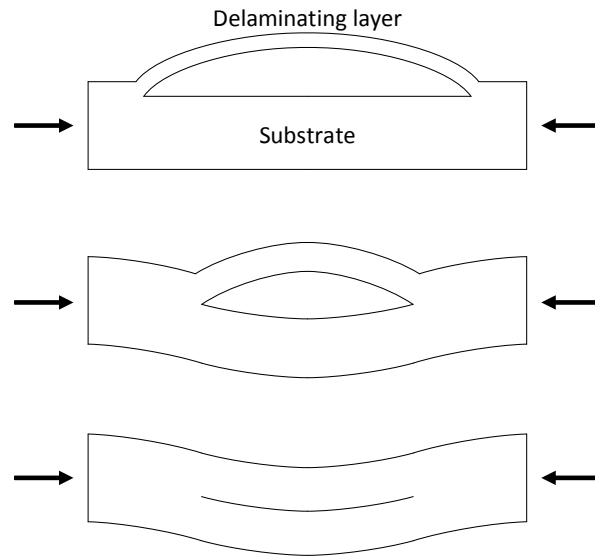


**Figure 2.9:** Delamination buckling modes: local buckling (top), mixed buckling (middle) and global buckling (bottom).

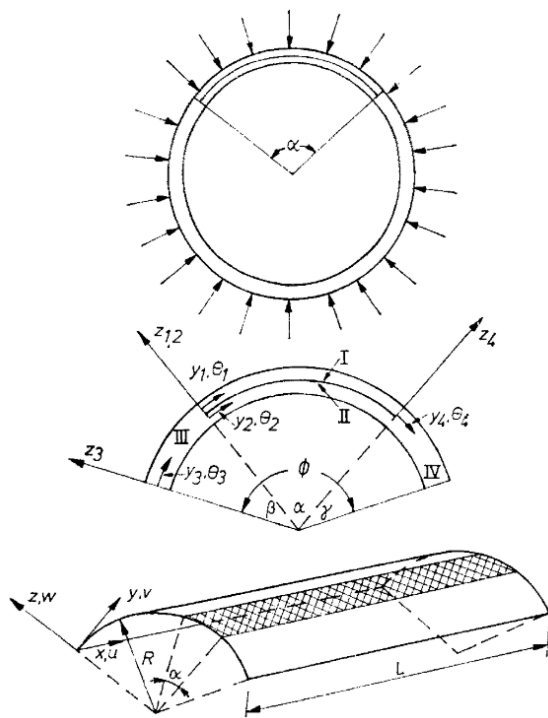


**Figure 2.10:** Delamination in a cylinder subjected to external pressure [35].

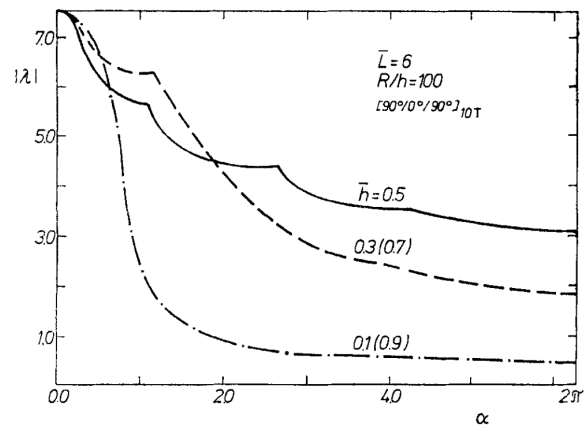


**Figure 2.11:** Critical load parameter for delaminated cylinders [35].

Analytical performance predictions are based on a linear buckling analysis, in which the bifurcation point, which is defined as a point where a small change in a parameter value causes a sudden change in the stability of an equilibrium, is found [38]. This point, as shown in Figure 2.12, is found by solving:

$$[K] \{\phi_i\} = \lambda_i [S] \{\phi_i\}, \quad (2.6)$$

where  $[K]$  is the structural stiffness matrix,  $\{\phi_i\}$  the eigenvector,  $\lambda_i$  is the eigenvalue and  $[S]$  is the stress stiffness matrix.

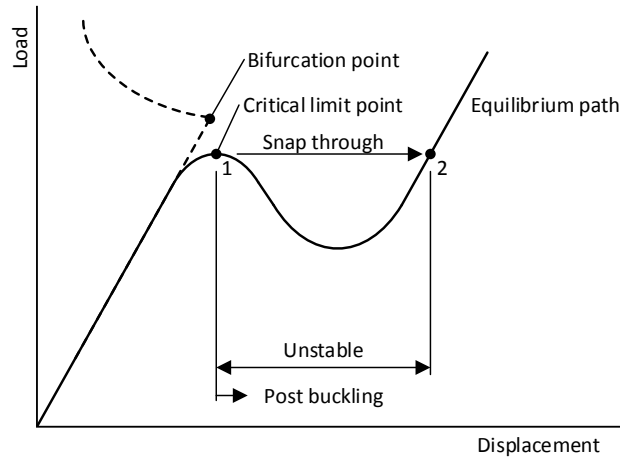


**Figure 2.12:** Linear and non-linear buckling analysis.

However, in reality structures do exhibit imperfections and show a non-linear behavior that prevent them for achieving their theoretical critical buckling load [39]. A linear buckling analysis therefore yields unconservative results [40].

### 2.3.2 FE modeling of delaminations

In general, the loadings and geometries of composites structures are not as straight forward as often seen in analytical calculations and examples, forcing to use FE modeling. Moreover, characteristics as material non-linearity and structural imperfections can be adopted in FE modeling as well.

The modeling of delaminations in structures using solid elements in FE modeling is widely used in literature [41–47]. A delamination can be modeled as two parts in which the coincident nodes of the defect free structure are merged or tied, while the nodes in the area of delamination are not, as shown in Figure 2.13. When both parts are meshed, double nodes occur at the delamination area, allowing to separate from each other.

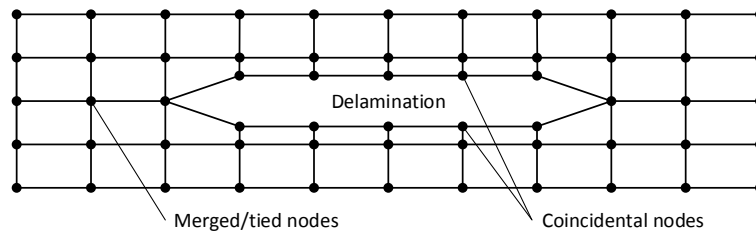


**Figure 2.13:** 2-Dimensional FE model of a delamination using solid elements.



In contrast to analytical calculations, a contact effect can be established between the surfaces of the delaminating layer and substrate. Analytical calculations allow penetration of both surfaces, having a low physical meaning. Several authors compared the results including and excluding the contact effect [48–50]. It was found that a delamination does not open when external pressure is applied, independent of the size of the delamination, leading to buckling loads up to 50 % higher in case a contact condition was used.

### 2.3.3 Failure prediction

Delamination failure can be predicted in several ways. Most commonly used is the non-linear buckling analysis shown in Figure 2.12 [49–54]. In a non-linear buckling analysis, the load on a structure is gradually increased until the load is found when the structure becomes unstable, i.e. the non-linear buckling load or critical limit point [40, 55]. A non-linear unstable region is present, in which the equilibrium path goes from one stable point (point 1) to a new stable point (point 2). The slope of the equilibrium curve is also known as tangent stiffness and when it approaches zero, the non-linear buckling load can be found [56].

Pavier and Clarke [57] and Short et al. [43] predicted delamination failure in flat specimens based on the maximum compression strength. Their method implies that failure of delaminated specimens can be predicted by the load at which the maximum compression stress in the fibers reaches their maximum value, in which the maximum value is obtained from undamaged specimen analyses. The methodology of this method is visualized in Figure 2.14. A buckled delaminating layer (local buckling) loses its stiffness leading to greater stresses in the substrate. If global buckling occurs, the laminate as a whole carries the stresses and the maximum compression stress is reached in the mid-section at the inner buckling side.

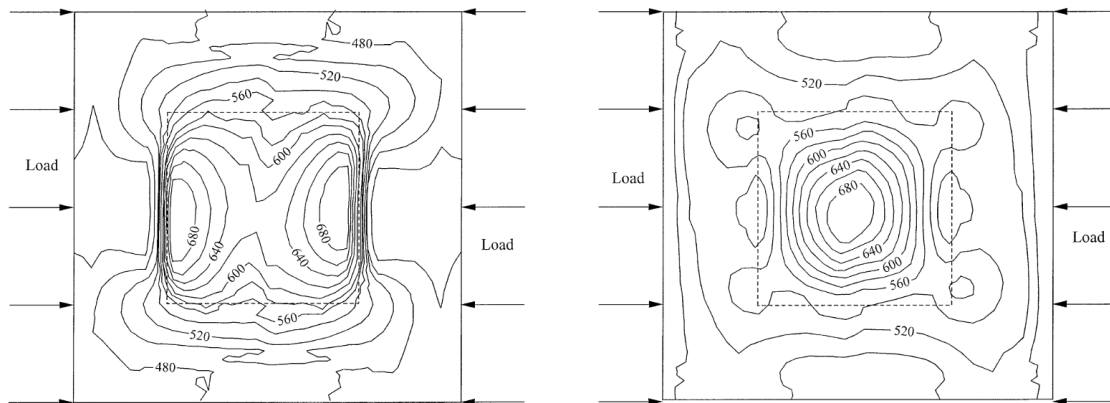


**Figure 2.14:** FE prediction of the maximum compression stress in the fiber direction for local buckling (left) and global buckling (right) in case of a delamination (indicated with a dashed square) [43].

### 2.3.4 Influencing factors

The effect of delamination size and thickness position in cylindrical shells was studied by Tafreshi and coworkers [49–54]. For rectangular delaminations, the critical buckling is shown

in Figure 2.15 and Figure 2.16 for axial compression and external pressure, respectively. For axial compression, a delamination in the middle of the laminate causes the critical buckling load to gradually decrease if the delamination size increases. Delamination length and width have the same influence on the performance reduction. However, for a delamination close to the surface (e.g.  $\bar{h} = 0.1$ ), the width has a more pronounced effect on the critical buckling load, in which the shift from global to local buckling is visible with a steep drop in buckling load. In contrast, for external pressure the lowest buckling load was found for  $\bar{h} = 0.5$ . The critical buckling load is mainly influenced by the normalized delamination length and not by the width. For small delamination areas, the critical load is almost unaffected. Surprisingly, a delamination close to the outer free surface tends to have a negligible effect on the critical load. This effect can be related to the fact that a delamination tends to close rather than open due to an external pressure load [58].

For certain small delaminations, the influence on the critical buckling load is found insignificant, which is in agreement with analytical predictions and observations in flat composite panels [28] and supports the claim that small delamination sizes (i.e. smaller than the critical size) do not affect the structural performance.

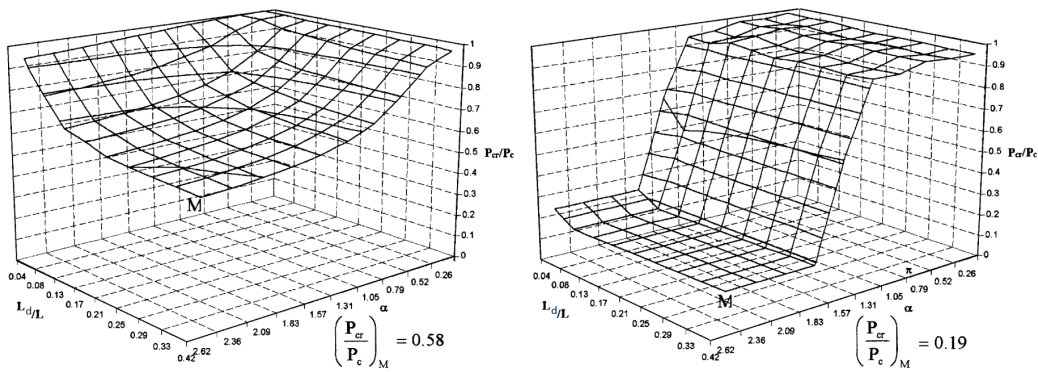


**Figure 2.15:** Effect of a rectangular delamination size on the critical buckling load of composite cylindrical shells subjected to axial compression for thickness positions  $\bar{h} = 0.5$  (left) and  $\bar{h} = 0.1$  (right) [49].

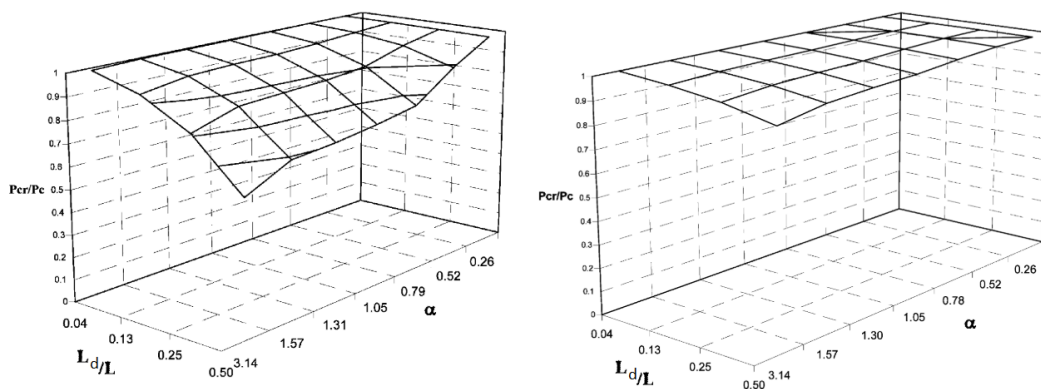


**Figure 2.16:** Effect of a rectangular delamination size on the critical buckling load of composite cylindrical shells subjected to external pressure for thickness positions  $\bar{h} = 0.5$  (left) and  $\bar{h} = 0.1$  (right) [50].

Considering purely in-plane stresses for thick walled cylinders ( $\frac{D}{t} < 20$ ) is not valid, since transverse stresses can be present as well. Kardomateas and Chuch [37] found that transverse stresses do have an adverse effect on a cylinder with a delamination. Moreover, Mistry et al. [59] investigated the failure mode for cylinders with different diameter-to-thickness ratios subjected to a pure hoop stress. Thick walled cylinders showed compression failure (i.e. first ply failure) while thin walled cylinders ( $\frac{D}{t} \geq 20$ ) showed a buckling failure mode. With this, the importance of analyzing both first ply failure and buckling is demonstrated.

If multiple stacked delaminations are considered, multiple buckling loads are present, one for each delaminating layer [47]. Multiple delaminations can have a significant effect on the structural stabilization and the effect increases as the through-the-thickness distance between multiple delaminations decreases, because the thickness of one delaminating layer reduces.

## 2.4 Conclusions

A gap in a composite structure, filled with matrix material, softens the structure and reduces its strength and stiffness. Currently the effect of gaps in TCPs is analytically predicted, but the use of FE modeling is in literature frequently found as more accurate predictions can be made.

In the modeling of gaps, the gap area can be assigned with either reduced laminate properties or matrix properties. The use of matrix properties can be computationally expensive, as the element size has to be small to capture the gap area accurately. Using the defect layer method, the percentage of gap per element is calculated and the properties of the elements are reduced accordingly, diminishing the urge of a small element size.

From the reviewed literature can be concluded that gaps do have an adverse effect on the strength and stiffness of composite laminates. It is however found that fiber out-of-plane undulations and thickness variations are the primary culprits for these reductions. Little literature is present regarding gaps the way they occur in TCPs. On lamina level, reduction in strength and stiffness in the fiber direction varies linearly with the gap width. Also the transverse stiffness and the shear modulus are found to drop when gaps are present. However, literature regarding these type of gaps only considers flat laminates, leaving the more complex structures out of consideration. In general, a clear, universal approach or an indication for the determination of appropriate knockdown factors on a global scale is currently not present.

A delamination is the separation of two adjacent layers in the layup of a composite structure and primarily causes a reduction in compression strength. Analytical failure predictions fall short if more complex systems are considered. Moreover, the contact condition between two delamination surfaces cannot be taken into account. FE modeling is found to be a suitable solution for more accurate predictions. Modeling a delamination in an FE model can be done using untied surfaces between the delaminating layer and the substrate and a contact condition between both.

Multiple failure prediction methods are present in literature. For the analysis of TCPs, based on the geometry and material non-linearity of EGF-HDPE, it is expected that a combination of the non-linear buckling analysis and maximum compression stress allow the assessment of mechanical performance.

Multiple factors have been identified to play a role in delamination failure. The two most prominent factors are delamination size and thickness position. A decrease in buckling load is achieved when the delamination size increases. Two trends have been observed in the effect of a rectangular delamination thickness position on the lowest critical buckling load. For a delamination close to the outer surface ( $\bar{h} = 0.1$ ), the delaminating layer buckles at a relatively low axial compression load due to its low stiffness, despite the high load carrying capacity of the substrate. Load carrying capacity for a delamination close to the outer surface is determined by the material fracture toughness. For a delamination deep in the laminate ( $\bar{h} = 0.5$ ), both substrate and delaminating layer thicknesses are at a minimum, leading to a low critical buckling load when subjected to external pressure, at which the structure buckles in a global mode.

Literature clearly shows a critical delamination size is present, below which a delamination does not affect the performance. This size mainly depends on the aforementioned factors, although the geometry of the structure and the material properties also play a role. With this can be stated that the results from one model cannot simply be copied to another.

## 2.5 Thesis outline

Based on an in-house exploratory research, gaps and voids were identified to be the critical defect types in the production of TCPs and therefore a study regarding their effects on mechanical properties has a high interest.

Current literature often considers brittle, thermoset matrix materials and linear material models. As for TCPs thermoplastic matrix material is used, which show differences in behavior compared with thermoset matrix material, care should be taken to use these findings in the analysis of TCPs. Moreover, the classically used thin laminate theory is invalid to use for thick walled cylinders. It can be stated that the understanding of the effects of gaps and voids on fiber reinforced pipes is still in its infancy.

For a thorough understanding about the effects of defect in TCPs, both short term static and long term behavior need to be understood. For the analysis of long term effects, criteria for damage progression are required and validated methods should be developed. However, the latter was outside the scope of this study. The first step in acquiring a thorough understanding is the evaluation of short term static behavior, which was the aim of this study.

From this, the following research objective was formulated:

*Obtain a thorough understanding of the effects of gaps and voids in TCPs to create a method and tool to assess the mechanical performance reduction in their presence by FE modeling techniques obtained from an extensive literature study and validated by experimental testing.*

The following main research question was formulated to reach the research objective:

*How is the mechanical performance of thermoplastic composite pipes affected by manufacturing-induced gaps and voids and what substantiated criteria can be established for these defects to be allowed in production?*

The motivation of this study was determined by two key factors. First, understanding the effects of defects plays a major role in the integrity management of TCPs during the lifetime. As no structures are produced without (very small) defects, it is of high importance to know at which defect size the performance reduces or the integrity can no longer be guaranteed. Second, when a certain defect size can be allowed in production, repairs are less often required, decreasing the lead time and therefore the costs.

In this work, the effects of defects on AOG product performance are evaluated to establish substantiated criteria for allowable defects in production. In Chapter 3 the impact of gaps and voids is investigated by structural analyses using FE modeling. In Chapter 4 the experimental work is described, for which experimental tests have been conducted on specimens with and without artificial defects. These results are used in Chapter 5 for the validation process of the modeling techniques. With a validated modeling technique, a method and tool are proposed to assess the mechanical performance reduction in TCPs with gaps in a fast and computationally inexpensive way in Chapter 6. Conclusions are drawn and recommendations are made in Chapter 7.

### **Confidentiality**

This thesis has come in two versions, in which the confidential data is excluded from this work.



# Modeling of defects in TCPs

This chapter is dedicated to the modeling and virtual testing of defects in TCPs. Section 3.1 describes the build-up of a TCP FE model, based on a specific TCP definition. In Section 3.2 a gap is modeled in a tensile coupon test, used to validate the modeling technique. The implementation of gaps in a TCP model is described in Section 3.3 and the results for internal pressure are discussed. Next, the effect of voids is studied, considering two load cases. The effect of external pressure is discussed in Section 3.4 and the effect of lateral crushing in Section 3.5, in which the latter is also used for validation purposes. The chapter ends with conclusions in Section 3.6.

### 3.1 TCP model

A TCP model was created, used for the analysis of a defect free situation and serving as a starting point for the models in which gaps and voids were included. A cylindrical coordinate system was used and the geometry was built up in a particular way to obtain a specific mesh. A sophisticated material model was used in the model and boundary conditions were applied. Abaqus version 2019 has been used for all modeling work in this study.

#### 3.1.1 Research TCP definition

For this research, a 6 inch TCP flowline with 40 layers was considered, with a liner and coating thickness (WT) of 8 and 10 mm, respectively. A tape with a thickness of 0.25 mm was considered, resulting in a laminate thickness of 10 mm. The TCP geometry can be found in Table 3.1 and seen in Figure 3.2. The liner and coating material consisted of HDPE and the laminate of EGF-HDPE. The winding angle was determined from the optimum winding angle for pressurized cylinders, which is, according to the netting theory, equal to  $\tan^{-1}\sqrt{2} = 54.74^\circ \approx 55^\circ$  [60].

However, for this study there was a slight deviation from this optimum angle, as the FE modeling was eased if the winding angle ( $\phi$ ) is determined by the diameter ( $D$ ) and the pitch with:

$$\phi = \tan^{-1} \left( \frac{\pi D}{pitch} \right). \quad (3.1)$$

With this, the average winding angle was determined to be  $\pm 55^\circ$  and with a fixed pitch (400 mm), the tape winding angle increased as the laminate thickness increases. Maintaining this pitch, the winding angles varied from  $53.53^\circ$  for layer 1 to  $56.42^\circ$  for layer 40, keeping an average winding angle of  $\pm 55^\circ$ . The winding angle per layer is shown in Table 3.2. The layers were placed in a circular repeating pattern:  $-55/+55/-55/+55\dots$ . It was assumed that the tape width was such that it covered the pipe in one winding ( $400 \sin(55) = 328 \text{ mm}$ ), which might deviate in reality.

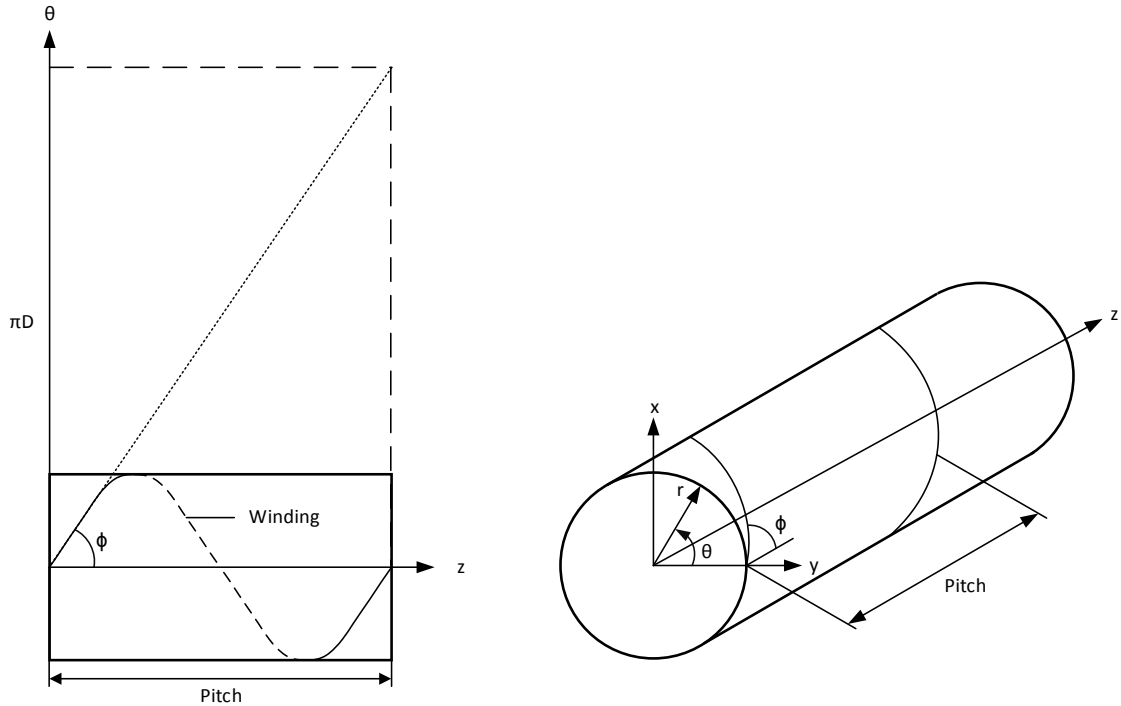


**Figure 3.1:** Schematic determination of the winding angle ( $\phi$ ) over a pipe in 2-dimensional (left) and 3-dimensional (right).

### 3.1.2 Cylindrical coordinate system

A cylindrical coordinate system ( $r, \theta, z$ ) was used, as shown in Figure 3.1 on the right. This coordinate system was used to define the material properties for the lamina, such that the local 11-direction is through-the-thickness, the local 22-direction is perpendicular to the fibers and the local fiber direction is in the 33-direction. This system was adopted to properly represent the material orientation in the layers.

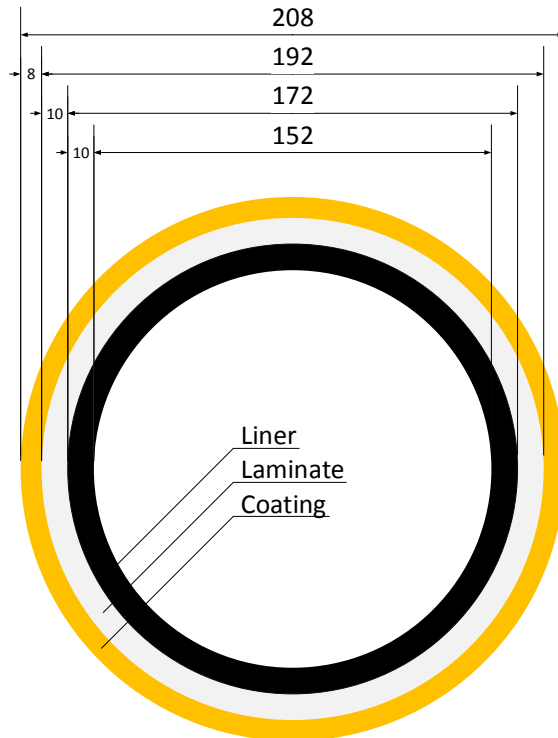


**Table 3.1:** TCP geometry.

Component	Dimension	Value [mm]
Liner	ID	152
	WT	10
Laminate	ID	172
	WT	10
Coating	ID	192
	WT	8
	OD	208

**Table 3.2:** TCP layup laminate.

Layer	WT [mm]	Material	$\phi$ [deg]
L1	0.25	EGF-HDPE	53.53
L2	0.25	EGF-HDPE	-53.61
L3	0.25	EGF-HDPE	53.69
L4	0.25	EGF-HDPE	-53.77
L5	0.25	EGF-HDPE	53.84
L6	0.25	EGF-HDPE	-53.92
L7	0.25	EGF-HDPE	54.00
L8	0.25	EGF-HDPE	-54.08
L9	0.25	EGF-HDPE	54.16
L10	0.25	EGF-HDPE	-54.23
L11	0.25	EGF-HDPE	54.31
L12	0.25	EGF-HDPE	-54.39
L13	0.25	EGF-HDPE	54.46
L14	0.25	EGF-HDPE	-54.54
L15	0.25	EGF-HDPE	54.61
L16	0.25	EGF-HDPE	-54.69
L17	0.25	EGF-HDPE	54.76
L18	0.25	EGF-HDPE	-54.84
L19	0.25	EGF-HDPE	54.91
L20	0.25	EGF-HDPE	-54.99
L21	0.25	EGF-HDPE	55.06
L22	0.25	EGF-HDPE	-55.13
L23	0.25	EGF-HDPE	55.21
L24	0.25	EGF-HDPE	-55.28
L25	0.25	EGF-HDPE	55.35
L26	0.25	EGF-HDPE	-55.43
L27	0.25	EGF-HDPE	55.50
L28	0.25	EGF-HDPE	-55.57
L29	0.25	EGF-HDPE	55.64
L30	0.25	EGF-HDPE	-55.71
L31	0.25	EGF-HDPE	55.79
L32	0.25	EGF-HDPE	-55.86
L33	0.25	EGF-HDPE	55.93
L34	0.25	EGF-HDPE	-56.00
L35	0.25	EGF-HDPE	56.07
L36	0.25	EGF-HDPE	-56.14
L37	0.25	EGF-HDPE	56.21
L38	0.25	EGF-HDPE	-56.28
L39	0.25	EGF-HDPE	56.35
L40	0.25	EGF-HDPE	-56.42

**Figure 3.2:** TCP geometry, in mm.

In Abaqus, the composite layup option was used to account for the individual layers with their respective fiber orientations within a solid element. By default, Abaqus visualizes stresses in their local coordinate system, meaning the fiber stress in the TCP model is denoted by  $S33$ .

### 3.1.3 Geometry

A solid pipe of 1000 mm was extruded in Abaqus/CAE with the inner diameter (ID) and outer diameter (OD) of the TCP. Within this pipe, 1 mm circular sections were created in the part representing the TCP laminate. To represent the way in which gaps and voids occur, helical shells were revolved around the center axis of the pipe with a thickness equal to the TCP (indicated in red in Figure 3.3). Using Equation (3.1) with a pitch of 400 mm, 2.5 revolutions were made within the model and the orientation of the helix matched the fiber orientation in each layer.

Using this method, the elements in the central section of the pipe followed the orientation of the helix, and hence the winding angle of the  $+\phi$  layers. For this reason the winding angles of the TCP slightly deviated from  $\pm 55^\circ$ . To obtain a proper mesh at the pipe ends was a tedious and time consuming practice, leading to a less structured mesh in these areas. To ease the meshing, on one side of the pipe the helix was stopped at one of the longitudinal quarter-sections. As the point of interest is within the mid-section of the model, these factors are of no major concern. In the model, continuum solid (C3D8R) elements were chosen, as this element type is preferred in TCP modeling [61]. Note that with this approach only gaps and voids can be created in the  $+\phi$  fiber orientation.

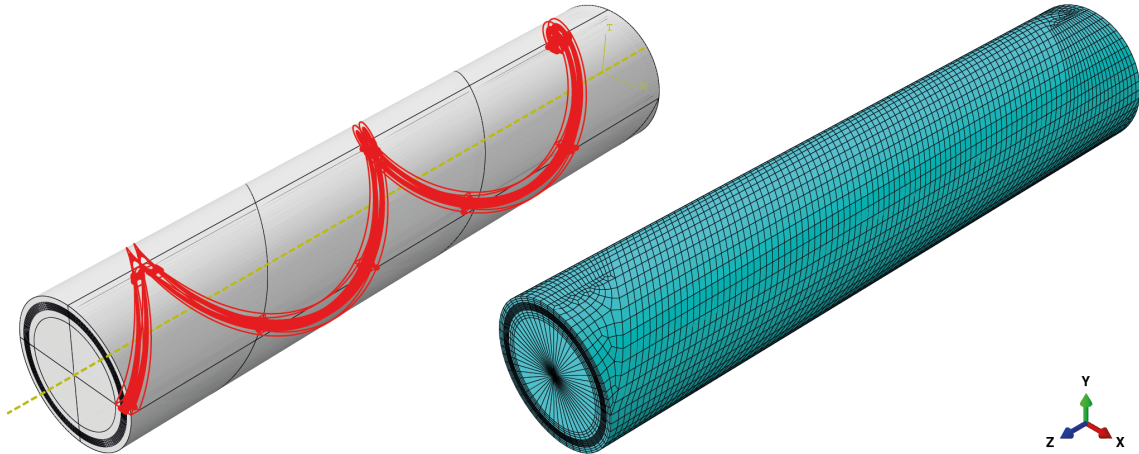


**Figure 3.3:** FE TCP model with a helix definition (left) and the associated mesh representing the winding angle of the  $+\phi$  layers (right).

### 3.1.4 Material

The material response of glass fibers is usually linear-elastic while the material response of thermoplastic polymers is visco-elastic, causing the composite material to behave in a non-linear way. To simulate these properties, a non-linear material model was used. For this, the non-linear material properties are obtained using a meanfield homogenization material

model, which is performed using the material properties of the constituents in a multi-scale material model. In essence, for meanfield homogenization the composite is considered as a two phase material, where continuous fibers of a given volume/mass fraction are assumed to be embedded in the matrix. Based on the constitutive models of both the fibers and the matrix, the macroscopic mechanical behavior of the composite is approached [62]. The material was introduced in the FE model to get the response of each ply.

In the model, a solid composite layup was used with multiple plies per element.

### 3.1.5 Boundary conditions

Rigid body motions were avoided by constraining the motion of one of the pipe edges. An endcap was modeled on one end of the pipe, while symmetric boundary conditions were applied to the other edge in order to simulate a continuous pipe. The endcap causes an axial load component to be present if pressure is applied, while taking the change in diameter into account. For the symmetric boundary conditions, the longitudinal displacement was restricted, while radial and tangential displacements were allowed.

## 3.2 Tensile specimen with gaps

As a validation process, tensile specimens were modeled, physically manufactured and experimentally tested. The manufacturing and testing of these specimen is discussed in Chapter 4 and the validation between the modeling and experimental results in Chapter 5. The reason tensile coupon tests have been performed is the fact that these can fairly easily be manufactured and tested, while a gap can be introduced in a similar way as gaps are present in TCPs, that is, in the  $0^\circ$  layers. Moreover, the strength decrease due to gaps is expected in the fiber dominated properties, as shown by Heinecke et al. [15].

### 3.2.1 Model

For this, an FE model was created as shown in Figure 3.4. In order to create a computationally inexpensive model, only a part of the gauge section was modeled and symmetry boundary condition were used. By restricting the displacement direction  $z$  in the  $xy$ -plane at the back-right side of the model, direction  $x$  in the  $yz$ -plane on the back-left side of the model and direction  $y$  in the  $xz$ -plane at the bottom of the model only  $1/8^{th}$  of a part of the gauge section had to be modeled.

The stacking sequence for the specimen was  $[(90/0)_2]_s$ , where the  $0^\circ$  layers correspond to the  $z$ -direction. The nominal width and thickness of the specimen were 25 and 2 mm, respectively. However, as these specimens have been manufactured and tested (Chapter 4), the dimensions of the model were adjusted to the average as-built dimensions to increase the accuracy for the validation process. The length of the FE model was 12.5 mm, representing a gauge section of 25 mm. Four plies, half the specimen thickness, were modeled, each ply having one element through-the-thickness. Load was introduced in a reference point, which was coupled to the cross-sectional area. In this way the load was equally distributed over the cross-sectional area of the specimen.

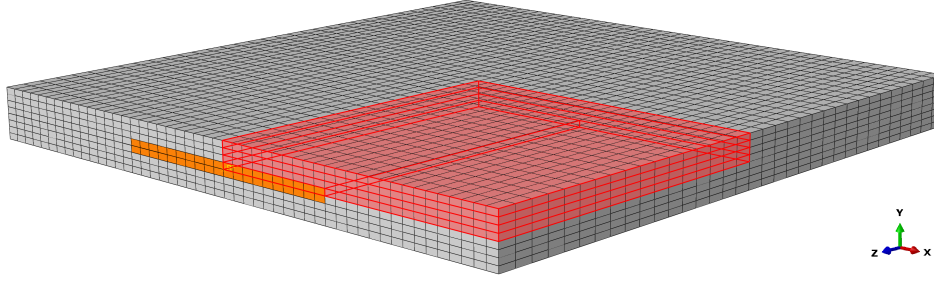


**Figure 3.4:** FE tensile model. The modeled section is highlighted in red and the section indicated in orange is used to assign gap properties to. Load is applied in the  $z$ -direction.

Two models were created: 1) a defect free model and 2) a gap model. In the defect free model, the composite layers were assigned with EGF-HDPE material properties, as described in Section 3.1.4. For the gap model, a 5 mm section was created in the bottom layer of the model, indicated in orange in Figure 3.4. Neat HDPE material properties were assigned to this section, representing a gap area.

### 3.2.2 Results

From the defect free and gap models, both the Young's modulus and tensile strength were obtained and used in Chapter 5 to compare with the experimental results. The obtained property differences are presented in Table 3.3.

**Table 3.3:** Predicted  $E$ -modulus and failure load difference for the gap model with respect to the defect free model.

	$E$	$P_{max}$
Difference	-18.2 %	-21.1 %

#### Young's modulus

For the determination of the Young's modulus a displacement load was applied to the models. Subsequently, the reaction force of this displacement load was obtained. The  $E$ -modulus was calculated by dividing the tensile stress ( $\sigma$ ) by the axial strain ( $\epsilon$ ) with:

$$E = \frac{\sigma(\epsilon)}{\epsilon} = \frac{\frac{F}{A}}{\frac{\Delta L}{L_0}} = \frac{FL_0}{A\Delta L}, \quad (3.2)$$

where  $F$  is the reaction force,  $A$  is the original cross-sectional area and  $L_0$  and  $\Delta L$  are the respective original length and length increase. With this, the  $E$ -modulus was determined using the engineering tensile stress at an axial strain between 0.1-0.3 %, in which the stress response was assumed to be linear, as shown in Figure 3.5. The decrease in stiffness for the gap model compared with the defect free was predicted to be 18.2 %.

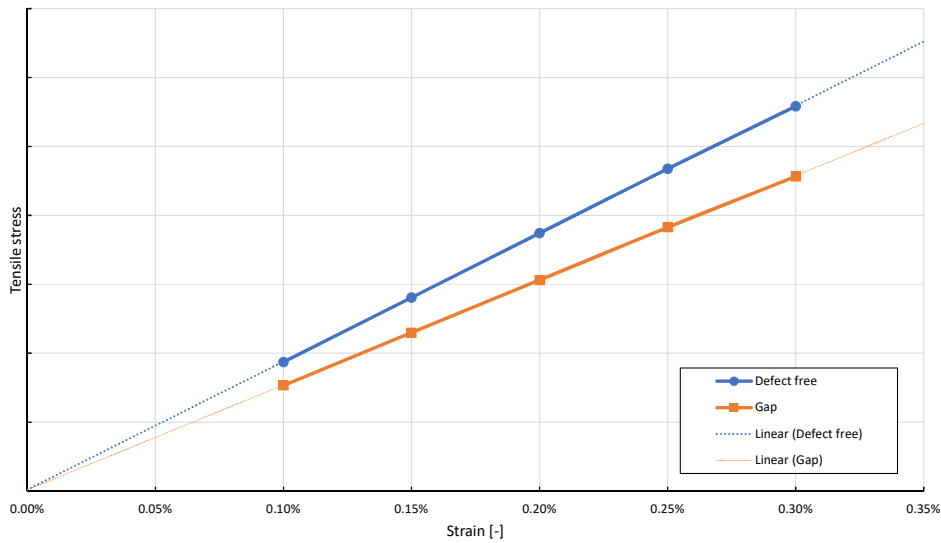


Figure 3.5: Stress strain plot for the defect free and gap model to determine the  $E$ -modulus.

### Tensile strength

To predict the tensile strength, it should be known at what stress failure occurs. For this, the experimentally obtained mean maximum load (Section 4.1.4) for the defect free specimens was used. The UD-ply strengths were obtained from the defect free FE model by evaluating the ply stress corresponding to the experimental failure load. The maximum true fiber tensile stress obtained with this procedure was considered to be the stress at which the material failed.

To predict the failure load of the gap model, load was introduced until the obtained failure stress was exceeded. The corresponding load was considered to be the failure load and compared with the failure load of the defect free specimens, yielding a decrease of 21.1 %. The decrease in strength, i.e. the increase in fiber stress, is shown in Figure 3.6, in which an equal amount of load is applied to both models. In the gap model it can be observed that the stress in the gap section is reduced and evenly redistributed over the remaining  $0^\circ$  plies.

## 3.3 TCP model including gaps - internal pressure

A validated gap modeling technique (Chapter 5) allows a reliable assessment of the effect of gaps in TCPs. As gaps affect the fiber driven parameters in terms of strength, an internal pressure load case was considered for this work, in which the fiber tensile stress is the failure driven parameter.

### 3.3.1 Internal pressure load case

An internal pressure of 350 bar was applied to the inner surface of the pipe as shown in Figure 3.7. Note that due to the endcap, the application of internal pressure results in an additional axial tensile force acting on the pipe as well. An endcap is used to account for the axial loads which are present in a (physical test of a) pipe with a finite length.

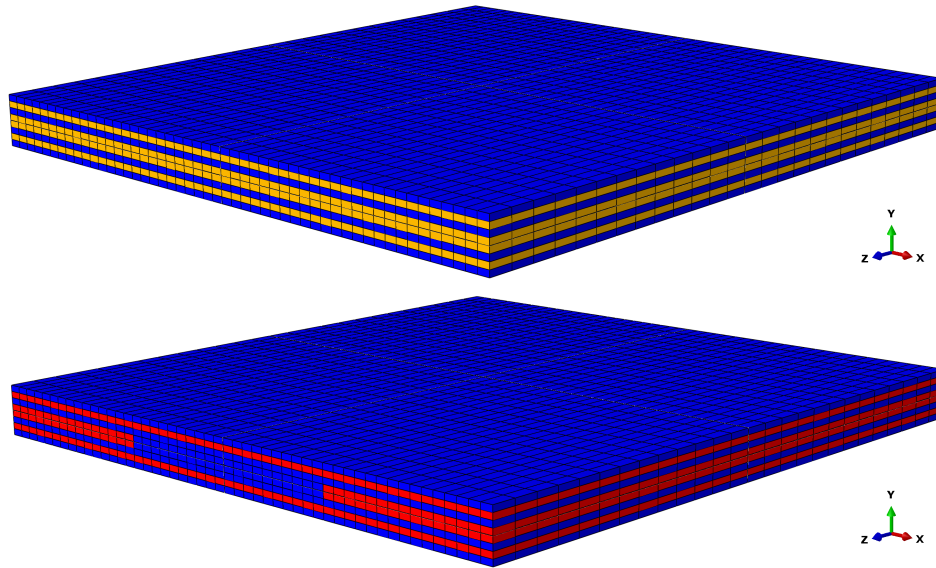


**Figure 3.6:** Visualization of the fiber tensile stress in the gauge section of a tensile coupon for the defect free model (top) and the gap model (bottom) for the same applied load. The contour colors represent the stress value with red and blue being the high and low (or negative) values, respectively.

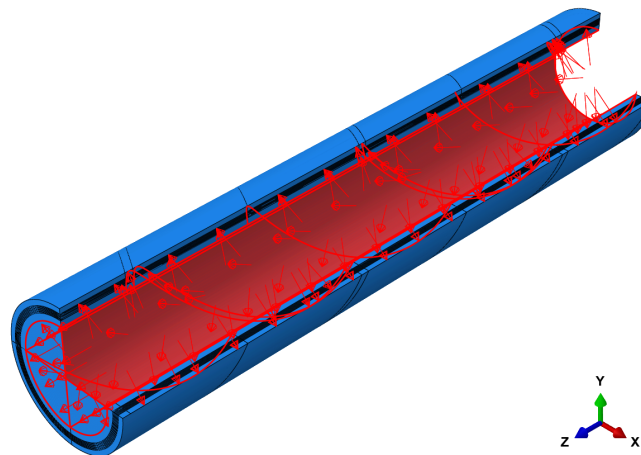


**Figure 3.7:** The application of internal pressure.

### 3.3.2 Mesh convergence study global model - defect free

A mesh convergence study has been conducted to find a mesh size that satisfactory balances accuracy and computational costs. For this, six different meshes were created with varying average element sizes, with mesh 1 having the largest average element area and mesh 6 the smallest, as shown in Table 3.4. The amount of radial elements was fixed for every model, with three elements through-the-thickness of the liner and coating and 10 for the circular sections, in which each element represented four composite layers. In the mesh sequence, the amount of elements in the circumferential direction increases and the average longitudinal element length decreases, in such a way that the aspect ratio of the elements is roughly maintained.

Each model was analyzed and the maximum fiber tension stress was obtained. This value was compared with the obtained value for the finest mesh (mesh 6). The maximum fiber tension stress for mesh 3 was within 99.9 % of the finest mesh and was therefore considered to be converged.

**Table 3.4:** Helix mesh convergence study baseline global model.

	Mesh 1	Mesh 2	Mesh 3	Mesh 4	Mesh 5	Mesh 6
Radial elements	16	16	16	16	16	16
Circumferential elements	24	36	48	60	72	96
Avg. longitudinal element size [mm]	20	15	10	8.75	7.5	5
Avg. element area [mm <sup>2</sup> ]	476	238	119	83	59	29
Aspect ratio	0.84	0.94	0.84	0.92	0.94	0.84
Absolute difference with respect to mesh 6 [%]	0.673	0.142	0.088	0.062	0.000	-

### 3.3.3 Submodel - defect free

The previous described model is an efficient way to predict the maximum fiber stress without the need of a computational expensive mesh. However, to increase the accuracy of the results, and in particular when localized defects are modeled, the mesh size needs to be further reduced. Although the stresses per ply can be extracted when a solid composite layup is used with multiple plies per element, having one element per ply increases the accuracy. Furthermore, there is a lack of accuracy in the ply responses within one element if different material properties are used.

To facilitate the desired increase in accuracy, a submodeling technique was used. The previous described model was used as the so called global model, which drive the submodels. The converged mesh size (mesh 3) was used. Figure 3.8 shows the development of a submodel, for which a part of the mid-section of the global model was used, with an angle of 45° of the circumference and a length of 137 mm. A node-based submodel technique was adopted, such that the sides of the submodel used the displacements at that location of the global model.

In this submodel, the amount of circular shell sections was increased to 40, one for each layer. Again a mesh convergence study was performed for five different meshes, as shown in Table 3.5. All mesh sizes showed results that were within 99.9 % of the finest mesh (mesh 5), as expected, since all mesh sizes were smaller compared with the converged mesh size of the global model. From these submodels the most accurate fiber tensile stress was determined, extracted from the model having the finest mesh. This value served as the defect free value which the gap models were compared to.

### 3.3.4 TCP model including gaps

For the analysis of gaps, HDPE material was assigned in the composite layup to the helical sections containing a gap in the model, following the winding angle of the  $+\phi$  layers. In this

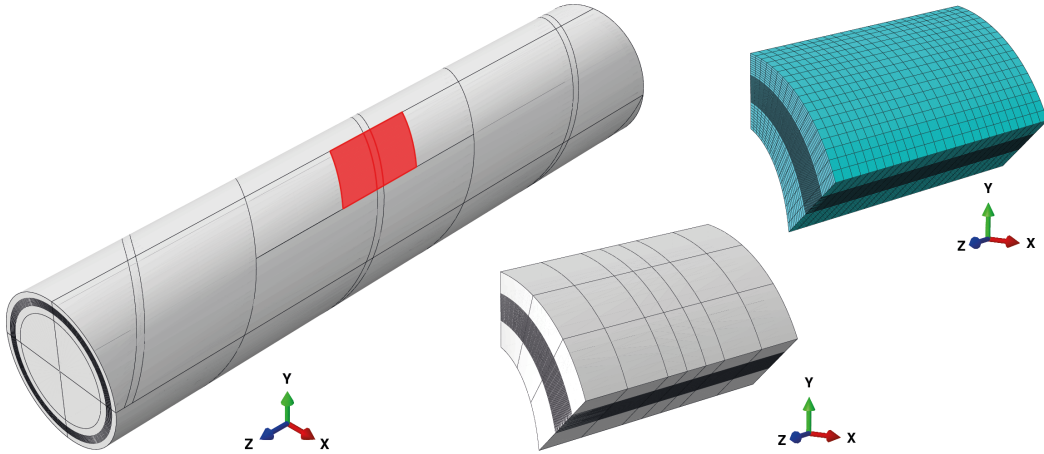


**Figure 3.8:** Global TCP model with the submodel location indicated in red (left), the submodel part (middle) and its converged mesh size for gaps (right).

**Table 3.5:** Helix mesh convergence study baseline submodel.

	Mesh 1	Mesh 2	Mesh 3	Mesh 4	Mesh 5
Radial elements	60	60	60	60	60
Circumferential elements <sup>1</sup>	9	12	18	36	87
Avg. longitudinal element size [mm]	10	7.5	5	2.5	1
Avg. element area [mm <sup>2</sup> ]	100	56	25	6	1
Absolute difference with respect to mesh 5 [%]	0.049	0.001	0.002	0.002	-

<sup>1</sup> The amount of elements used in the submodel, corresponding to 1/8<sup>th</sup> of the TCP circumferential.

way the gap area was exactly captured by the elements, as shown in Figure 3.9, which is a key factor for accuracy [17, 18]. The orientation of these HDPE sections could be disregarded, as the matrix material has isotropic material characteristics.

With this serving as a basis model, for each gap configuration a separate model was created. First, global models have been analyzed, after which for each gap configuration a submodel was created and analyzed with the corresponding global model as input. A separate global model for each case was required to obtain the correct global stiffness response of the TCP.

While for the global model with gaps the mesh size of the defect free model had been used, for the submodel with gaps again a mesh convergence study was performed, as it was found that smaller elements were required when local defects are present. An important difference in this study is that not the maximum fiber tensile stress of the whole model was used, but the maximum values of each composite layer were compared. This because it was found that the maximum value for different mesh sizes can be located in different layers. If the mesh size becomes very small (in the order of a few millimeters), the elements in the layers above and under the gap area tend to deform towards the gap, as less stiffer material is used here. This is a non-converging phenomenon and lead to numerical stress peaks. For the aim of this



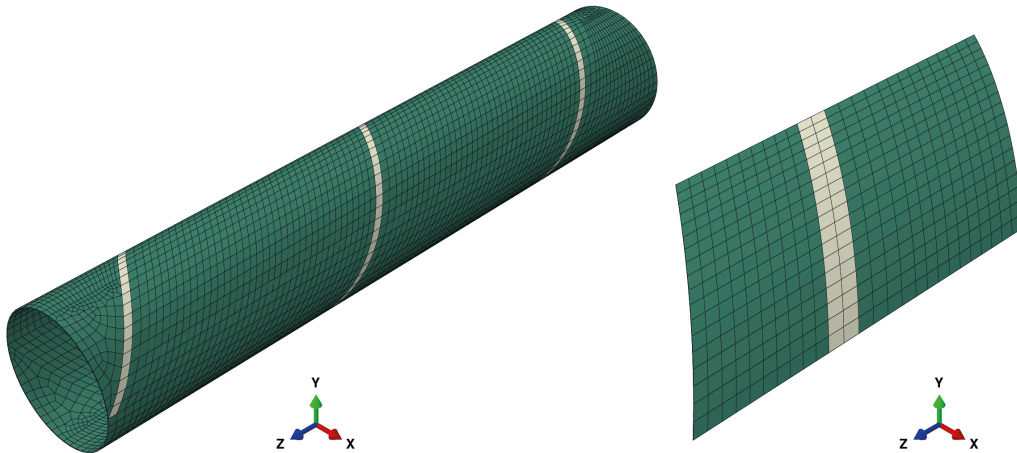


**Figure 3.9:** Representation of a 10 mm gap in a global TCP model (left) and the corresponding submodel (right), in which green represents the defect free material and beige the gap. For clarity only the element layer which includes the gap is shown.

study this phenomenon was left out of consideration, as macro gaps were of primary interest. The mesh convergence study was conducted for a 10 mm gap in layer 21 and it was found the model converged for an element size equal to  $25 \text{ mm}^2$ , as shown in Table 3.6. Two elements through the gap width were present for this mesh size, which is shown in Figure 3.8 on the right.

For gaps larger than or equal to 10 mm, this element size was used, while a smaller element size was used for smaller gaps. The downside of the latter is that the earlier discussed phenomenon, stress peaks at the gap edges, occurred. Therefore the values of interest were extracted from the models including gaps smaller than 10 mm by disregarding the stress peaks at the edge of the gaps.

**Table 3.6:** Helix mesh convergence study submodel including a 10 mm gap in layer 21.

	Mesh 1	Mesh 2	Mesh 3	Mesh 4	Mesh 5
Radial elements	60	60	60	60	60
Circumferential elements <sup>1</sup>	9	12	18	36	45
Avg. longitudinal element size [mm]	10	7.5	5	2.5	2
Avg. element area [ $\text{mm}^2$ ]	100	56	25	6	4
Max. absolute difference in S33 with respect to mesh 5 [%] <sup>2</sup>	0.163	0.200	0.063	0.076	-

<sup>1</sup> The amount of elements used in the submodel, corresponding to  $1/8^{\text{th}}$  of the circumferential.

<sup>2</sup> Maximum difference between each of the 40 layers.

### 3.3.5 Results

Different aspects have been studied: the effect of a gap in general, the size, the thickness position and the effect of multiple gaps.

#### Effect of a gap

Compared with a fiber cut, a gap will not result into a stress concentration because the load path is not interfered by having fibers cut through. Figure 3.10 shows the fiber tension stress state for a global TCP model having a 10 mm gap in layer 21. In the figure on the left, the response of the layer having the gap is shown. The continuous gap following the winding angle does not have load carrying capacity and is therefore indicated in blue in the contour plot. In the defect free layers, a distinction can be made between the layers having the same winding angle as the gap layer and layers having the opposite winding angle. While the gap only has a minor effect on the layers having the opposite winding angle, a significant stress increase is observed in the layers having the same winding angle as the gap layer. This increase is primarily at the same longitudinal position and reaches its maximum right below or on top of the gap layer, as indicated in the figure on the right.

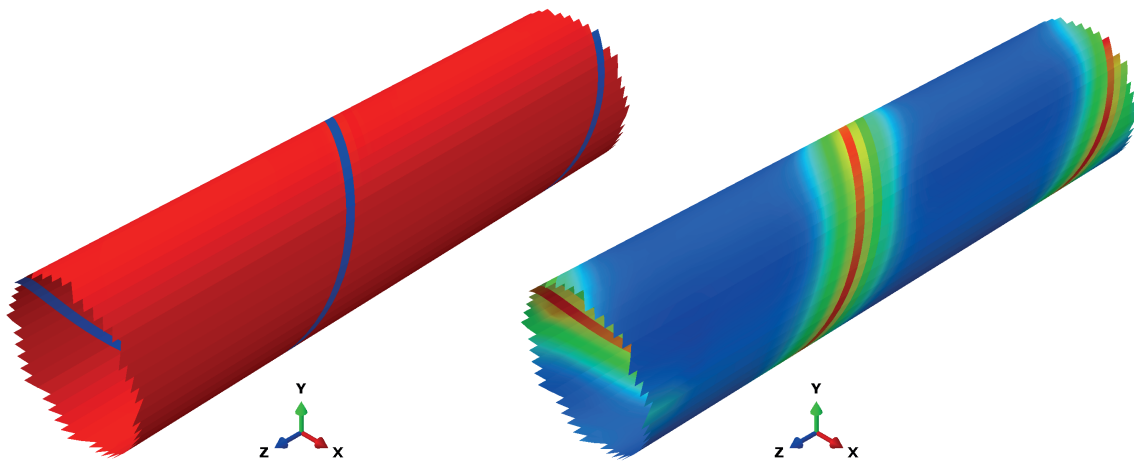


**Figure 3.10:** Visualization of the fiber tensile stress in layer 21 (left) and the other uneven layer numbers (right) for a 10 mm gap in layer 21. The contour colors represent the stress value with red and blue being the high and low (or zero) values, respectively. The colors in both situations are relative to the stress in that layer, i.e. the red color represent a different value in both figures.

Compared to the submodels, these global models gave in general similar predictions of the fiber stress in the far field and through-the-thickness of the laminate, provided that for the latter the gap layer and layer of interest were not within one element. With a gap layer and the critical layer within one element, the global model predicted a stress decrease instead of increase, which contrasts the expectation (based on the tensile coupon tests) and the submodeling predictions. Therefore the use of submodeling is required to study the effect of gaps on a more local and smaller scale. The fiber tensile stress response of the submodel belonging to the global model in Figure 3.10 is shown in Figure 3.11. Here, the gap layer together with the two adjacent layers below are shown. The fibers next to a gap within the gap layer experience a small increase in stress, which is mesh size sensitive. The earlier stated

minor stress increase in the layers having the opposite winding angle compared with the gap layer, is substantiated with the result shown in the figure; the stress increase in the gap layer is already larger compared with the layer below with the opposite winding angle. Moreover, examining layer 19, the stress in the ply having the same winding angle as the gap layer outnumber the increases in both layers 20 and 21.

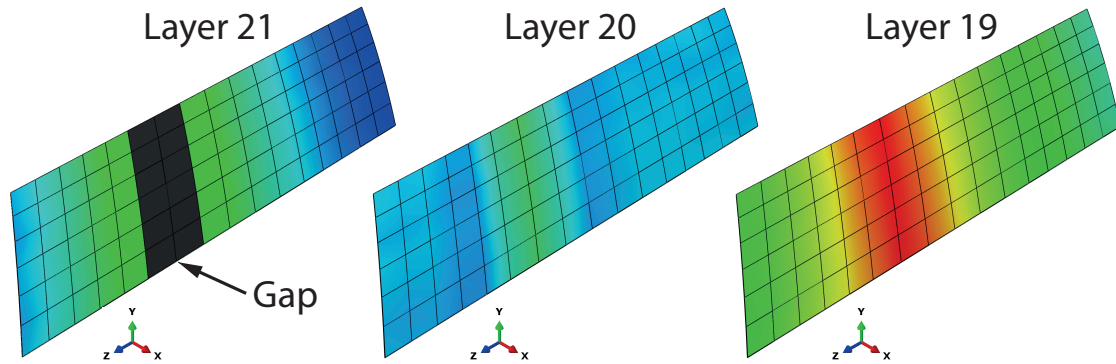


**Figure 3.11:** Visualization of the fiber tensile stress in layer 21 (left), 20 (middle) and 19 (right) for a 10 mm gap in layer 21. The contour colors represent the stress value with red and blue being the high and low (or zero) values, respectively. One color scale is used for the layers.

The fiber stress through-the-thickness for both the defect free model and the gap model are shown in Figure 3.12. The stress distribution through-the-thickness is as presented in Appendix A, with layer 1 being the layer carrying the highest load and layer 40 the lowest. In the figure, the maximum fiber tensile stress per layer is also shown for the above discussed model with a 10 mm gap in layer 21, causing an increase in stress for each layer. In fact, each layer with the same winding angle experiences, percentage wise, in general an equal increase, as shown in Figure 3.13. This means the stress in layer 1 increases even if a gap is present in layer 39 and vice versa. In this example the largest increase is observed in layer 19, the first higher loaded layer next to the gap layer having the same winding angle. This largest increase in the first layer having the same winding angle with a higher load compared with the gap layer is also observed for gaps in different layers than 21. Similar plots can therefore be reproduced for each gap size and location.

The most important observation is the fact that the percentage stress increase in layer 1 equals the percentage of global performance reduction of the TCP, as this is the most critical layer.

### Effect of gap size and thickness location

Both gap size and thickness position are of importance in the amount of performance decrease and their influence is shown in Figure 3.14. In the figure the maximum fiber tension stress increase is plotted, which is, except when a gap in layer 1 is considered, in layer 1. For a gap in layer 1 the maximum fiber stress was found to be located in layer 3.

In terms of gap width, widths varying from 2 mm to an infinite width, in which the entire layer was modeled with matrix material, were studied. The stress increase for gap widths from 2 to 30 mm are shown in Figure 3.14. It was found that the stress increase is linearly proportional to the gap width. To assess the effect of a gap width of 2 mm in layer 3, a smaller

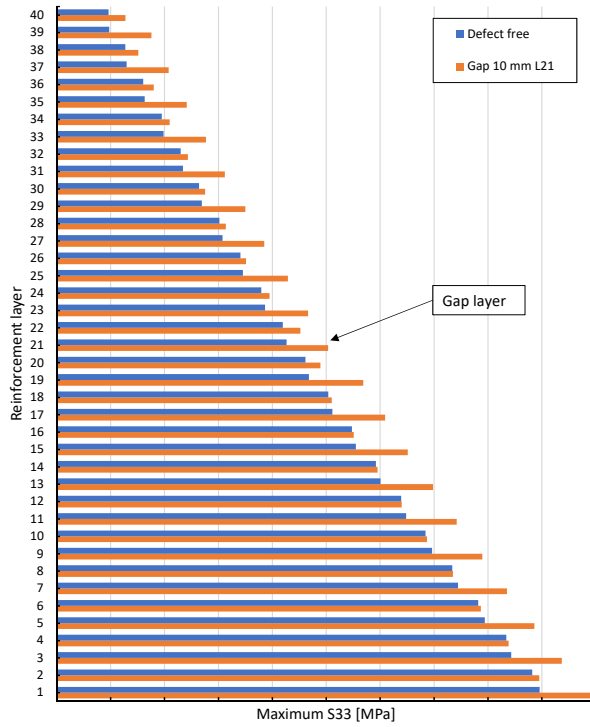


**Figure 3.12:** Fiber tensile stress per layer for the defect free model and a 10 mm gap in layer 21. Note:  $x$ -axis does not start at zero.

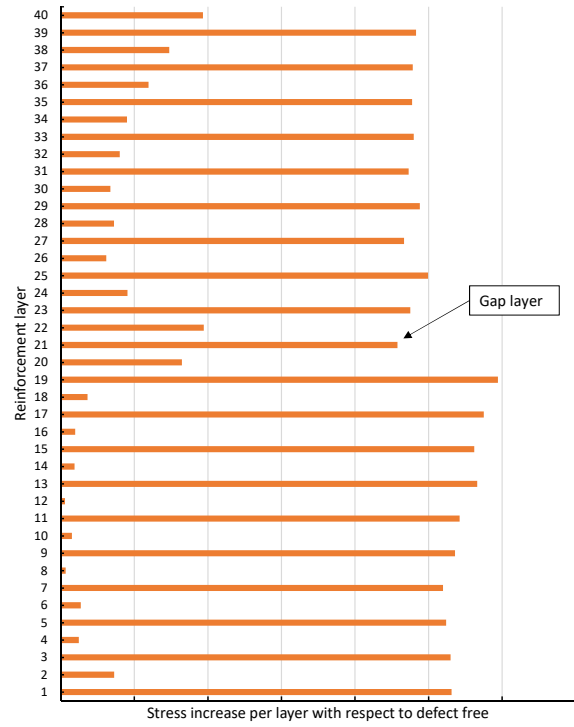


**Figure 3.13:** Stress increase per layer for a 10 mm gap at layer 21 compared with the defect free model.

mesh size was required to have multiple elements in the gap area, which in turn caused stress peaks at the gap edges for the same reason as discussed before in Section 3.3.4. Therefore a prediction of the maximum stress increase for this gap size in layer 3 is left out in the plot. In addition, extrapolating the curve for a gap in layer 3 would yield a non-zero value, indicating that some non-linearity in the stress response will be present. Assessing the effect of such small gaps causes numerical difficulties. For the other extreme, having a infinite large gap, the fiber stress increases are shown in Table 3.7 and cause a performance reduction of roughly 5 %. This is not unexpected and in agreement with the removal of 1/20<sup>th</sup> of the layers in one direction. A slight increase on top of the 5 % is however present if a low layer, i.e. layer 3, is considered to be the gap layer.

**Table 3.7:** Maximum fiber stress increase of an infinitely large gap.

	layer 1	layer 3	layer 21
Maximum S33 increase	4.68 %	5.40 %	4.99 %

Although in general the stress increase due to a gap is roughly equal in each layer having the same winding angle, the adjacent layer below a gap having the same winding angle experiences a slightly larger increase. With this can be said the second highest loaded layer having the same winding angle as the highest loaded layer is the most critical in having a gap. As in the configuration layer 1 is the highest loaded with layer 3 being the next highest loaded layer

among the remaining layers having the same winding angle, layer 3 is the most critical in having a gap.

A gap in layers higher than 3 result in similar curves in the plot, running parallel but slightly lower to the curve of a gap in layer 3.

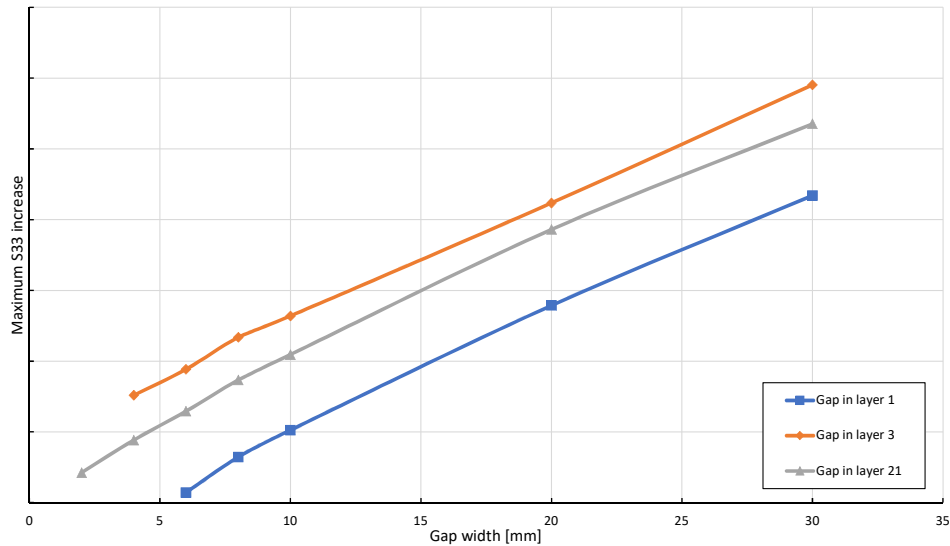


**Figure 3.14:** Increase in maximum fiber tension stress for different gap widths and thickness positions.

### Effect of multiple gaps

As a gap has an equal effect on all layers having the same winding angle, it is therefore of no surprise the maximum stress increase multiplies with the number of overlapping gaps. The stress increase for a single gap in layer 3, as well as an additional gap in layer 5 are shown in Figure 3.15. This effect is however exclusively apparent if multiple gaps are exactly on top of each other. The stress rapidly decreases if multiple gaps are not overlapping. The longitudinal distance between two gaps, as indicated in Figure 3.16, is of importance. If multiple gaps are located adjacent to each other, but in different layers, the stress response is similar to one gap having a width equal to the sum of the adjacent gaps. In the figure it is shown that for a longitudinal distance of more than 60 mm between two gaps the effect of both does not reinforce each other. While 60 mm is enough for a 10 mm gap, this distance is lower for smaller gaps; up to 40 mm for 2 mm gaps. On the other hand, for wider gaps (20 and 30 mm) the effect of multiple gaps is also negligible after a longitudinal distance of 60 mm.

## 3.4 TCP model including voids - external pressure

In this section the effect of voids on the TCP behavior is studied. An external pressure load case was assumed for this, as this load case is identified to be critical in cylinders containing delaminations [49–54]. The analysis of this load case varies from that of internal pressure. While for internal pressure a perfect cylinder was assumed, this is not possible in the analysis

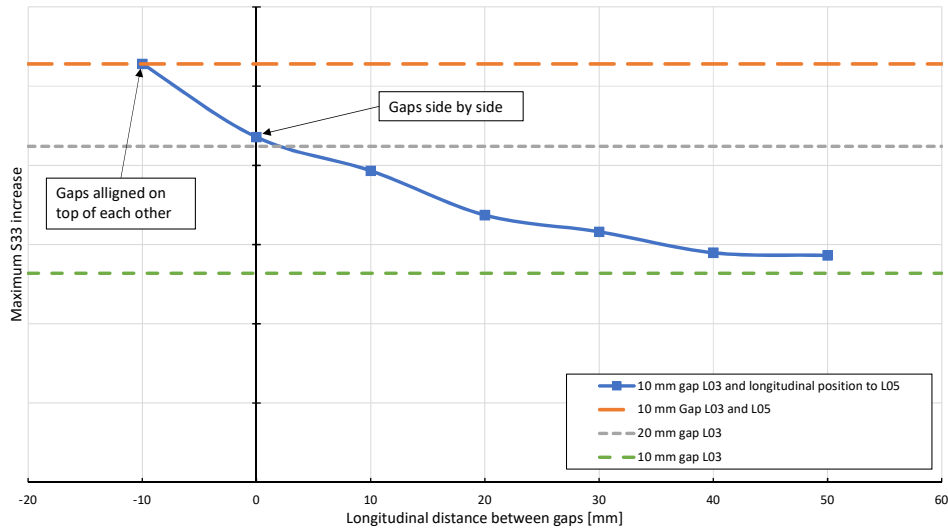


**Figure 3.15:** The effect of longitudinal distance between two gaps on the increase in maximum fiber tension stress.

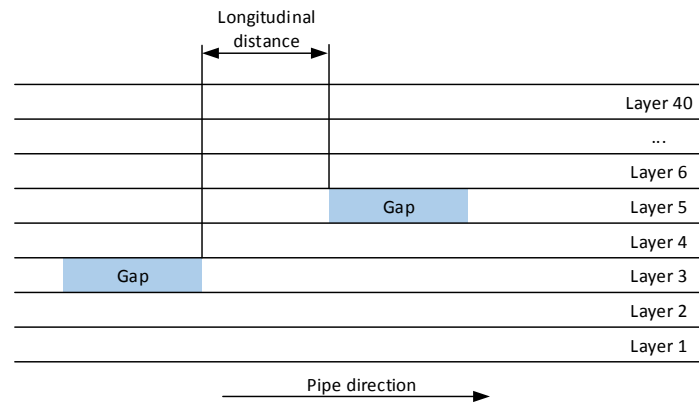


**Figure 3.16:** Schematic representation of the cross-section of the laminate in the longitudinal direction with a gap in layer 3 and in layer 5.

of external pressure. In a perfect cylinder the hoop stress induced by the external pressure tend to cancel each other, resulting in a high order buckling mode and an overestimated buckling pressure. Therefore, an imperfection in the model is required to allow buckling in the first mode.

The following steps have been performed in the analysis of external pressure, which are discussed in more detail in the following sections:

- Step 1: TCP model including voids
- Step 2: Linear buckling analysis
- Step 3: Geometric imperfection in the model
- Step 4: Non-linear buckling analysis

### 3.4.1 TCP model including voids

For the analysis of voids, a defect free reference model and models including delaminations were created. For the delaminations, a width of 30 mm and a finite length of 200 mm was considered, as highlighted in red in Figure 3.17 on the left. This size is exceptionally large and does not occur in the manufacturing of TCPs. The modeling technique as described in Section 2.3.2 was used. For this, the TCP model as described in Section 3.1 was recreated consisting of two separate parts, one being the TCP without the delaminating layer and one being the delaminating layer, as shown in Figure 3.17 on the right. These two parts were assembled and connected using tie constraints on the sides. In the delamination a contact condition between the two surfaces was defined, allowing the surface of the delaminating layer to open, whilst restricting penetration. In addition, the symmetry edge was removed and an extra endcap was modeled, resulting in a finite length of 1000 mm. Global mesh size 3 (Table 3.4) was used, as this size was found to converge for global TCP models.

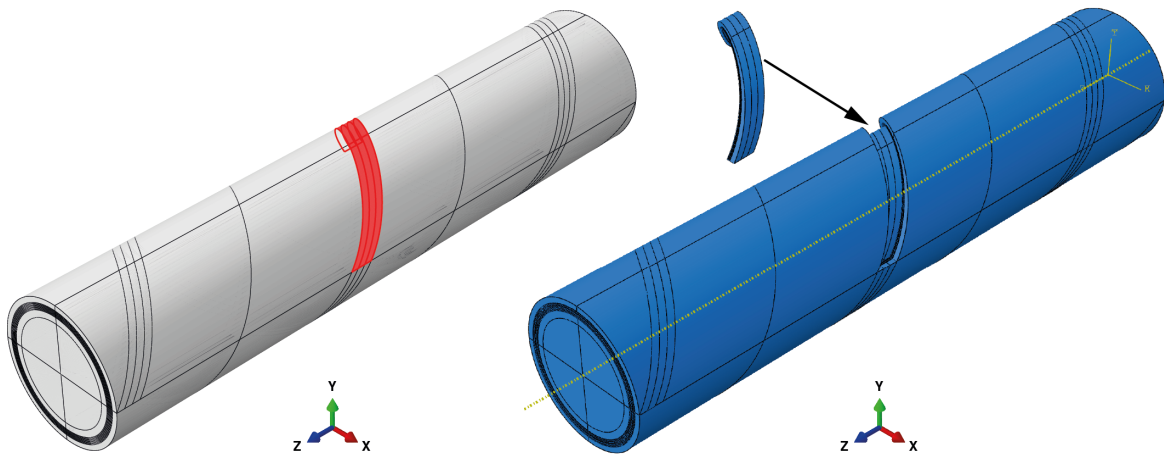


**Figure 3.17:** Location of the delamination area on the TCP (left) and the modeling technique of a delamination (right).

As the thickness position can have an effect on the buckling response [49–54], three different thickness positions were considered: 1) between layers 36 and 37 ( $\bar{h} = 0.1$ ), 2) between layers 20 and 21 ( $\bar{h} = 0.5$ ) and 3) between layers 4 and 5 ( $\bar{h} = 0.9$ ).

### 3.4.2 External pressure load case

An external pressure was applied to the outer surface of the TCP as shown in Figure 3.18. Note that due to the endcaps, the application of external pressure results in an additional axial compression force acting on the pipe as well. The endcaps are used to account for the axial loads which are present in a (physical test of a) pipe with a finite length.

### 3.4.3 Linear buckling analysis

A linear perturbation analysis was performed for each model to predict the buckling modes and corresponding eigenvalues. The endcaps in these models forced the buckling to be located in the mid-section of the TCP model.



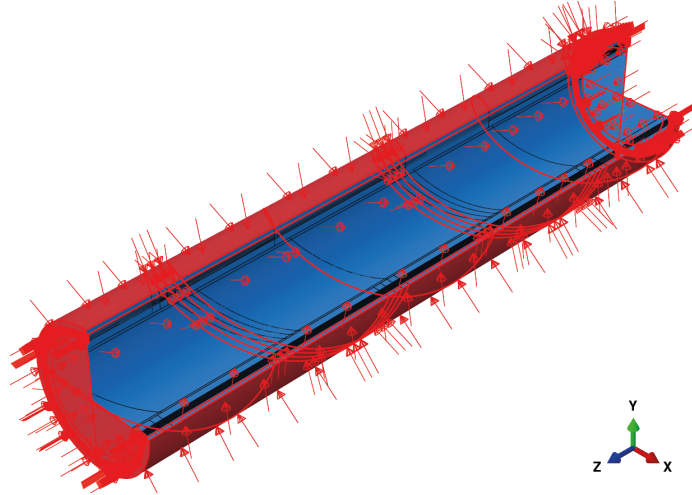


**Figure 3.18:** The application of external pressure.

It was observed that global buckling occurred for each model in a first buckling mode, having an elliptical shaped cross-section at the center as shown in Figure 3.19. Based on this buckling behavior, the location of the delamination was chosen to be in the upper section of the TCP, as the fiber compression stress reaches the maximum there.

### 3.4.4 Geometric imperfection

An initial imperfection was geometrically introduced in the models and based on the elliptical shaped cross-section of the first buckling mode. An ovality of 0.1 % was used to force the TCP to buckle in the first buckling mode. The ovality was calculated with:

$$ovality = \frac{D_1 - D_2}{D_1 + D_2} 100 \%, \quad (3.3)$$

where  $D_1$  and  $D_2$  represent the major and minor axis of the ellipse, respectively.

For the ease of the helix model, the ovality was determined based on the location of the first reinforcement layer. The diameter in the perfect circular condition was 172 mm and in the new condition the diameters representing the vertical (major) and horizontal (minor) diameters became 172.15 and 171.8 mm, respectively. The ID of the liner and OD of the coating were remained unchanged, causing small variations in thickness of these components. As these components do not contribute to the load carrying capacity of the TCP, these small changes does not significantly affect the results.

### 3.4.5 Non-linear buckling analysis

Non-linear buckling analyses were performed for an applied external pressure of 150 bar. The critical limit point (Section 2.3.3) for the models were found using Newton's method, which is the default solving technique for non-linear equilibrium equations in Abaqus [63], disregarding the post buckling behavior. Failure was assumed when either the maximum compression stress in the fibers was exceeded or when buckling took place.



### 3.4.6 Results

The delaminating layer in the models was able to open and buckle locally. However, as already indicated from the linear buckling analyses, global buckling took place in all models. Due to the external pressure it was found that a contact pressure was present between the delaminating layer and the substrate, causing both to act as one part without losing its load carrying capacity. For this reason, it was not required to refine the mesh size.

As no local buckling took place, the fiber stress around the delamination area was not significantly increased. Therefore, the maximum fiber compression stress for all models was found in layer 1, which is the most critical layer for external pressure (Appendix A). However, the global buckling behavior as shown in Figure 3.19 causes an additional increase in fiber compression stress in the inner layers of the major axis and in the outer layers of the minor axis.

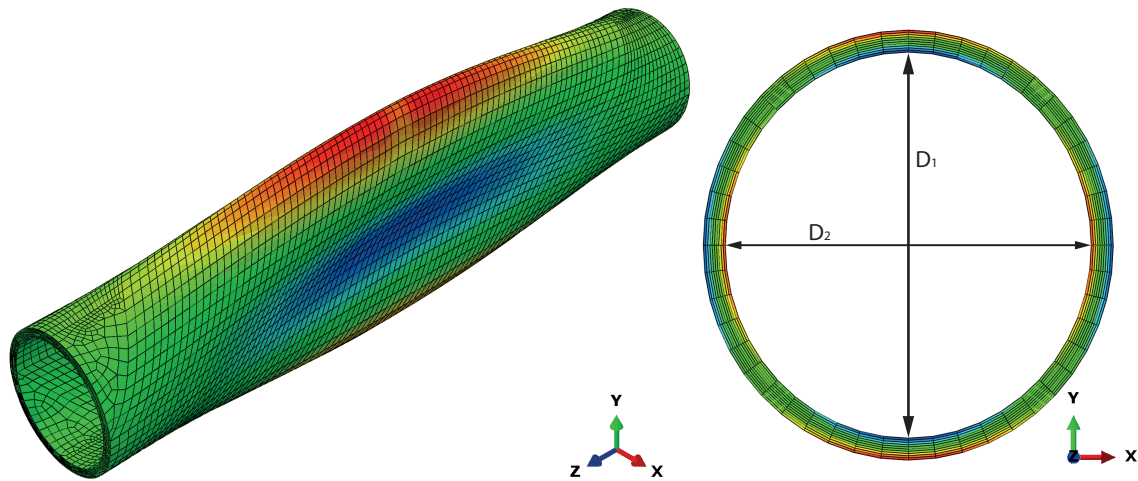


**Figure 3.19:** Visualization of stress state in the entire TCP (left) and cross-sectional (right) reinforcement for external pressure for a TCP with a delamination at  $\bar{h} = 0.5$ . The contour colors represent the compression stress value with red and blue being the low (or zero) and high values, respectively. For clarity of the buckling behavior the deformation scale factor is set to 25 for the reinforcement on the left.

In Figure 3.20 the fiber compression stress is plotted against the applied external pressure. A linear relationship between both is observed up to three quarters of the buckling pressure, after which the fiber stress started to increase more rapidly as the external pressure increases. As the fiber compression stress is related to the displacement of the TCP, the moment the graph becomes vertical, the critical limit point is reached and the structure buckles. The figure shows no distinctive differences in the curves between the models.

Results are listed in Table 3.8, comparing the external pressure at which buckling took place and the maximum fiber compression stress with the defect free model. It was found that global buckling took place for all models with practically no differences between the models. Minor differences were observed in the fiber stress, with a maximum increase of nearly 2.5 % for a delamination close to the inner surface. Despite these differences in fiber stress, the TCPs containing delaminations failed at the same external pressure compared to the defect free model, as the fiber compression stress was still 50 % below the allowable stress (indicated

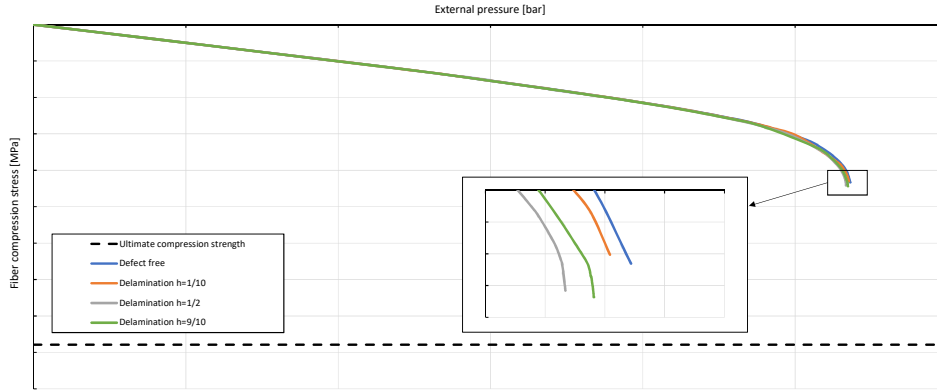


**Figure 3.20:** Fiber compression stress for a TCP subjected to external pressure.

with a dashed line in Figure 3.20). However, it is expected that some geometries will reach the maximum fiber stress first before buckling occurs [59].

**Table 3.8:** Differences in external pressure and fiber compression stress for a TCP containing a delamination at different thickness positions with respect to a defect free situation.

	Delamination $\bar{h} = 0.1$	Delamination $\bar{h} = 0.5$	Delamination $\bar{h} = 0.9$
Buckling pressure	-0.16 %	-0.51 %	-0.29 %
Maximum S33 increase	-0.64 %	1.96 %	2.44 %

### 3.5 TCP model including voids - lateral crushing

It has been shown that voids do not seriously affect the external pressure load capacity of TCPs, but what is the effect on the lateral crushing behavior, in which the through-thickness properties are of high importance? The failure mechanism in this load case strongly depends on the matrix properties and the three-dimensional stress-state in the laminate [64].

To study this topic, crushing TCP specimens were considered to evaluate the effect on the interlaminar strength. For this, a TCP with a different geometry compared with the previous analyses was considered, because a TCP including delaminations has been manufactured and tested in the past, which will be elaborated upon in Section 4.2. This was an 80-layer, 2.5 inch EGF-HDPE TCP with a  $\pm 55^\circ$  layup and a liner and coating thickness of 5 mm.

#### 3.5.1 TCP model

A TCP model was created similarly as explained in Section 3.1; a solid pipe length of 50 mm was extruded in which 20 circular sections were created, each representing four layers of reinforcement. This created model was without helical sections following the winding angle. Analytical rigids were used to represent two parallel crushing plates on top and bottom of the TCP, as shown in Figure 3.21. The use of analytical rigids decreases computational costs

compared with rigid surfaces formed by element faces. As during the experimental tests steel bearing plates were used, much stiffer compared with the TCP materials, this approach was suitable.

A number of 96 elements was used in the circumferential and 26 in the radial direction; one element per four layers and three elements for both the liner and coating.

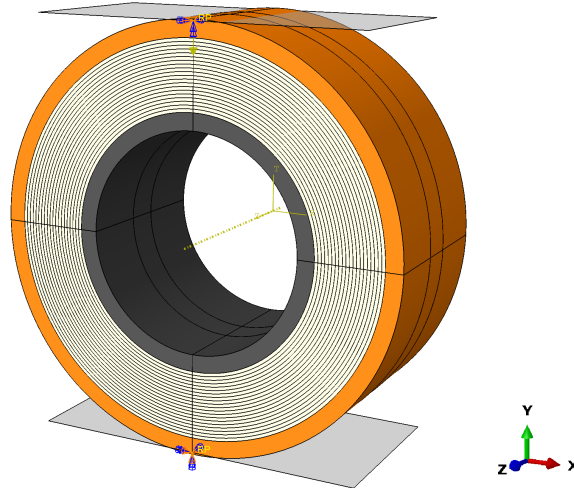


**Figure 3.21:** Lateral crushing model including load application. TCP characteristic colors are included for clarification.

### 3.5.2 Lateral crushing load case

A lateral crushing load was introduced as a concentrated force of 30 kN pressing down on the analytical rigid, as shown in Figure 3.21. Due to the analytical rigid this force was equally distributed over the length of the TCP. A contact condition between the plates and the TCP outer surface was established and displacements of the bottom plate were restricted, allowing the TCP to be crushed between both plates.

#### Modeling delaminations

In addition to a defect free reference model, models with delamination were created. Delaminations were modeled similar as discussed in Section 3.4.1. Three delamination widths were considered: 13, 25 and 42 mm. The middle of the delaminations were located at an angle of  $45^\circ$  counterclockwise of the loading direction and in the middle of the laminate thickness ( $\bar{h} = 0.5$ ), as shown in Figure 3.22.

Unlike an external pressure load case, the delaminating layer opens from the substrate when loaded. Therefore a complex stress state around the delamination edges arises, urging the need for a refined mesh size. Submodels were created for this, similar as discussed in Section 3.3.3. In the submodels, additional sections were created around the midplane of the laminate, such that the reinforcement layers close above and below the midplane consisted of one element thickness. In addition, a biased mesh in the circumferential direction was used, with smaller elements near the edge of the delaminated area. The submodel of the 13 mm delamination including its corresponding mesh is shown in Figure 3.22.

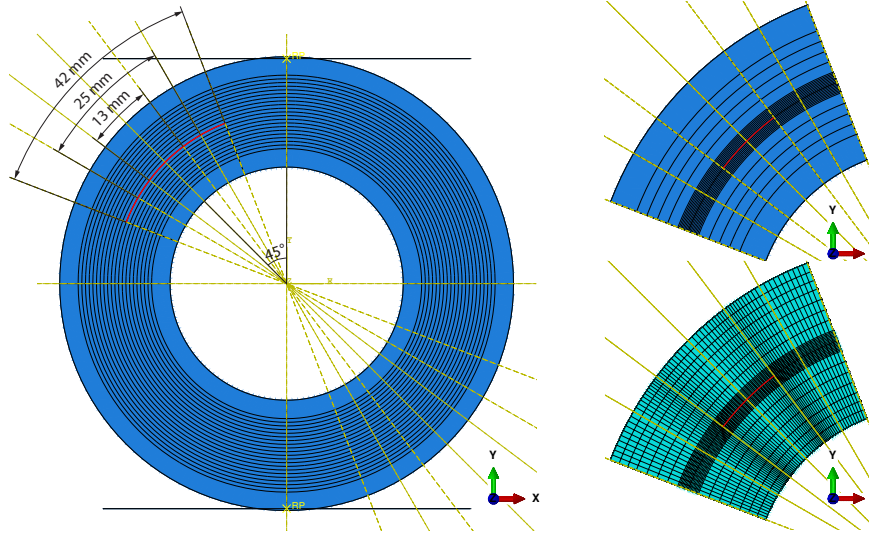


**Figure 3.22:** Location delaminations for lateral crushing models (left) and the submodel for the 13 mm delamination (top right) with its mesh (bottom right). The red lines indicate the location of the delamination.

### 3.5.3 Results

First failure was expected to be caused by exceeding the allowable matrix stress [64]. Due to the three-dimensional stress-state in a TCP when laterally crushed, an equivalent matrix stress covering all non-fiber dominated failure mechanisms was used. In the equivalent stress, the stress tensor is transformed into a single component, using a selected criterion. As an example, such transformation of the normal ( $\sigma$ ) and shear stresses ( $\tau$ ) is given in Equation (3.4) for the Von Mises criterion ( $\sigma'$ ), which is commonly used in engineering [65].

$$\sigma' = \sqrt{\frac{(\sigma_{11} - \sigma_{22})^2 + (\sigma_{22} - \sigma_{33})^2 + (\sigma_{33} - \sigma_{11})^2}{2} + 3(\tau_{12}^2 + \tau_{13}^2 + \tau_{23}^2)} \quad (3.4)$$

#### Defect free model

To predict the strength of the models, it should be known at what stress state failure occurs. For this value, the experimentally obtained mean failure load (Section 4.2.4) for the defect free TCP was used. The corresponding stress state is shown in Figure 3.23 and was obtained from the FE model by the evaluation at the experimental load. A symmetric stress state in the TCP is present, in which the maximum matrix equivalent stress is around the middle of the laminate on the top and bottom of the TCP on both sides of the crushing plates. At these areas delaminations are expected, which is also experimentally observed. Based on the experimentally obtained mean failure load, the corresponding maximum matrix equivalent stress was considered to be the stress at which the TCP fails.

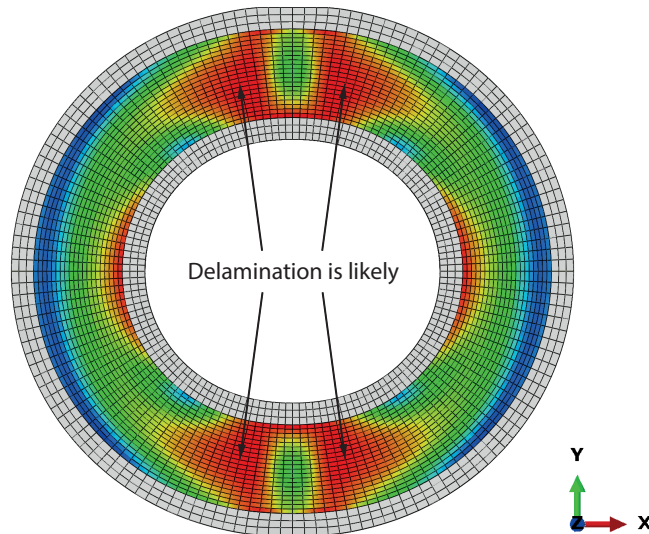


**Figure 3.23:** Visualization of the matrix equivalent stress state in the reinforcement of a defect free TCP subjected to lateral crushing. The contour colors represent the stress value with red and blue being the high and low (or zero) values, respectively.

### Models including delaminations

To predict the failure load for the models with a delamination, load was introduced until the matrix equivalent stress allowable was exceeded. A small element size was required for these models, as stress concentrations in the matrix equivalent stress arose at the delamination edge (crack tip), which is shown in Figure 3.24 for a 13 mm delamination. It was however observed that the stress peak increased as the elements size decreased. A minimum element size around the crack tip was chosen to be 0.25 mm, equal to the element thickness. With this approach, large decreases in failure load were predicted. The failure load predicted using this approach is the onset of damage load, i.e. the load at which the delamination grows. The FE results do not include progressive damage analysis, meaning results after the onset of delamination growth might not be realistic.

Table 3.9 shows the expected decreases, varying between 51 and 80 %. Remarkable is the largest decrease is not predicted for the largest delamination. The effect of different void geometries, thickness positions and the effect of multiple voids is however not studied, as the validation of model requires further investigation, which will be more elaborated upon in Chapter 5.

**Table 3.9:** Differences in lateral crushing failure predictions for a TCP containing a delamination with different widths with respect to a defect free situation.

	Delamination $\bar{h} = 0.5$		
	13 mm	25 mm	42 mm
Crushing load	-51 %	-80 %	-69 %

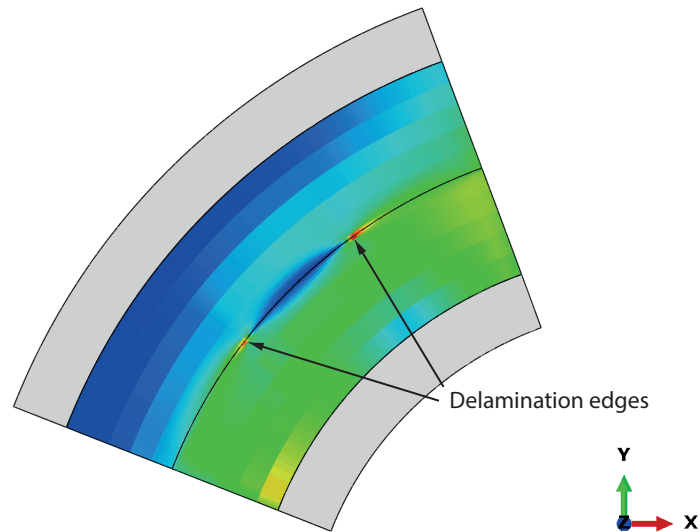


**Figure 3.24:** Visualization of the matrix equivalent stress state in the reinforcement of a TCP with a 13 mm delamination subjected to lateral crushing. The contour colors represent the stress value with red and blue being the high and low (or zero) values, respectively.

### 3.6 Conclusions

An FE TCP model was successfully developed to study the effects of gaps and voids in TCPs. By assigning matrix material to a section with a similar thickness as the composite layers, the gap behavior as occurring in TCPs was mimicked. It was found that the presence of a gap provokes an equal stress increment in all layers having the same winding angle as the gap layer. A slightly more pronounced increase in stress is present in the first layer below the gap layer having the same winding angle, concluding that the thickness position is only of importance if the gap layer is close to the critical layer. Therefore layer 3 in the considered TCP is the most critical in having a gap. The stress increase is linear proportional to the gap width and multiplies if gaps are exactly overlapping. The increase effect of multiple gaps rapidly diminishes when the longitudinal position between the gaps increases.

Voids are modeled as delaminations, in which the delaminating layer and substrate are allowed to open. It was found that the application of external pressure on TCPs having a delamination does not influence the failure pressure, regardless the thickness position. The tendency of the delaminating layer to be pressed onto the substrate is expected to be the cause. However, it is expected that delaminations do have a strong effect on the lateral crushing behavior of TCPs, in which the through-thickness properties are of high importance. For the latter load case, the delaminating layer opens, causing stress peaks at the delamination edges.

Prior to the discussed effects of defects in this chapter have any meaning, the modeling techniques need to be validated, which is the key topic of the following chapters.

# Testing of defects in TCPs

Experimental tests have been performed as part of the validation procedure of the FE modeling discussed in the previous chapter. For gaps, the manufacturing and testing of tensile coupons is described in Section 4.1. For voids, lateral crushing tests have been performed on TCP level and described in Section 4.2. For both cases a control group and a test group (or groups) have been tested to examine the differences between both. Conclusions are drawn in Section 4.3 and the results of this chapter are used in the Chapter 5 to compare to the FE results.

## 4.1 Gaps in specimens

This section provides the assessment of the test results for determining the fiber tensile properties of EGF-HDPE coupons. Two type of laminates have been manufactured for this: control (defect free) and test (gap containing) laminates. Tensile tests have been performed according to ASTM D3039 - Standard Test Method for Tensile Properties of Polymer Matrix Composite Materials [66].

### 4.1.1 Plate manufacturing

A schematic representation of the two types of plates is displayed in Figure 4.1. An effective usable area of 300 x 300 mm was used. For this, the total plate dimensions were 400 x 400 mm to obtain a uniform thickness in the usable area. The stacking sequence for the laminates was  $[(90/0)_2]_s$ , where the  $0^\circ$  layers correspond to the tensile loading direction. With an average thickness of 0.25 mm per ply, the resulting laminate had a nominal thickness of 2 mm. Thermocouples were placed between layer 4 and 5 in two diagonally opposite corners a few centimeters from the edge.

Four plates have been manufactured: two control and two test plates. While for the control plates the above mentioned stacking sequence was used, for the test plates a different approach



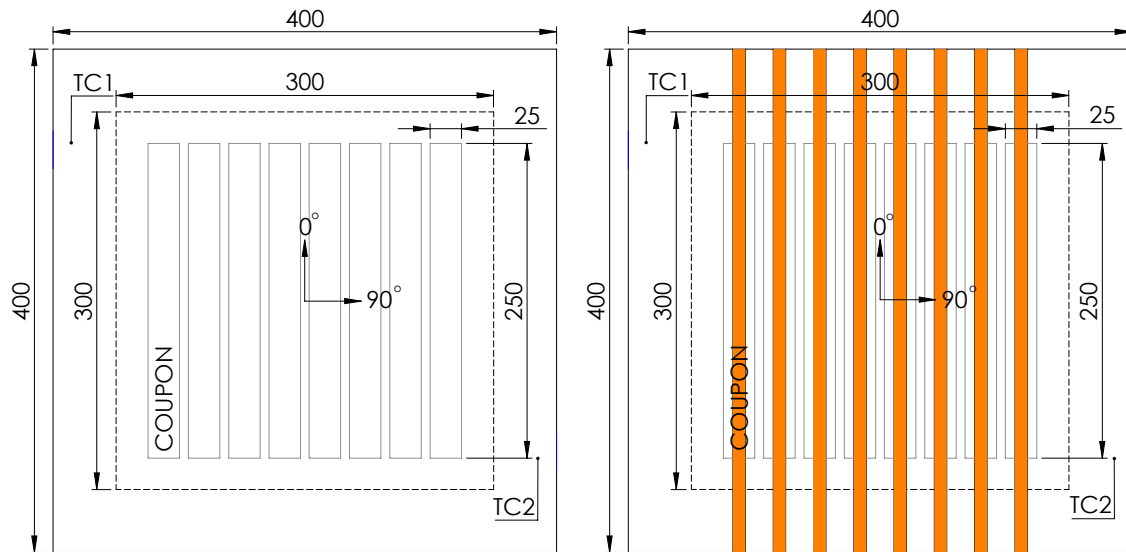


**Figure 4.1:** Schematic layout for the control (left) and test (right) plates including the location of the specimens. The orange color represent the gap areas and TC the location of the thermocouples. Dimensions in mm.

was used. In the  $0^\circ$  layers 4 and 5, EGF-HDPE strips were replaced with 10 mm HDPE strips, corresponding to the mid-sections of the specimens.

A hydraulic 100 tonnes flat hot plate Joos press [67] was used for the plate pressing. Metal plates were placed on top and bottom of the laminates to obtain a smooth surface. A standard, temperature controlled, consolidation cycle for PE was used. During this cycle, temperatures of the heating zones of the press, the thermocouples and the pressure force were monitored.

#### 4.1.2 Coupon extraction

Per plate eight 250 x 25 mm specimens were obtained (from the locations displayed in Figure 4.1) by means of a waterjet cutting machine. The gap specimens were cut in a way the 10 mm HDPE was aligned in the middle of the specimens, as shown in Figure 4.2.



**Figure 4.2:** Photo of a control (top) and a test (bottom) specimen.



### 4.1.3 Tensile test

Fifteen control and 15 test specimens were tested in short term static tension to obtain the static tensile relations. Tests were performed according to ASTM D3039 [66], with the setup as shown in Figure 4.3. Tests were performed on an Instron 3367 30 kN test bench with mechanical fixtures of 57 mm, leading to a gauge length of 136 mm. An axial extensometer was attached to the specimen by means of o-rings. This extensometer was used until 1 % of axial strain was reached. Tests have been performed at room temperature. The tests were performed with a constant cross-head speed of 2 mm/min and force, displacement and strain were logged at 10 Hz.



Figure 4.3: Tensile test setup.

### 4.1.4 Results

Failure criteria according to the ASTM test standard were used, in which final failure of the specimen should occur within the specimen gauge section. Tests were successfully performed with mostly valid failure modes and reproducible static mechanical properties. The majority of the specimens failed in the gauge section, presenting lateral breakage and delamination of the 90° fibers and longitudinal shear off of the 0° layers. However, the control group specimens showed more angled type failures compared with the test group. Multiple specimens in the test group failed at the grip, but with an acceptable failure mode. It is expected that the slight variation in the thickness through the width (due to the gap) of the specimens caused a stress concentration at the grip. One specimen showed an invalid failure mode and is therefore excluded from the test results. Test conditions were on average 24.0°C and 19.7% RH.

Table 4.1 shows the test result differences between the control group and test group for the modulus of elasticity ( $E$ ), maximum axial load ( $P_{max}$ ) and the ultimate tensile strength ( $\sigma_{max}$ ). The modulus of elasticity is determined with the strain response of the extensometer between 0.1 and 0.3 % axial strain.

**Table 4.1:** Summary experimental tensile test data. Differences of the test group with respect to the control group.

	$E$	$P_{max}$	$\sigma_{max}$
Coefficient of variation control group	3.2	4.8	4.2
Coefficient of variation test group	2.4	2.7	2.6
Difference mean values	-17.2 %	-22.5 %	-21.8 %

Low scatter in the test results was observed, which led to low coefficients of variations. The  $E$ -modulus for the control group was found to be 17.2 % smaller compared with the test group. In the decrease in maximum load and ultimate tensile strength similar values were found, with respective decreases of 22.5 and 21.8 %. The value of the ultimate tensile strength is of more importance compared with the maximum axial load, as this value is based on the specimen geometry. However, the value of the maximum axial load is displayed as this value is used for the FE validation process, which will be dealt with in Chapter 5.

## 4.2 Voids in TCPs

In 2015, experimental lateral crushing tests on TCP level with and without delaminations have been performed [68, 69]. These tests were carried out according to ASTM D2412 - Standard Test Method for Determination of External Loading Characteristics of Plastic Pipe by Parallel-Plate Loading [70]. However, the obtained results have never been thoroughly analyzed and worked out. Limited data from this has been preserved, which has been used in this study.

### 4.2.1 Pipe manufacturing

A 2.5 inch 80-layers EGF-HDPE TCP had been manufactured. Several meters of this pipe was used for research purposes. One of these purposes was to identify the crushing behavior in the presence of voids. For this, three different widths of delaminations were artificially created during the manufacturing of the pipe. This was done by placing heat resistant blue scotch tape over the length of the pipe in the middle of the laminate thickness ( $\bar{h} = 0.5$ ).

### 4.2.2 Test specimens

During the manufacturing of the pipe, reference coordinates were used to locate the defects, as the coating causes the defects to be no longer visible by the human eye. A total of 27 specimens were cut from the pipe, having a nominal length of 50 mm. A control series of 15 defect free specimens was used as reference. Three test series specimens with delamination

widths of 13, 25 and 42 mm were cut, with a smaller amount of specimens per test series. The delaminations were through-the-length of the specimens. An overview of the four different test batches is shown in Table 4.2.

**Table 4.2:** Lateral crushing test series.

Series	Defect type	Amount
Control	Defect free	15
Series 1	13 mm delamination	2
Series 2	25 mm delamination	5
Series 3	42 mm delamination	5

### 4.2.3 Lateral crushing test

A total of 27 tests have been performed to determine the crushing resistance of the pipe specimens with and without defects. The tests were performed according to ASTM D2412 [70], with the test setup as shown in Section 4.2.3. An Instron 3367 30 kN test bench was used, in which two steel, flat and parallel bearing plates were mounted. The TCP specimens were placed with the longitudinal axis parallel to the bearing plates and centered laterally in the testing machine. The test series specimens were placed in such a way that the middle of the delamination was at a  $45^\circ$  angle with the loading direction. After a 100 N preload was applied to remove the slack between the specimen and the plates, the upper bearing plate moved down on the specimen with a speed of 12.5 mm/min. The tests have been performed at room temperature and time, force and displacement were monitored and logged at 10 Hz.

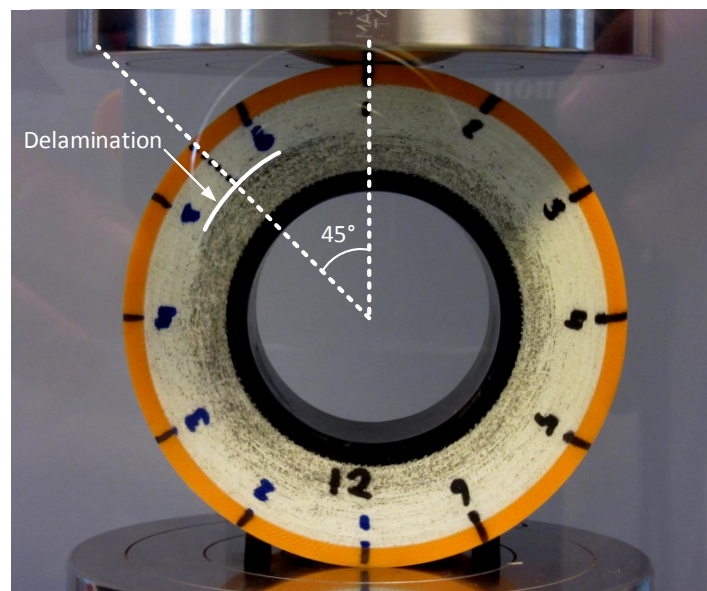


**Figure 4.4:** Lateral crushing test setup with a delamination at  $\bar{h} = 0.5$  with a  $45^\circ$  anticlockwise angle towards the direction of loading.

#### 4.2.4 Results

A summary of the test results is shown in Table 4.3. The parameter of main interest is the crushing resistance ( $P_{crush}$ ), defined by:

$$P_{crush} = \frac{P_{max}}{l}, \quad (4.1)$$

where  $P_{max}$  is the maximum load during the test and  $l$  is the specimen length.

Two points were of interest during the tests: 1) the first evidence of an event (i.e. delamination, cracking) and 2) a drop in load on the specimen. Load displacement curves for one specimen per test series is shown in Figure 4.5. For the control group, the load increased with an increasing displacement up a point where the load dropped for an increase in displacement, thus having a clear maximum point in the load displacement plot. This point indicates the onset of delamination formation in the defect free specimens. Test series 1 and 2, with their respective delaminations of 13 and 25 mm, showed however a difference in the load displacement curves. At a certain load, a small drop in load took place, after which the load increased again with an increasing displacement. Finally, a second drop in load took place, similarly to the drop observed in the control group. It was observed that at the first drop in load, the artificial delamination started to grow. Surprisingly, a first drop in load for test series 3, with a 42 mm delamination was not observed. However, for this series it was evident from video recordings that the delamination started to grow at a certain point, which was consistent for all individual tests. The parameters corresponding to the onset of delamination growth are in Table 4.3 denoted by subscript 1, whereas the parameters at the maximum load are denoted by subscript 2.

In addition, a change in stiffness for the test series was observed. The displacement at the maximum load for the test series was found to be 17 to 23 % larger compared with the control specimens. It should be noted that according to the ASTM manual,  $\Delta y$  is the measured change of the inside diameter in the direction of the load application. However, as this parameter was not measured during the tests, the machine displacement was used for this. It was therefore assumed that the wall thickness of the TCP did not change during the test. Furthermore, slack in the system also has an effect on the recorded machine displacement.

Considering the maximum values, all three delamination geometries did not have a major effect on the crushing resistance, with a maximum decrease of 2.3 %. Interestingly, the largest decrease was observed for the 13 mm delamination. However, it should be noted that a small amount of specimens were tested for this test series, affecting the confidence of the results. At the onset of delamination growth, the integrity of the TCP can no longer be guaranteed, despite the fact that a load carrying capacity was found to be present after the moment the delamination started to grow. Therefore the onset of delamination growth is of importance in the analysis of TCPs. Based on the onset of delamination growth, large decreases in mechanical performances were observed, from 11.3 % for the smallest delamination up to 46.3 % for the largest.

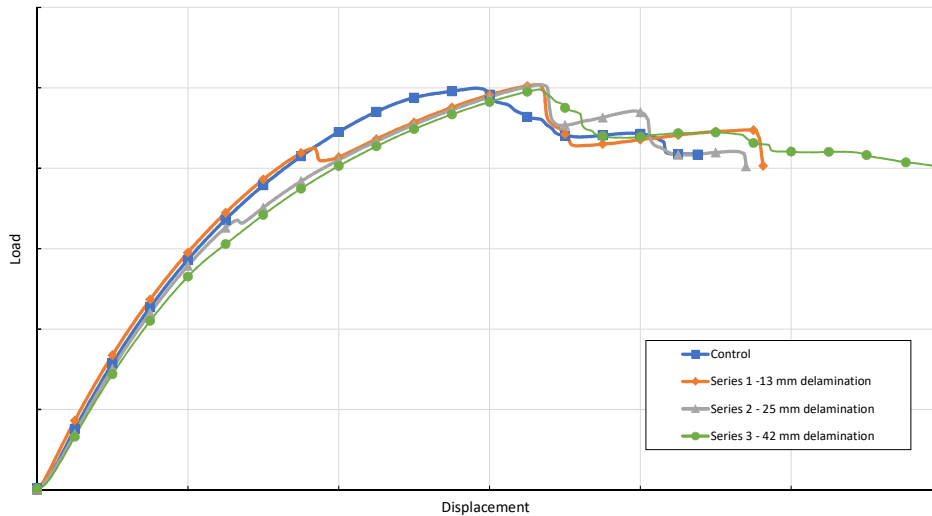


**Figure 4.5:** Load displacements curves for one specimen of the control group and one per test series.

**Table 4.3:** Summary experimental lateral crushing test data. Differences in mean values for the test series with respect to the control defect free group.

	Onset of delamination growth			Maximum		
	$\Delta y_1$	$P_{max_1}$	$P_{crush_1}$	$\Delta y_2$	$P_{max_2}$	$P_{crush_2}$
Series 1 - 13 mm	-29.5 %	-11.0 %	-11.3 %	17.8 %	2.6 %	2.3 %
Series 2 - 25 mm	-47.7 %	-29.4 %	-29.5 %	17.5 %	1.7 %	1.5 %
Series 3 - 42 mm	-61.5 % <sup>1</sup>	-46.3 %	-46.3 %	22.8 %	1.7 %	1.7 %

<sup>1</sup> Approximated value

## 4.3 Conclusions

Tensile specimens with and without gaps have been successfully manufactured and tested to study the mechanical properties between both. A  $[(90/0)_2]_s$  layup was used, in which for the specimens with gaps, a section of EGF-HDPE was replaced by HDPE. Reductions in mechanical properties varied from roughly 17 to 22 %.

In the experimental phase of the assessment of voids, lateral crushing specimens were cut from a TCP manufactured with artificial delaminations. Three types of delaminations were tested, showing an onset of delamination growth at a significant lower crushing load compared with reference specimens, up to 46 %. However, no significant decreases were observed for the maximum failure loads, indicating a delamination does not affect the ultimate load carrying capacity. Additionally, the delaminations caused a decrease in TCP stiffness.

The experimental obtained values are used in the next chapter, in which they are compared to the FE results.



# Validation of defect modeling in TCPs

This chapter is dedicated to the validation of the defect modeling used in Chapter 3. The experimental results discussed in Chapter 4 were used for this purpose. The validation of gaps and voids are discussed in Section 5.1 and Section 5.2, respectively. Conclusions whether the modeling techniques are validated or not are drawn Section 5.3.

## 5.1 Validation gap modeling

As presented in Section 3.2, a gap was modeled as a section where the material properties were set to HDPE material. To validate this modeling technique, tensile coupon behavior was simulated (Section 3.2.2) and compared to the experimental results (Section 4.1.4). The results in terms of  $E$ -modulus and the maximum failure force are summarized in Table 5.1. For the  $E$ -modulus, a decrease of 17.2% and 18.2% was obtained from the experimental and modeling results, respectively. The FE modeling predicted a slightly larger decrease in stiffness. For the failure load, the experimental obtained decrease was slightly larger compared to the FE model, with respective 22.5% and 21.1%. Despite the minor differences between the results, a good agreement between FE the models and experiments was obtained. With this it is demonstrated that the gap modeling technique represents the actual behavior and therefore the effect of gaps on TCP level (Section 3.3.5) are assumed to be valid.

**Table 5.1:** Comparison FE modeling and experimentally obtained decreases in  $E$ -moduli and failure loads for tensile specimens containing gaps with respect to defect free specimens.

	$E$		$P_{max}$	
	FEM	Experimental	FEM	Experimental
Difference	-18.2 %	-17.2 %	-21.1 %	-22.5 %

## 5.2 Validation void modeling

Void modeling (Section 3.4.1) was based on modeling two separate parts instead of one, in which the defect free areas were tied and a contact condition was used in the delamination. Lateral crushing specimens have been virtually and experimentally tested and the decreases in mechanical performance are listed in Table 5.2.

There is a lack of agreement between the FE modeling and experimental results. The predicted performance decrease obtained using FE modeling is highly overestimated. The reason for this mismatch is the localized stress concentrations at the delamination edges, which are highly dependent on the element size used.

**Table 5.2:** Comparison FE modeling and experimentally obtained decreases in the crushing load at the onset of delamination growth for lateral crushing specimens with respect to defect free specimens.

	13 mm delamination		25 mm delamination		42 mm delamination	
	FEM	Experimental	FEM	Experimental	FEM	Experimental
Difference	-51.0 %	-11.0 %	-80.4 %	-29.4 %	-69.4 %	-46.3 %

As no agreement was found considering the matrix equivalent stress, the out-of-plane shear stresses  $S_{12}$  and  $S_{13}$  were investigated, as well as their combination in the so-called delamination stress. The latter is defined by [11]:

$$\sigma_{delamination} = \sqrt{\sigma_{12}^2 + \sigma_{13}^2}. \quad (5.1)$$

It was found that the stress peaks for all parameters were at the same location as the matrix equivalent stress, but no correlation was found between one of the parameters and the experimental results.

Test series 1 and 2, with their respective delaminations of 13 and 25 mm, showed a clear onset of delamination growth, which was also observed in their load displacement curves. At this point the delamination opened and started to grow. In the FE models, the contact pressure and status between the delaminating layer and substrate were obtained. However, for an increasing load, the contact between both gradually decreased as the delaminating layer started to detach from the substrate. Therefore, the onset of delamination cannot be predicted based on the contact between the delaminating layer and the substrate.

In Figure 5.1 the load displacement curves for the defect free TCP and test series 3 - 42 mm delamination are shown. The experimentally obtained results are averaged and superimposed with the FE results. There is a good agreement between both. However, for the 42 mm delamination the experimental curve slightly deviates from the FE curve as the displacement increases. This mismatch can be explained by the delamination growth observed during the test. The larger the delamination becomes, the less stiff the TCP is. While in the experimental tests delamination growth is allowed, in the FE analyses it is not. Although the 42 mm delamination causes the TCP to be less stiff, the effect is not very pronounced. The reduced stiffness response is made clear for an exaggerated delamination spanning half the TCP circumference (Figure 5.2).



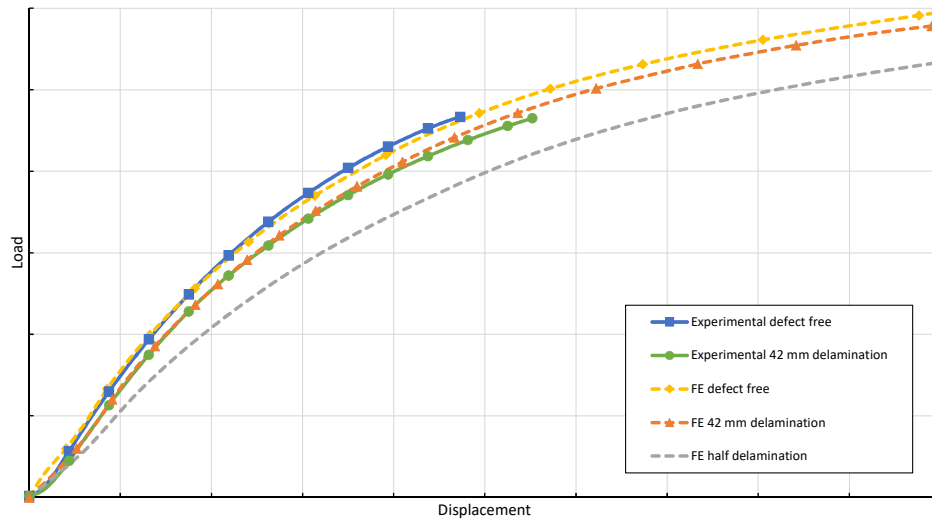


**Figure 5.1:** Comparison load displacement curves of experimental and virtual tested lateral crushing specimens.

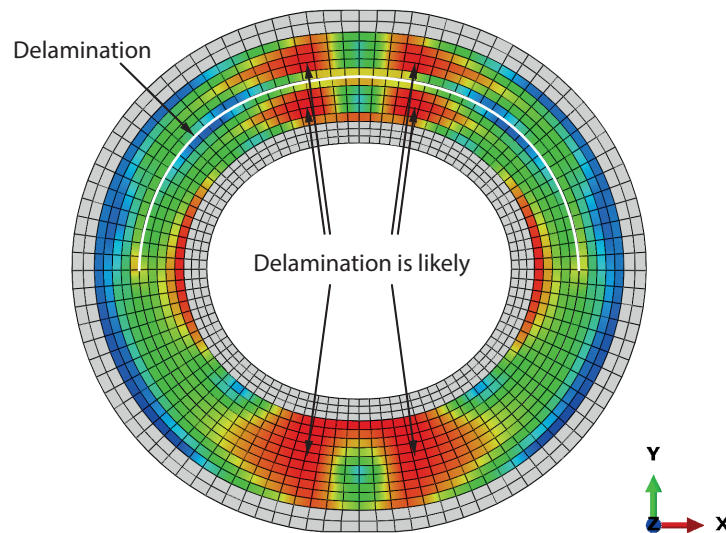


**Figure 5.2:** Visualization of the matrix equivalent stress state in the reinforcement of a TCP with a delamination  $\alpha = \pi$  at  $\bar{h} = 0.5$  subjected to lateral crushing. The contour colors represent the stress value with red and blue being the high and low (or zero) values, respectively.

Moreover, from Figure 5.2 it is observed that the delamination causes in the upper part of the TCP a stress response similar to two individual TCPs, both having half the original laminate thickness. The observations of the two distinctive points in the experimental tests, one being the onset of delamination and the other being the ultimate strength, can be explained with this. At the onset of delamination, the stress exceeds the allowable locally, causing the delamination to grow. However, the TCP remains its load carrying capacity, as the final failure is determined by a global stress state exceeding the allowable, which is followed by one or multiple delaminations. The load carrying capacity after the onset of delamination growth is important for the integrity management, but outside the scope of the present study. For

this, damage progression and fracture mechanics need to be studied.

As for external pressure, in which the failure is either determined by buckling or fiber compression failure, the through-thickness properties are of less concern. In contrast to the modeling of a lateral crushing load case with delaminations, modeling of an external pressure load case with delaminations is widely present in literature and therefore it is plausible the modeling technique is valid to study the effect of a delamination on TCP level. However, even with a validated method for the modeling of delaminations in an external pressure load case, still a larger decrease is expected considering lateral crushing. It is therefore recommended to focus on the latter in future studies.

### 5.3 Conclusions

In the validation procedure of gaps, in which the material properties were reduced locally, tensile coupons tests have been virtually and experimentally tested. The decrease in  $E$ -modulus and failure load between defect free specimens and specimens having a gap were compared. A good agreement between both was observed and thus it is demonstrated that the modeling technique of gaps is validated. This concludes that the assessment results of gaps on TCPs in Section 3.3.5 can be considered correct.

The used modeling technique for voids, in which a contact condition between the surfaces of the delaminating layer and substrate is established, allowing the delamination to open, is not validated. An absence of agreement between the virtual and experimental testing was observed, originating from the fact an artificial delamination act as a crack, causing localized stress concentrations at the edges. The delamination grows as local stress peaks at the delamination edges exceed the allowable, while the maximum load carrying capacity of the system is determined by the global stress field in the TCP. Although the stiffness response can be predicted, a correct failure indicator is missing. The delamination failure (onset of delamination growth) cannot be predicted based on the stress state obtained at the onset of delamination formation in a defect free specimen.

# Tool to assess the effects of defects in TCPs

The modeling method for gaps in TCPs is validated and therefore the effect of gaps discussed in Section 3.3.5 is assumed correct. However, the involved modeling work to obtain the effect of gaps for a certain TCP geometry is very labor-intensive, and therefore costly to repeat when a new TCP is to be developed. Currently, a tool to assess the effect of gaps, as described in Section 2.2.1, is present. In Section 6.1 is this tool compared with the modeling results obtained in this study. It was found the accuracy of the current tool can be substantially improved and therefore a new tool is proposed for the assessment of gaps in Section 6.4. The usage of the proposed gap tool is discussed in Section 6.4 and conclusions are drawn in Section 6.5.

### 6.1 Current gap assessment tool

As presented in Section 2.2.1, the effect of gaps is currently predicted using a statistical and straight forward approach based on area reduction. The current gap tool is however not validated by full scale testing, which is time consuming and expensive. Predictive engineering offers a solution here, and therefore the current gap tool was compared with the modeling results presented in this study.

#### 6.1.1 Current gap assessment tool used for tensile coupons

Using the methodology of the current gap tool, the strength reduction of the tested tensile coupons was predicted. Using Equation (2.1) with a gap width ( $W_g$ ) of 10 mm and a tape width ( $W_t$ ) of 15 mm, to obtain the specimen width of 25 mm, a layer strength reduction of 40 % is predicted. Having two overlapping gaps ( $r$ ) and four layers in the  $0^\circ$  direction ( $n$ ), the total strength reduction predicted by the current gap tool is 20 % with Equation (2.4). Similar performance reductions have been predicted and observed in the FE modeling and

experimental testing, as listed in Table 6.1. With this, it seemed that the gap calculator is an easy method to obtain a fairly accurate prediction of the strength decrease.

**Table 6.1:** Comparison of the strength decrease obtained by FE modeling, experimental testing and using the current gap tool, for tensile specimens containing gaps with respect to defect free specimens.

	FEM	Experimental	Current gap tool
Difference	-21.1 %	-22.5 %	-20.0 %

### 6.1.2 Current gap assessment tool used for TCPs

On coupon level there is a good agreement between the current gap tool and reality. However, on TCP level there is a lack of agreement between the strength reduction predicted using the current gap tool and using FE modeling. Figure 6.1 shows the effect of gap width and thickness position as discussed in Section 3.3.5, and includes the strength reduction predicted using the current gap tool. For the prediction with the current gap tool, similar gap widths were used and a tape width ( $W_t$ ) of 328 mm was assumed, covering the TCP in one winding. Both the predicted decreases including and excluding a safety factor of 3 are shown, in which the latter is comparable to gap widths ranging from 6 to 90 mm.

First, the curves of the current gap tool do not agree with the curves of the FE modeling, as significant differences in the slopes are present. The predictions are underestimated; up to a factor 3 for a gap in layer 3 when a safety factor of 3 is included and a factor 9 in the case the safety factor is disregarded. Second, the effect of thickness position is not represented in the current gap tool. In the current gap tool, the strength reduction is multiplied with the amount of overlapping gaps, which is similar to the effect of overlapping gaps considered in this study.

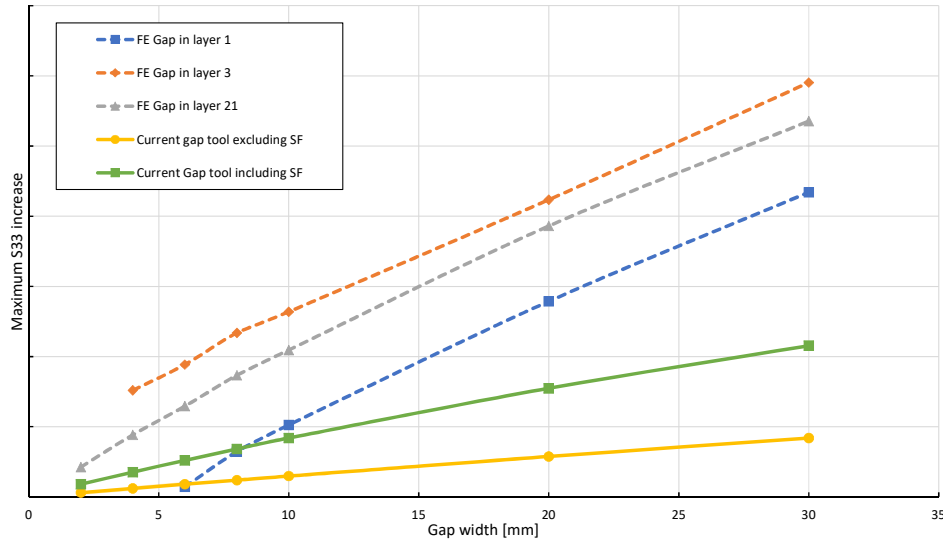


**Figure 6.1:** Comparison of FE modeling results with the current gap tool for the increase in the maximum fiber tension stress for different gap widths and thickness positions.

But why does the current gap tool accurately predict the strength decrease for the tensile coupons, while the prediction on TCP level falls short? The layer strength reduction (Equation (2.1)) depends on the gap width and tape width. For the tensile specimen, the tensile force is equally distributed over the cross-sectional area, having a finite width. In the case the specimen has a gap, the fiber stress in the specimen in the area of a gap is evenly redistributed over the cross-section of the defect free area, and therefore the relation between the gap width and the strength reduction is straight forward. However, as discussed in Section 3.3.5, a gap in TCPs does not evenly redistribute the stress over the remaining reinforcement. The stress increases in the TCP laminate is primarily on top and below the gap, while at a certain longitudinal distance from the gap no net effect of the gap is present. The current gap tool is based on the assumption that the stress is evenly redistributed over the width of the tape, which is found to be invalid on TCP level. The tape width has an effect on the amount of gaps (the probability of a gap increases as the tape width decreases), but not on the effect of a gap. It should be noted that in this example a tape width is used such that the TCP is covered in one winding. Differences in tape width give different results for the predictions of the current tool.

## 6.2 Proposed gap assessment tool

The accuracy of the current tool can be substantially improved and therefore a new gap assessment tool is proposed. The idea behind the tool is that a gap with a certain width and location can be included in an existing FE TCP model to assess the mechanical performance. The use of this tool for existing models increases the feasibility of performing the analyses during the design phase of a TCP. The amount of computational costs also play a role in this.

The tool is based on a Python script which can be executed in Abaqus, as Python is the application programming interface of this software. The methodology of the script is to set the material of the elements located in the gap to matrix material, without the use of helical sections. In this way a simple mesh can be used, greatly reducing the involved manual work. In this section the structure of the Python script is explained and the individual elements are highlighted to clarify the methodology. The final script can be found in Appendix B.

### Input

Prior to use the script, a full TCP model should be in place and meshed. Several inputs are required from the user. In the Abaqus/CAE, the name of the model, part and composite layup of interest need to be given. In addition, the reinforcement layer in which a gap is to be modeled, and the gap width are used as inputs.

Optionally, the total amount of reinforcement layers and the amount of layers per element thickness can be given. The script extracts the winding angle of the considered layer from the model and calculates the corresponding element section (denoted by  $R[number]$ ). The current limitation is that this is only possible if an equal amount of layers is used in all elements representing the reinforcement. If a different model structure is used, e.g. differences in the amount of layers per element, the winding angle and the element set of the layer containing the gap need to be given manually.

### Element centroid calculation

The first step in the process is the calculation of the centroid coordinates of the elements. For each element in the set (which is one of the circular sections as described in Section 3.1.3) in which the gap will be modeled ( $R[number]$ ), the coordinates of the nodes are extracted. It is important exclusively hexahedral elements, which is the default element shape in Abaqus, are used. The centroid of an element is calculated by summing the  $x$ ,  $y$  and  $z$  coordinates of the nodes in each direction, divided by the amount of nodes, as in:

$$\begin{bmatrix} x_c \\ y_c \\ z_c \end{bmatrix} = \frac{1}{n} \sum_{i=1}^n \begin{bmatrix} x_i \\ y_i \\ z_i \end{bmatrix}, \quad (6.1)$$

where  $x$ ,  $y$  and  $z$  are the coordinates of the centroid (denoted by subscript  $c$ ) and the nodes (denoted by subscript  $i$ ) and  $n$  is the amount of nodes per element.

### Transformation coordinate system

Next, the element centroid coordinates are transformed from the Cartesian coordinate system ( $x, y, z$ ) to a cylindrical coordinate system ( $r, \theta, z$ ) (Figure 6.2) using:

$$\begin{aligned} r &= \sqrt{x^2 + y^2}, \\ \theta &= \tan^{-1}\left(\frac{y}{x}\right), \\ z &= z. \end{aligned} \quad (6.2)$$

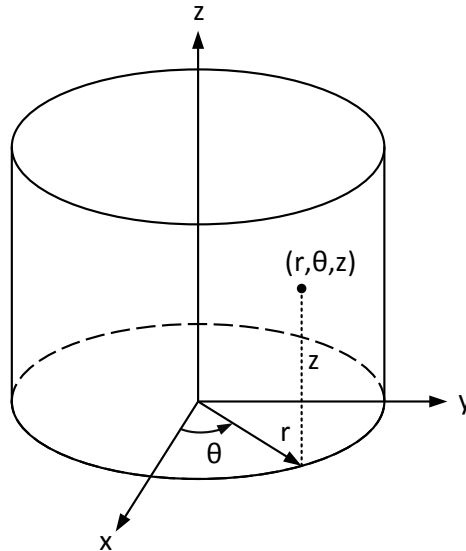


**Figure 6.2:** Cylindrical coordinate system.

The coordinate system transformation eases the calculation from a point in space to a helix, which represents the gap. The parametrisation of a helix, a curve in 3-dimensional space,

is defined by Equation (6.3) in the Cartesian coordinate system and by Equation (6.4) in a cylindrical coordinate system, where the radius is denoted by  $a$  and the pitch with  $b$ .

$$(x(t), y(t), z(t)) = (a \cos(2\pi t), a \sin(2\pi t), bt) \quad (6.3)$$

$$(r(t), \theta(t), z(t)) = (a, 2\pi t, bt) \quad (6.4)$$

The cylindrical coordinates are transformed to a 2-dimensional representation, having an  $x$ -axis and  $y$ -axis according to:

$$\begin{aligned} x &= z, \\ y &= r\theta. \end{aligned} \quad (6.5)$$

With this, a 2-dimensional representation of the TCP is produced, as shown in Figure 6.3. This representation is comparable to cutting a cylinder in the longitudinal direction and fold it open to a flat sheet. The helix becomes a straight line for each winding representing one circumference of the cylinder with:

$$r\theta = \tan(\phi) z, \quad (6.6)$$

which is in the form of a standard line equation:

$$ax + by + c = 0. \quad (6.7)$$

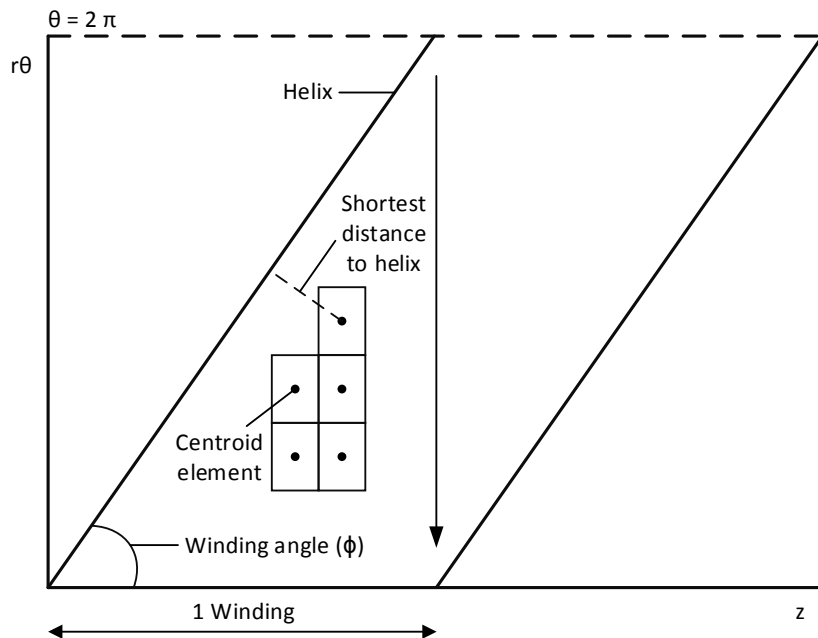


**Figure 6.3:** 2-Dimensional representation of a TCP including elements and a helix in the winding direction.

### Distance to line calculation

For each element, the shortest distance  $d$  from the centroid point  $(x_c, y_c)$  to the helix is calculated with [71]:

$$d = \frac{|a(x_c) + b(y_c) + c|}{\sqrt{a^2 + b^2}}, \quad (6.8)$$

where  $a$  is  $\tan(\phi)$ ,  $b$  is 1,  $c$  is 0,  $x_c$  is  $z$  and  $y_c$  is  $r\theta$  for the first winding. The constant  $c$  varies with the winding number.

If the shortest distance of the element centroid to the helix is smaller than or equal to half the gap width (as the centroid can be on both sides of the line) the element is (partially) located in the gap and stored in a list.

### New set definition

From the initial set ( $R[number]$ ), containing the elements in the defect free case, the elements which are calculated to be in the gap area are removed. A new set, containing the elements that are located in the gap, is created. The updated initial set and the new set are the outputs of the script and automatically implemented in the Abaqus model. On the left in Figure 6.4, the new set containing the gap elements is highlighted for a 10 mm gap in layer 21.

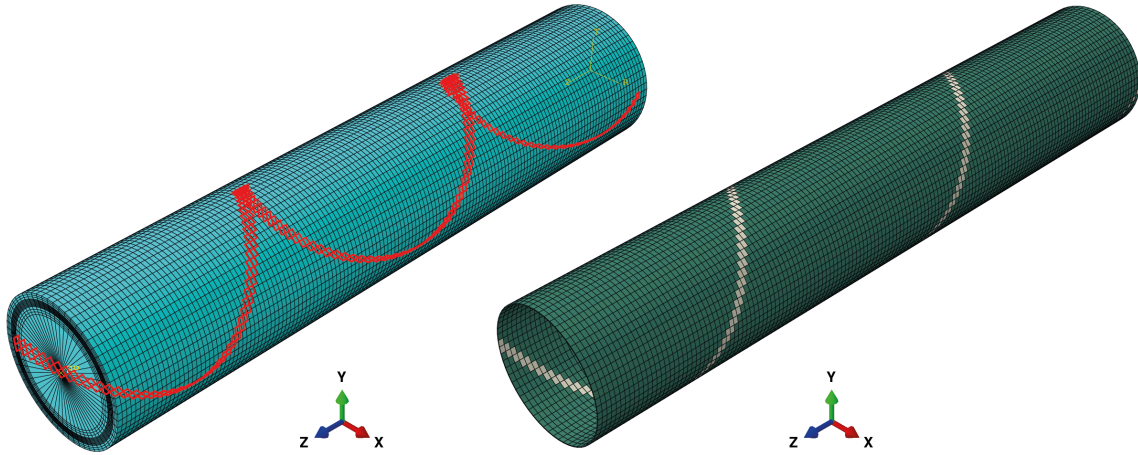


**Figure 6.4:** TCP with a 10 mm gap in layer 21 with the gap set highlighted (left) and the defined composites layouts for R6 (right), in which green represents the defect free layout and beige the layout for the gap set.

### Abaqus model adjustments

After executing the script, some actions are required in the Abaqus model. For the original set ( $R[number]$ ) adjustments are automatically done, requiring no further action. However, an additional layout, equal to the amount of plies in the gap elements, must be created. The layout for these plies must be equal to the adjusted element set ( $R[number]$ ). For the material selection of these plies, matrix material must be selected for the ply containing the gap, while



composite material (as used in the rest of the model) must be selected for the others, as shown in Figure 6.5. The result is shown in Figure 6.4 on the right, having two composite layups instead of one.

The procedure above can be repeated when the effect of, for example, multiple gaps is to be assessed.

		Ply Name	Region	Material	Element Relative Thickness	CSYS	Rotation Angle	Integration Points
1	✓	L21	Gap_10mm	HDPE	0.25	<Layup>	55.06	1
2	✓	L22	Gap_10mm	EGF-HDPE	0.25	<Layup>	-55.13	1
3	✓	L23	Gap_10mm	EGF-HDPE	0.25	<Layup>	55.21	1
4	✓	L24	Gap_10mm	EGF-HDPE	0.25	<Layup>	-55.28	1

Figure 6.5: Abaqus composite layup definition for the gap set for a gap in layer 21.

## 6.3 Proposed gap assessment tool analysis and validation

The proposed gap tool was tested and a sensitivity study has been performed. An internal pressure load case was considered, similar as in Section 3.3. With this, the TCP strength reduction predicted with the proposed gap tool was compared to the results obtained using the submodeling technique. As the aim of the tool is to assess the effect of gaps in a computational inexpensive way, three different methods, with their details presented in Table 6.2, have been analyzed and compared. The methods are discussed in the following sections.

### 6.3.1 Normal mesh method

The aim is to keep the element size as large as possible to reduce the computational costs. However, considering for example mesh 1 for the proposed gap tool, with a gap width of 10 mm in layer 21, either one or two elements are located in the longitudinal direction in the gap. The drawback of this method is that at the locations where two elements are present in the longitudinal direction, the fibers experience a larger stress compared with the areas in which the gap has a single element. This results in an uneven stress response in the laminate from which it is impossible to obtain the correct fiber stress, as shown in Figure 6.6 on the left.

This effect can be reduced if a smooth gap set is used, as shown in Figure 6.6 on the right. If the diagonal of the elements equals the winding angle of the TCP, then the selected gap elements follow a structured helix. This is obtained using Figure 6.7. If the element aspect ratio ( $AR$ ) is defined by the element longitudinal length ( $l_{lon}$ ) and the circumferential length ( $l_{cir}$ ) with:

$$AR = \frac{l_{lon}}{l_{cir}}, \quad (6.9)$$

**Table 6.2:** Proposed gap tool sensitivity study for different methods.

		Radial elements	Circumferential elements	Avg. longitudinal element size [mm]	Avg. element area [mm <sup>2</sup> ]	Aspect ratio	Total CPU time [h]
Defect free		16	48	10	119	0.84	2.2
Normal mesh	Mesh 1	16	48	10	119	0.84	2.3
	Mesh 1AR <sup>1</sup>	16	48	8.34	99	0.7	2.9
	Mesh 2	16	60	6.67	64	0.7	5.0
	Mesh 3	16	72	5.56	44	0.7	7.8
	Mesh 4	16	84	4.76	32	0.7	11.8
	Mesh 5	16	96	4.17	25	0.7	16.5
Defect layer	Mesh 1AR <sup>1</sup>	16	48	8.34	99	0.7	2.8
	Mesh 2	16	60	6.67	64	0.7	5.1
	Mesh 3	16	72	5.56	44	0.7	7.5
	Mesh 4	16	84	4.76	32	0.7	15.2
	Mesh 5	16	96	4.17	25	0.7	19.3
Biased mesh		16	96	1.48 <sup>2</sup>	9 <sup>3</sup>	-	13.4

<sup>1</sup> Longitudinal element size of mesh 1 is reduced to obtain an aspect ratio of 0.7.

<sup>2</sup> Smallest longitudinal element [mm].

<sup>3</sup> Smallest element area [mm<sup>2</sup>].

and:

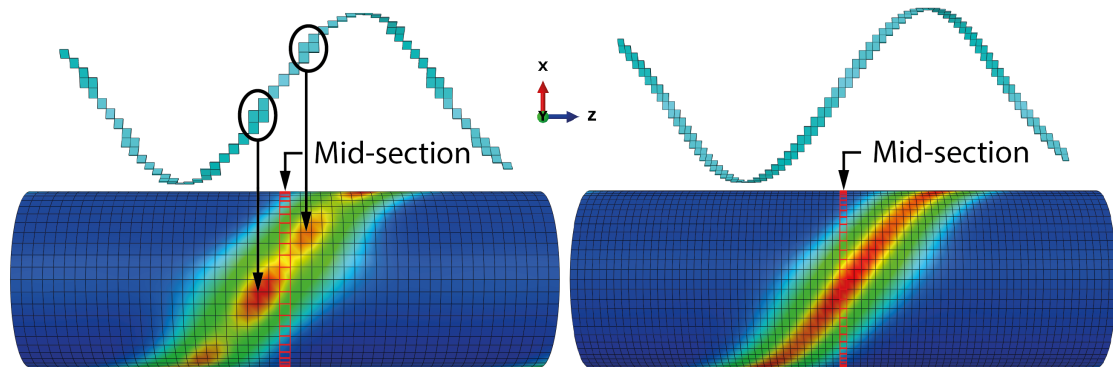
$$\tan(\phi) = \frac{l_{cir}}{l_{lon}}, \quad (6.10)$$

then the aspect ratio for which the element diagonal is parallel to the winding angle is:

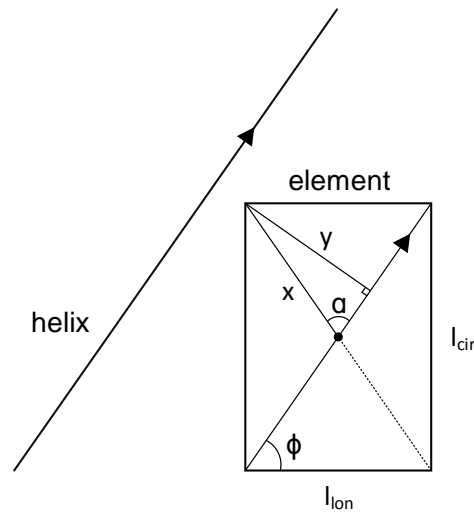
$$AR = \frac{1}{\tan(\phi)}. \quad (6.11)$$

For a winding angle of 55° an element aspect ratio of 0.7 is required to obtain a smooth gap set.

However, this is a rather rough method, as the aim is to maximize the element size without sacrificing the accuracy. If the element centroid location is just within the gap area, the whole element is considered to be a gap. On the other side, if the location of the centroid is just outside the gap area, the element as a whole is considered to be defect free, while half of the area is within the gap area. This will underestimate the effect of a gap and is shown in



**Figure 6.6:** Visualization of the fiber tensile stress in layer 1 for a 10 mm gap in layer 21 for the gap tool using an arbitrary mesh size (left) and a mesh size with an aspect ratio of 0.7 (right). The contour colors represent the stress value with red and blue being the high and low (or zero) values, respectively.



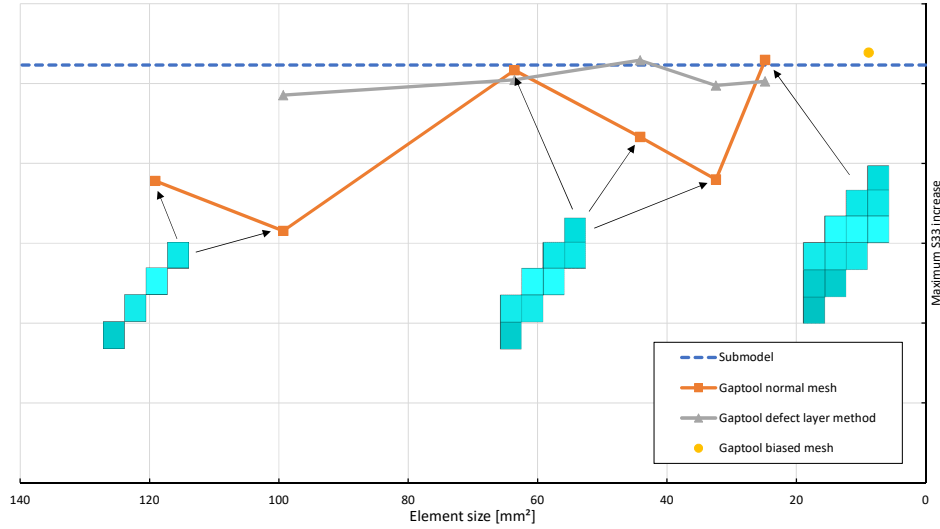
**Figure 6.7:** 2-Dimensional representation of an element to calculate the distance from a node to the diagonal.

Figure 6.8. Considering mesh 2, 3 and 4, they all having two elements in the longitudinal direction of the gap area, while the element size decreases with increasing mesh number. At a certain smaller mesh size (mesh 5), an additional element is added to the gap set. The result is a saw-tooth behavior in the accuracy.

### 6.3.2 Defect layer method

A second method is based on the defect layer method proposed by Fayazbakhsh et al. [19], in which per element the percentage of gap is calculated and the material is adjusted accordingly. For this, the proposed tool described in the previous section is extended to include this method. The longitudinal element length is required as additional input. It is essential that the aspect ratio of the elements equals the winding angle, as discussed before.

The percentage of element in a gap is calculated using Figure 6.7. If the aspect ratio ( $AR$ )



**Figure 6.8:** Mesh sensitivity study of the increase in the maximum fiber tension stress for a 10 mm gap in layer 21 for three different methods.

and longitudinal element length ( $l_{lon}$ ) are known, then the circumferential length is defined by:

$$l_{cir} = \frac{l_{lon}}{AR}. \quad (6.12)$$

The distance from one node to the element centroid ( $x$ ) is calculated using the Pythagorean Theorem:

$$x = \frac{1}{2} \sqrt{l_{lon}^2 + l_{cir}^2}. \quad (6.13)$$

With the known winding angle ( $\phi$ ), the angle  $\alpha$  can be obtained using basic triangle rules ( $\alpha = 180 - 2\phi$ ) and the distance from the node perpendicular to the element diagonal  $y$  is calculated with:

$$y = \sin(\alpha) * x \quad (6.14)$$

Now, if the desired gap width is divided by 2, as the gap is on both sides of the helix, the elements whose diagonal is at this distance are for 50 % located in the gap. If the element diagonal is within half the gap width minus the distance of a node perpendicular to the diagonal ( $y$ ), the element is for 100 % in the gap. With the fact that the element area is linearly proportional with the distance  $y$ , the gap percentage of each element can be calculated.

Ultimately, percentages ranging from 0 to 100 % defect would give the best accuracy. This introduces however a significant amount of work, as for every defect percentage a material has to be created within Abaqus. On the other hand, too little percentage steps cause large stiffness differences between elements, resulting in stress concentrations similar as observed in

the normal mesh method when no specific aspect ratio is taken into account. In the proposed tool, percentage steps of 10 are used. In addition, if the element diagonal is in between two percentage steps, the higher percentage of gap is assigned to the elements, yielding a conservative approach.

The result of this method are 10 new sets instead of a single one compared with the previous method. For the assignment of the material, a meanfield homogenization is used (Section 3.1.4), in which the fiber volume fraction can be reduced per set, corresponding to the gap percentage.

Five different mesh sizes have been analyzed for this method, with element sizes equal to the normal mesh method. Using this method, there are more elements in the longitudinal direction of the gap compared to the normal mesh method, as shown in Figure 6.9 on the left. A good agreement with the submodeling results is observed in Figure 6.8. In comparison with the normal mesh method, the saw-tooth behavior disappeared and this method is therefore less prone for the effect of the element size, yielding more robustness.

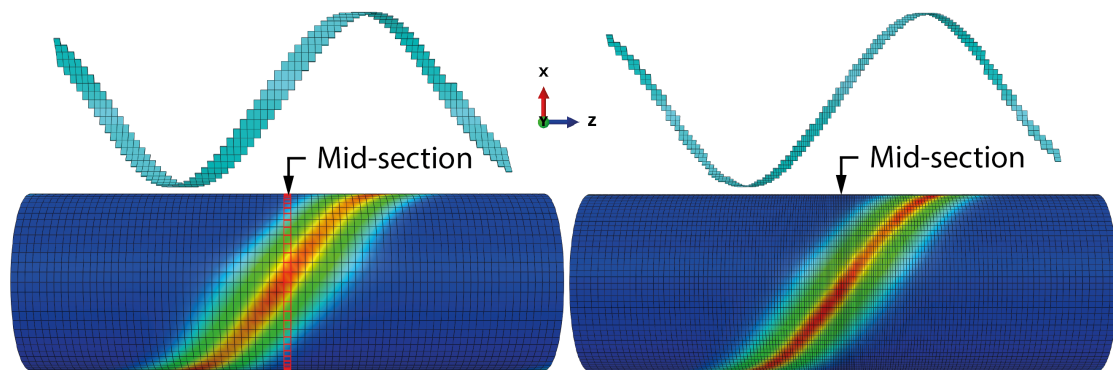


**Figure 6.9:** Visualization of the fiber tensile stress in layer 1 for a 10 mm gap in layer 21 for the gap tool using the defect layer method (left) and the biased mesh method (right). The contour colors represent the stress value with red and blue being the high and low (or zero) values, respectively.

### 6.3.3 Biased mesh method

If the element size of the normal mesh method becomes smaller, the saw-tooth behavior diminishes, but the computational costs increase. An alternative is to use a biased mesh (Figure 6.9 on the right), in which the elements vary in size in the longitudinal direction. As the interest is in the mid-section of the TCP, here the element size is small and the size increases towards the end of the TCP. With this method, the aspect ratio corresponding to the winding angle cannot be met, but as multiple small elements are within the longitudinal gap direction in the mid-section, there are no pronounced stress peaks in the response. In the far field, the element size increases and the rough gap definition causes stress peaks. However, as the interest is in the mid-section, this is of no concern.

### 6.3.4 Results

The three discussed methods have all been used in the assessment of different gap widths in layer 21, similar to the assessment in Section 3.3.5. For the normal mesh method, mesh 2 was used, as this mesh showed a good agreement with a significant reduced computational time compared with mesh 5. Although for the defect layer method all considered mesh sizes showed a good agreement, mesh 3 was used to be conservative in having elements small enough to assess gap widths smaller than 10 mm. For the biased mesh, a single mesh type was considered, such that multiple elements were present within the gap at the mid-section of the TCP.

In Figure 6.10 the gap assessment of the three methods are shown and superimposed with the results obtained using submodeling. In general the methods show a good agreement. However, the normal mesh underestimates the effect of a gap for a gap of 30 mm. This is due to the fact that for certain gap widths, the element centroids can be just outside the gap area and therefore the whole elements are considered to be defect free, as discussed before. For this method to work, after the script has run, it should be checked manually if the amount of elements in the gap section represents the correct gap width. Without this manual check the method is unreliable. Both the defect layer method and the biased mesh show a good agreement with the submodel results. For the smaller gaps (<4 mm), the biased mesh starts to divert more from the submodel results compared with the defect layer method. By further decreasing the element size of the biased mesh it is expected the agreement will be improved. However, for the used mesh size the computational costs are already nearly double the costs of the defect layer method.

With this, it is demonstrated that the defect layer method can be effectively used for the assessment of gaps, while limiting the computational costs.

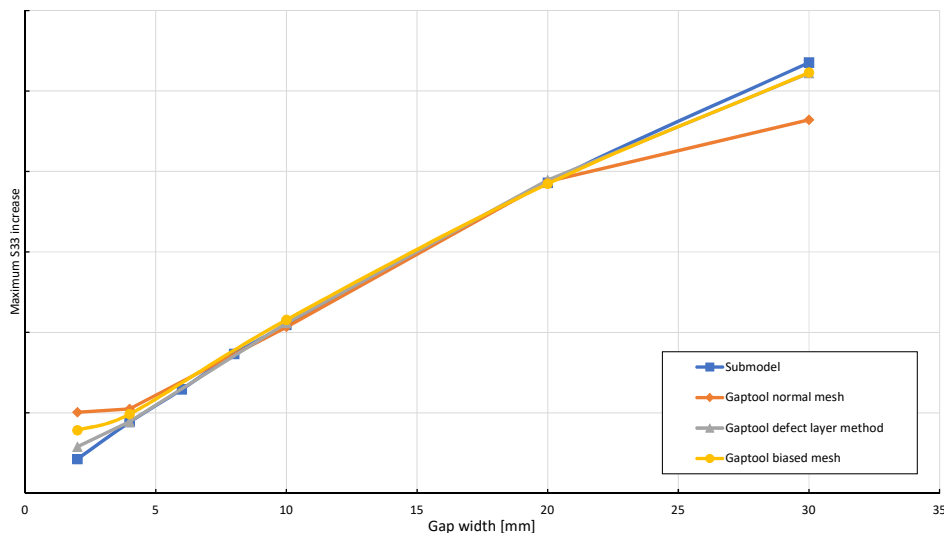


**Figure 6.10:** Comparison of FE modeling results using the proposed gap tool for the increase in the maximum fiber tension stress for different gap widths in layer 21 using three different methods.

## 6.4 Use of the proposed gap assessment tool

With the proposed gap assessment tool, the global TCP performance can be predicted in the presence of gaps. In this study the focus was on internal pressure, as this load case was predicted to be critical for the described TCP considering gaps. With this tool, the effect of gaps can also be predicted for different load cases. A different load case of interest considering gaps is external pressure, as failure is either determined by buckling of the TCP or fiber compression failure. An external pressure load case, similar as in Section 3.4, was performed using the proposed gap tool. Gap widths varying from 10 to 30 mm in layer 21 were considered and the results are shown in Figure 6.11. The (global) buckling pressure was for all cases equal and only minor differences in the maximum fiber compression stress were observed, which were primarily due to step size discrepancies in the last increments.

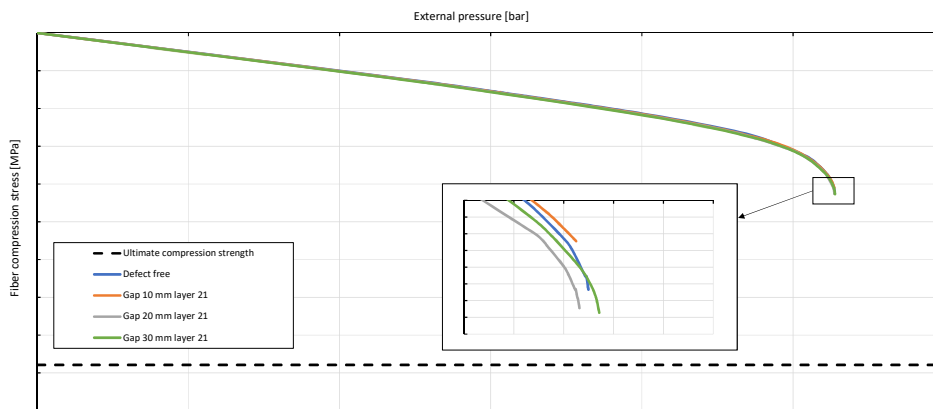


**Figure 6.11:** Fiber compression stress for a TCP subjected to external pressure predicted with the proposed gap tool.

In the design of a new TCP, this tool can either be used to determine what gap sizes may be allowed in production for a certain performance margin, or to define what safety margin is required to be able to allow gaps of certain sizes.

For example, if a TCP is designed with a strength margin for manufacturing defects being a certain value  $x$ , a single gap with a certain width, or multiple stacked gaps having smaller widths are allowed at one longitudinal position. Based on the maximum fiber stress increase for internal pressure obtained by the proposed gap tool, as shown in Figure 6.12, four examples of gaps that may be allowed in the 40-layer TCP considered in this study are shown in Figure 6.13. In **example 1**, a single large gap of 30 mm consumes most of the safety margin at once. The second, smaller gap, has its own safety margin because this gap is located in a layer having the opposite winding angle of the layer having the larger gap. Multiple gaps are stacked in **example 2**, which multiplies the stress increase. Four stacked gaps in the layers having the same winding angle would exceed the safety margin, but as only three out of four are within the layers having the same orientation, they may be allowed. Multiple gaps located side by side act as a single large gap having a width equal to the sum of the gaps. In **example 3**, four 5 mm gaps at different positions are located side by side, having an effect equal to a single 20 mm gap. In combination with a 10 mm gap, the total fiber stress increase is equal to the set safety margin. A more complex configuration is shown in **example 4**, in which the stacked gaps on the left, middle and right all consume the safety

margin. Because the stacked gaps in the middle are in the layers having the opposite winding angles with respect to the gaps on the left and right, and the longitudinal distance between the gaps on the left and right is large enough to not interfere (60 mm), this configuration may also be allowed.

The small stress increase in the layers having the opposite winding angle as the gap layer, are not taken into account in these examples. It is therefore recommended to always add an additional safety margin if this is expected.

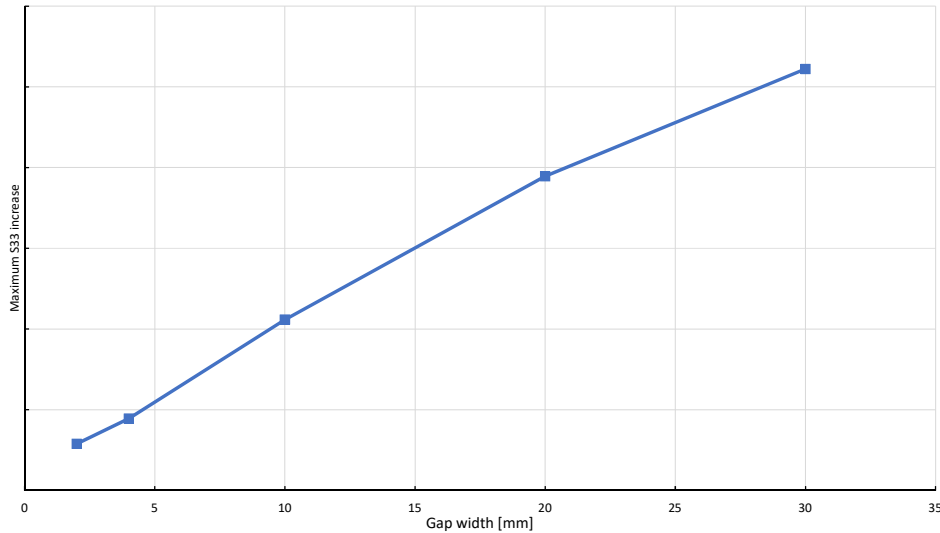


**Figure 6.12:** Predicted increase in the maximum fiber tension stress for different gap widths in layer 21 using the proposed gap tool.

However, the tool has its limits. As the element edges of the gap sets represent a saw-tooth, stress concentrations at these points can be present in the layers close to the gap. These peaks can be ignored, as it is known in which layer the largest stress will be located, which is, in this case, in layer 1. Due to this, and the fact the layer of interest and the gap layer may not be within one element, the tool can only be used to assess the response of gaps in layers which are not close to the critical layer. This means the slightly more pronounced effect of a gap in layer 3, which is the second highest loaded layer having the same winding angle as the critical layer, can not be assessed using the proposed tool. It is therefore recommended to use a safety factor or an additional safety margin to bridge this difference. If the effect of this layer is of primary interest, a submodeling technique as discussed in Section 3.3.3 can be used.

## 6.5 Conclusions

It is demonstrated that the current gap calculator underestimates the performance decrease in TCPs and therefore needs to be revised. A tool is proposed, based on a Python script, which can be used in Abaqus for the assessment of the effect of gaps. Based on an element selection method, three methods have been studied: 1) using a normal mesh, 2) a normal mesh combined with the defect layer method and 3) a biased mesh. It was found that the



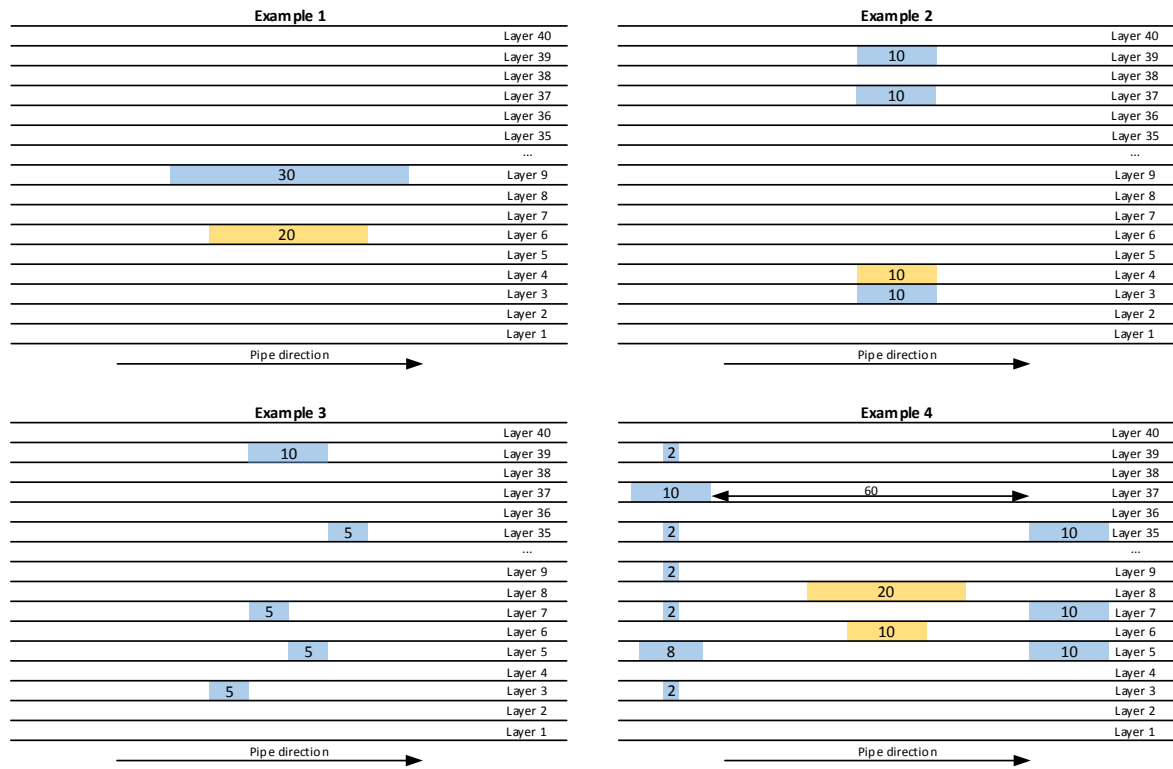


**Figure 6.13:** Four schematic representations of the cross-section of a TCP laminate in the longitudinal direction with gaps in the  $+\phi$  layers (blue) and  $-\phi$  layers (orange). Dimensions in mm.

second method, in which the element material is reduced based on the percentage of the element in the gap provides an accurate assessment, while limiting the computational costs. The tool can be used in the design process of a TCP to determine the required safety margin or the allowable gap geometry and occurrences.



# Conclusions and recommendations

The aim of this study was to obtain a thorough understanding of the effects of defects in TCPs. Gaps and voids were identified as critical defect types in the production of TCPs, as these two defect are most frequently observed. The following research question was formulated:

*How is the mechanical performance of thermoplastic composite pipes affected by manufacturing-induced gaps and voids and what substantiated criteria can be established for these defects to be allowed in production?*

## 7.1 Conclusions

### 7.1.1 Effect of gaps on the performance of TCPs

Gaps in composite structures, which are areas filled with matrix material, soften the structure and reduce its strength and stiffness. For flat laminates having gaps, the fiber stress is evenly redistributed over the remaining laminate, yielding a linear relationship between the gap size and performance reduction, in which in terms of strength, gaps only have an effect in the fiber direction. To study the effect of gaps on the mechanical performance of TCPs, an FE model was created and subjected to internal pressure. Helical sections, following the winding angle, were used to capture a gap accurately. In combination with a submodel technique the effect on lamina level was studied, leading to the following results:

- A gap provokes in general an equal stress increment in all layers having the same winding angle as the gap layer, with a slightly more pronounced increase in the first layer below the gap layer having the same winding angle.
- The increase in stress is linear proportional to the gap width.
- The stress increase multiplies with the amount of overlapping gaps, but rapidly diminishes when the longitudinal distance between gaps increases.

It is therefore concluded that the thickness position is only of importance if the gap layer is close to the critical layer (highest loaded layer). Therefore, the second most critical layer, having the same winding angle as the critical layer, is the most critical in having a gap. As the effect of a gap is dependent on the amount of layers in the same winding orientation, the effect is either smaller or larger for thicker and thinner pipes, respectively.

The used gap modeling technique was validated by tensile coupons with and without gaps, which were tested both virtually and experimentally. As a good agreement between the results of both was observed, it was concluded that the assessment results of gaps on TCPs can be considered correct.

As the effect of gaps depends on multiple factors, no universal criteria can be established. It was found that the current tool to assess the effect of gaps can be substantially improved and therefore a new gap assessment tool is proposed. For this tool, a Python script selects in a TCP Abaqus model the elements which are in the gap and by using the defect layer method [19] the area percentage of the elements in the gap are calculated and their material properties are reduced accordingly. The proposed tool allows for a computational inexpensive and accurate assessment of gaps and can be used as an integral part of the design process and contributes to an improved integrity management system.

### 7.1.2 Effect of voids on the performance of TCPs

A void in a TCP is defined as a delamination, which is the separation of two adjacent layers in the layup of a composite structure. The possibility of the delaminating layer to buckle causes the compression strength of a structure to reduce. In literature was found that size and thickness position are the most prominent factors playing a role in delamination failure. In the study of the effect of voids in TCPs, two load cases were considered: external pressure and lateral crushing. Voids were modeled as delaminations, in which the defect free TCP was connected using tie constraints and a contact condition was established between the delaminating layer and substrate, allowing the delaminating layer to open.

For external pressure a delamination with an exceptional large dimension (30 x 200 mm) was modeled at different thickness locations. A non-linear buckling analysis was performed to predict the buckling load and the corresponding maximum compression stress in the fibers. External pressure causes the delamination surfaces to be pressed onto each other and therefore differences in buckling load were negligible and only minor increases in maximum fiber stress were observed, which were still 50 % below the allowable stress. It is concluded that voids in TCPs do not have an effect on the mechanical performance in terms of external pressure.

A TCP with and without delaminations was tested both virtually and experimentally in lateral crushing, in which the through thickness matrix properties are of importance. For a TCP having a delamination, an onset of delamination growth was observed at a significant lower load compared with the onset of delamination formation in a defect free TCP. In addition, the stiffness was reduced. With FE modeling the correct stiffness response can be predicted, but a correct failure indicator to determine the onset of delamination growth is missing. It is concluded that the onset of delamination growth is determined by the material fracture toughness and cannot be predicted using the value of the global stress field in the TCP when a defect free specimen fails.

## 7.2 Recommendations

Based on the present study, recommendations are made in order to improve the TCP design. Recommendations are also made for future studies and to improve the accuracy in the defect analyses. These recommendations can be used as input for the improvement of the structural integrity management system.

### **Full scale TCP test with gaps**

The gap modeling used on TCP level is based on the validation on coupon level, as full scale testing is time consuming and expensive. In this study the assessment of gaps on TCP level is done using predictive engineering. It is however recommended to ultimately validate if the results reflect reality the by testing TCPs in which the gap size and occurrence are fully quantified to allow correlation with the model.

### **Long term gap assessment**

This study is the first step in an improved integrity management system for TCPs and serves therefore as a basis from which to investigate further. The short term static behavior is assessed, leaving the long term effects for future research.

### **Reconsider the use of the current gap tool**

It is recommended to reconsider the use of the current gap tool, as mechanical performance predictions are found to be underestimated. The assumption that the fiber stress of a gap area is evenly redistributed over the width of the tape is found to be invalid, as the stress primarily redistributes through-the-thickness of the laminate.

### **Use of the proposed gap assessment tool in the design of a TCP**

The proposed tool for the analysis of gaps in TCPs can be used to either determine the size and amount of overlapping gaps before a certain safety margin is consumed, or based on the occurrences of gaps, a manufacturing margin can be defined. It is recommended to make a trade-off between the allowed gaps and the safety margin. If a small safety margin is used, the threshold for a gap width to be repaired is low, causing an increase in the amount of repairs and additional costs, while it may be more cost efficient to manufacture additional reinforcement layers to raise the gap allowable threshold.

Although the proposed tool is built in a way it can be easily adopted for different materials, TCP geometries and temperatures, care should be taken to adopt and use the tool. It is recommended to validate the tool for other material combinations by means of virtual and experimental testing.

### **Improve proposed gap assessment tool**

As the proposed tool is currently only used for research purposes, the effective use in the daily operation and the design of a TCP has not been done. It is possible that adjustments are

required for the tool to work in a more convenient way. Ultimately, more options in the tool can be automated, such as the manual input of the longitudinal element length or automatic meshing of a TCP model with an element aspect ratio corresponding to the winding angle. Moreover, the tool would be even more powerful if it would be able to assess the effect of a gap in the gap critical layer, which is layer 3 in the considered TCP.

#### **Lateral crushing tests for a TCP with a delamination**

In the experimental lateral crushing results, the onset of delamination growth for specimens with a 13 and 25 mm delamination was obtained from the load displacement curve, as a clear drop in load was present. However, for the 42 mm delamination the onset of delamination was less pronounced in the load displacement curve and therefore manually extracted from video recordings. The determination of the onset is difficult and prone to errors. It is therefore recommended to use a different technique, for example using acoustic emission sensors, to determine the onset of delamination growth.

#### **Delamination modeling**

Further research on the modeling of delaminations in a lateral crushing load case is recommended, as the onset of delamination cannot be predicted based on the global stress field when a defect free TCP fails and a correct failure indicator is missing. The material fracture toughness and fracture mechanics are options to study for this.

#### **Structural integrity in the lateral crushing behavior**

An onset of delamination growth was observed in the experimental lateral crushing tests. However, despite the presence of a single (growing) delamination, the ultimate load carrying capacity of the TCP did not change. It is recommended to further investigate this phenomenon, as a single delamination can possibly be present without compromising the structural integrity.

---

## References

- [1] A. Madeo. Fibrous composite reinforcements. In A. Madeo, editor, *Generalized Continuum Mechanics and Engineering Applications*, pages 19–47. Elsevier, 2015. ISBN 978-1-78548-032-4. doi: 10.1016/B978-1-78548-032-4.50002-4.
- [2] C. Ballinger. Structural frp composites. *Civil Engineering - ASCE*, 60(7):63–65, 1990.
- [3] G. Qi, D. Qi, N. Ding, and X. Shao. Hydrostatic Experimental Study and Failure Mechanism of Glass Fiber Reinforced Thermoplastic Pipes Used for Oilfields. In Y. Han, editor, *Advances in Materials Processing*, pages 1133–1141. Springer Singapore, Singapore, 2018. ISBN 978-9-81130-106-3, 978-9-81130-107-0. doi: 10.1007/978-981-13-0107-0\_108.
- [4] D. Picard, W. Hudson, L. Bouquier, G. Dupupet, and I. Zivanovic. Composite Carbon Thermoplastic Tubes for Deepwater Applications. In *Offshore Technology Conference*, Houston, Texas, U.S.A., 2007. Offshore Technology Conference. doi: 10.4043/19111-MS.
- [5] F. Taheri. Advanced fiber-reinforced polymer (FRP) composites for the manufacture and rehabilitation of pipes and tanks in the oil and gas industry. In *Advanced Fibre-Reinforced Polymer (FRP) Composites for Structural Applications*, pages 662–704. Elsevier, 2013. ISBN 978-0-85709-418-6. doi: 10.1533/9780857098641.4.662.
- [6] C. Soutis. Fibre reinforced composites in aircraft construction. *Progress in Aerospace Sciences*, 41(2):143–151, 2005. ISSN 0376-0421. doi: 10.1016/j.paerosci.2005.02.004.
- [7] E. Shehab, W. Ma, and A. Wasim. Manufacturing Cost Modelling for Aerospace Composite Applications. In J. Stjepandić, G. Rock, and C. Bil, editors, *Concurrent Engineering Approaches for Sustainable Product Development in a Multi-Disciplinary Environment*, pages 425–433. Springer London, London, 2013. ISBN 978-1-44714-425-0, 978-1-44714-426-7. doi: 10.1007/978-1-4471-4426-7\_37.
- [8] R. Talreja. Manufacturing defects in composites and their effects on performance. In *Polymer Composites in the Aerospace Industry*, pages 99–113. Elsevier, 2015. doi: 10.1016/b978-0-85709-523-7.00005-0.
- [9] B. Farahmand. *Virtual Testing and Predictive Modeling*. Springer, 2009.

- [10] DNVGL. DNVGL-ST-F119 Thermoplastic composite pipes standard, August 2018.
- [11] AOG. Design manual thermoplastic composite pipe. Internal company document - confidential, October 2018.
- [12] Y. Bai and Q. Bai. Subsea pipelines. In *Subsea Engineering Handbook*, pages 919–940. Elsevier, 2019. doi: 10.1016/b978-0-12-812622-6.00031-2.
- [13] Engineering Toolbox. Tools and basic information for design, engineering and construction of technical applications, 2001. URL <https://www.engineeringtoolbox.com>.
- [14] K. Potter. Manufacturing defects as a cause of failure in polymer matrix composites. In *Failure Mechanisms in Polymer Matrix Composites*, Woodhead Publishing Series in Composites Science and Engineering, pages 26–52. Woodhead Publishing, 2012. ISBN 978-1-84569-750-1. doi: 10.1533/9780857095329.1.26.
- [15] F. Heinecke, W. Brink, and T. Wille. Assessing the structural response of automated fibre placement composite structures with gaps and overlaps by means of numerical approaches. *ICCM International Conferences on Composite Materials*, July 2015.
- [16] Statistics How To. Binomial distribution: Formula, what it is and how to use it, 2019. URL <https://www.statisticshowto.datasciencecentral.com/probability-and-statistics/binomial-theorem/binomial-distribution-formula/>.
- [17] D.S. Cairns, L.B. Ilcewicz, and T. Walker. Response of automated tow placed laminates to stress concentrations. *Third NASA Advanced Composites Technology Conference*, 1 (2):649–663, January 1993.
- [18] A.W. Blom, C.S. Lopes, P.J. Kromwijk, Z. Gürdal, and P.P. Camanho. A theoretical model to study the influence of tow-drop areas on the stiffness and strength of variable-stiffness laminates. *Journal of Composite Materials*, 43(5):403–425, January 2009. doi: 10.1177/0021998308097675.
- [19] K. Fayazbakhsh, M.A. Nik, D. Pasini, and L. Lessard. Defect layer method to capture effect of gaps and overlaps in variable stiffness laminates made by automated fiber placement. *Composite Structures*, 97:245–251, February 2013. doi: 10.1016/j.compstruct.2012.10.031.
- [20] H. Ghayoor, C.C. Marsden, S.V. Hoa, and A.R. Melro. Numerical analysis of resin-rich areas and their effects on failure initiation of composites. *Composites Part A: Applied Science and Manufacturing*, 117:125–133, February 2019. doi: 10.1016/j.compositesa.2018.11.016.
- [21] E.M. Jensen, D.A. Leonhardt, and R.S. Fertig. Effects of thickness and fiber volume fraction variations on strain field inhomogeneity. *Composites Part A: Applied Science and Manufacturing*, 69:178–185, February 2015. doi: 10.1016/j.compositesa.2014.11.019.
- [22] C. Kassapoglou. *Modeling the Effect of Damage in Composite Structures*. Aerospace Series. John Wiley & Sons Ltd, 2015. ISBN 978-1-11901-321-1.



- [23] C. Larco, R. Pahonie, and I. Edu. The effects of fibre volume fraction on a glass-epoxy composite material. *INCAS BULLETIN*, 7(3):113–119, September 2015. doi: 10.13111/2066-8201.2015.7.3.10.
- [24] B. Khan, K. Potter, and M.R. Wisnom. Simulation of process induced defects in resin transfer moulded woven carbon fibre laminated and their effect on mechanical behaviour. *International Conference on Flow Processes in Composite Materials*, 2006.
- [25] K. Potter. Understanding the origins of defects and variability in composites manufacture. *ICCM International Conferences on Composite Materials*, January 2009.
- [26] A. Sawicki and P. Minguett. The effect of intraply overlaps and gaps upon the compression strength of composite laminates. In *39th AIAA/ASME/ASCE/AHS/ASC Structures, Structural Dynamics, and Materials Conference and Exhibit*. American Institute of Aeronautics and Astronautics, April 1998. doi: 10.2514/6.1998-1786.
- [27] K. Croft, L. Lessard, D. Pasini, M. Hojjati, J. Chen, and A. Yousefpour. Experimental study of the effect of automated fiber placement induced defects on performance of composite laminates. *Composites Part A: Applied Science and Manufacturing*, 42(5): 484–491, May 2011. doi: 10.1016/j.compositesa.2011.01.007.
- [28] JP. Marrouzé, J. Housner, and F. Abdi. Effect of manufacturing defects and their uncertainties on strength and stability of stiffened panels. *ICCM International Conferences on Composite Materials*, 2013.
- [29] M. Broggi and G.I. Schuëller. Efficient modeling of imperfections for buckling analysis of composite cylindrical shells. *Engineering Structures*, 33(5):1796–1806, May 2011. ISSN 0141-0296. doi: 10.1016/j.engstruct.2011.02.019.
- [30] M.W. Hilburger and J.H. Starnes. Effects of imperfections of the buckling response of composite shells. *Thin-Walled Structures*, 42(3):369–397, March 2004. ISSN 0263-8231. doi: 10.1016/j.tws.2003.09.001.
- [31] A.C. Garg. Delamination—a damage mode in composite structures. *Engineering Fracture Mechanics*, 29(5):557–584, January 1988. doi: 10.1016/0013-7944(88)90181-6.
- [32] S. Abrate. Impact on laminated composite materials. *Applied Mechanics Reviews*, 44(4): 155–190, April 1991. ISSN 0003-6900. doi: 10.1115/1.3119500.
- [33] M.J. Pavier and M.P. Clarke. Experimental techniques for the investigation of the effects of impact damage on carbon-fibre composites. *Composites Science and Technology*, 55(2):157–169, January 1995. doi: 10.1016/0266-3538(95)00097-6.
- [34] G.J. Simitses, S. Sallam, and W.L. Yin. Effect of delamination of axially loaded homogeneous laminated plates. *AIAA Journal*, 23(9):1437–1444, September 1985. doi: 10.2514/3.9104.
- [35] Z.Q. Chen and G.J. Simitses. Delamination buckling of pressure-loaded, cross-ply, laminated cylindrical shells. *Zeitschrift Angewandte Mathematik und Mechanik*, 68:491–501, 1988. doi: 10.1002/zamm.19880681007.

- [36] G.J. Simitses, Z.Q. Chen, and S. Sallam. Delamination buckling of cylindrical laminates. *Thin-Walled Structures*, 11(1-2):25–41, January 1991. doi: 10.1016/0263-8231(91)90009-8.
- [37] G.A. Kardomateas and C.B. Chuch. Thin film modeling of delamination buckling in pressure loaded laminated cylindrical shells. *AIAA Journal*, 30(8):2119–2123, August 1992. doi: 10.2514/3.11189.
- [38] B. Prabu, N. Rathinam, R. Srinivasan, and K.A.S. Naarayan. Finite element analysis of buckling of thin cylindrical shell subjected to uniform external pressure. *Journal of Solid Mechanics*, 1, January 2009.
- [39] H.A. Ameen and A.H. Abood. Study the stability of composite laminated thin cylindrical shell with stiffeners. *Iraqi journal of mechanical and material engineering*, 10(2):234–244, 2010.
- [40] M. Bak. Nonlinear buckling analysis using workbench v15. online, 2014.
- [41] M. Barski, A. Muc, P. Pastuszak, and A. Bondyra. Numerical and Experimental Buckling and Post - Buckling Analysis of Composite Cylindrical Panel with Delamination. *Applied Mechanics and Materials*, 477-478:39–42, December 2013. ISSN 1662-7482. doi: 10.4028/www.scientific.net/AMM.477-478.39.
- [42] S.A. Sajjady, S. Rahnama, M. Lotfi, and R. Nosouhi. Numerical analysis of delamination buckling in composite cylindrical shell under uniform external pressure: Cohesive element method, 2017.
- [43] G.J. Short, F.J. Guild, and M.J. Pavier. The effect of delamination geometry on the compressive failure of composite laminates. *Composites Science and Technology*, 61(14): 2075–2086, November 2001. doi: 10.1016/s0266-3538(01)00134-8.
- [44] Y. Pekbey and O. Sayman. A Numerical and Experimental Investigation of Critical Buckling Load of Rectangular Laminated Composite Plates with Strip Delamination. *Journal of Reinforced Plastics and Composites*, 25(7):685–697, May 2006. ISSN 0731-6844, 1530-7964. doi: 10.1177/0731684406060566.
- [45] M. Zor. Determination of Critical Width of Multiple Delamination in Laminated Composite Plate Under Buckling Load. *Journal of Reinforced Plastics and Composites*, 28(3): 305–316, February 2009. ISSN 0731-6844, 1530-7964. doi: 10.1177/0731684407084244.
- [46] M. Gaiotti, C.M. Rizzo, K. Branner, and P. Berring. Finite elements modeling of delaminations in composite laminates. *Advances in Marine Structures - Proceedings of the 3rd International Conference on Marine Structures, Marstruct 2011*, pages 133–139, March 2011. doi: 10.1201/b10771-18.
- [47] R.G. Wang, L. Zhang, W.B. Liu, J. Zhang, X.D. Sui, D. Zheng, and Y.F. Fang. Numerical analysis of delamination behavior in laminated composite with double delaminations embedded in different depth positions. *Polymers and Polymer Composites*, 19:213–222, March 2011. doi: 10.1177/0967391111019002-325.

- [48] S. El-Sayed and S. Sridharan. Delamination buckling and growth in rings under pressure. *Journal of Engineering Mechanics*, 126, October 2000. doi: 10.1061/(ASCE)0733-9399(2000)126:10(1033).
- [49] A. Tafreshi. Efficient modelling of delamination buckling in composite cylindrical shells under axial compression. *Composite Structures*, 64(3-4):511–520, June 2004. doi: 10.1016/j.compstruct.2003.09.050.
- [50] A. Tafreshi. Delamination buckling and postbuckling in composite cylindrical shells under external pressure. *Thin-Walled Structures*, 42(10):1379–1404, October 2004. doi: 10.1016/j.tws.2004.05.008.
- [51] A. Tafreshi. Delamination buckling and postbuckling in composite cylindrical shells under combined axial compression and external pressure. *Composite Structures*, 72(4):401–418, April 2006. doi: 10.1016/j.compstruct.2005.01.009.
- [52] A. Tafreshi. Delamination buckling of composite cylindrical shells. In S. Sridharan, editor, *Delamination Behaviour of Composites*, Woodhead Publishing Series in Composites Science and Engineering, pages 586–617. Woodhead Publishing, 2008. ISBN 978-1-84569-244-5. doi: 10.1533/9781845694821.5.586.
- [53] A. Tafreshi. Instability of delaminated composite cylindrical shells under combined axial compression and bending. *Composite Structures*, 82(3):422–433, 2008. ISSN 0263-8223. doi: 10.1016/j.compstruct.2007.01.021.
- [54] A. Tafreshi and C.G. Bailey. Instability of imperfect composite cylindrical shells under combined loading. *Composite Structures*, 80(1):49–64, 2007. ISSN 0263-8223. doi: 10.1016/j.compstruct.2006.02.031.
- [55] B. Prabu, A.V. Raviprakash, and A. Venkatraman. Parametric study on buckling behaviour of dented short carbon steel cylindrical shell subjected to uniform axial compression. *Thin-Walled Structures*, 48(8):639–649, August 2010. ISSN 0263-8231. doi: 10.1016/j.tws.2010.02.009.
- [56] J.F Doyle. *Nonlinear analysis of thin-walled structures: statics, dynamics, and stability*. Mechanical Engineering Series. Springer-Verlag New York, 2001. ISBN 978-0-387-95216-1.
- [57] M.J. Pavier and M.P Clarke. Finite element prediction of the post-impact compressive strength of fibre composites. *Composite Structures*, 36(1):141–153, 1996. ISSN 0263-8223. doi: 10.1016/S0263-8223(96)00073-6.
- [58] E.E. Theotokoglou. Behaviour of thick composite tubes considering of delamination. *Theoretical and Applied Fracture Mechanics*, 46(3):276–285, 2006. ISSN 0167-8442. doi: 10.1016/j.tafmec.2006.09.005.
- [59] J. Mistry, A.G. Gibson, and Y.-S. Wu. Failure of composite cylinders under combined external pressure and axial loading. *Composite Structures*, 22(4):193–200, January 1992. ISSN 0263-8223. doi: 10.1016/0263-8223(92)90055-H.
- [60] A.H.J. Nijhof. *Vezelversterkte kunststoffen: mechanica en ontwerp*. VSSD, 2005. ISBN 978-9-04072-484-8.

- 
- [61] AOG. Memo on continuum shell and continuum solid elements for pipe analysis. Internal company document - confidential, May 2012.
- [62] E.S.emih Perdahcioğlu and H.J.M. Geijselaers. Constitutive modeling of two phase materials using the mean field method for homogenization. *International Journal of Material Forming*, 4(2):93–102, November 2010. doi: 10.1007/s12289-010-1007-6.
- [63] Abaqus theory manual version 6.14, 2014.
- [64] S. Namdeo, H. De Boer, and J. De Kanter. A micromechanics approach towards delamination of thermoplastic composite pipe for offshore applications. In *International Conference on Composite Materials*, 2017.
- [65] R.G. Budynas and J.K. Nisbett. *Shigley’s Mechanical Engineering Design*. Mc Graw Hill, tenth edition, 2015.
- [66] D30 Committee. Test Method for Tensile Properties of Polymer Matrix Composite Materials. Technical report, ASTM International, 2017.
- [67] Delft Technical University. Flat hot plate press joos, 2007. URL <http://www.labs.tudelft.nl/index.php?action=instrument&id=237>.
- [68] AOG. AOG1407043 - TP 43 Effects of Defects. Internal company document - confidential, 2015.
- [69] AOG. AOG1407043TR001 - Crushing. Internal company document - confidential, 2015.
- [70] F17 Committee. Test method for determination of external loading characteristics of plastic pipe by parallel-plate loading. Technical report, ASTM International, 2008.
- [71] Brilliant.org. Dot product - distance between point and a line, 2020. URL <https://brilliant.org/wiki/dot-product-distance-between-point-and-a-line/>.

---

# Appendix A

---

## Thick walled cylinder stresses

This appendix shows the stresses and their distributions in thick walled cylinders for the static loads stated in Section 1.2.3. The formulas are retrieved from [13].

The stresses in a cylinder subjected to **internal pressure** depend on the internal pressure ( $P_i$ ), inner diameter, outer diameter and radial location ( $r$ ), as in Equation (A.1). At the inner diameter, tensile hoop stress and radial compression stress are at a maximum. Both stresses reduce in a non-linear manner towards the outer diameter, where the radial stress is equal to zero and the hoop stress can have a non-zero value. If the cylinder has a finite length, internal pressure also induce an axial stress in the cylinder, which is equal through-the-thickness (Figure A.1).

$$\sigma_r = P_i \frac{ID^2}{OD^2 - ID^2} \left( 1 - \frac{OD^2}{r^2} \right) \quad (\text{A.1a})$$

$$\sigma_h = P_i \frac{ID^2}{OD^2 - ID^2} \left( 1 + \frac{OD^2}{r^2} \right) \quad (\text{A.1b})$$

$$\sigma_a = P_i \frac{ID^2}{OD^2 - ID^2} \quad (\text{A.1c})$$

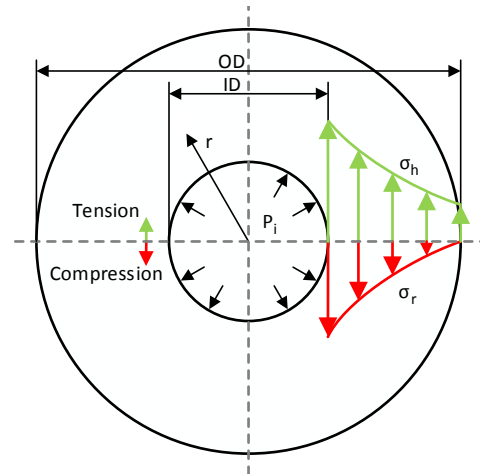


**Figure A.1:** Cylinder stresses due to internal pressure.

For an **external pressure** ( $-P_e$ ) load case, in which the minus indicates compression, the cylinder stresses depend on the same parameters as for internal pressure (Equation (A.2)). Hoop- and radial stresses behave in a similar non-linear manner through-the-thickness and

while the radial stress is largest at the outer diameter, the hoop stress reaches its maximum at the inner diameter. Axial compression stress is present if the cylinder has a finite length (Figure A.2).

$$\sigma_r = -P_e \frac{OD^2}{OD^2 - ID^2} \left( 1 - \frac{ID^2}{r^2} \right) \quad (\text{A.2a})$$

$$\sigma_h = -P_e \frac{OD^2}{OD^2 - ID^2} \left( 1 + \frac{ID^2}{r^2} \right) \quad (\text{A.2b})$$

$$\sigma_a = -P_e \frac{OD^2}{OD^2 - ID^2} \quad (\text{A.2c})$$

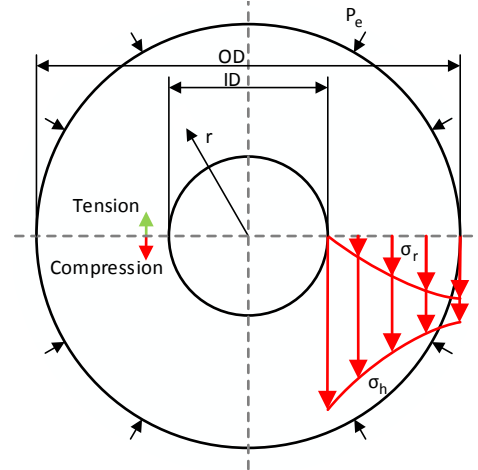


**Figure A.2:** Cylinder stresses due to external pressure.

A cylinder subjected to **bending** experiences both compression and tensile stresses. Compression stress is present between the neutral axis and the radius origin and tensile stresses on the outer side of the neutral axis. The distance to the neutral axis linearly determines the magnitude of both stresses, as shown in Figure A.3. The stresses are calculated according to the flexure formula in Equation (A.3), where  $M$  is the bending moment,  $y$  the distance from the neutral axis to the point of interest and  $I$  the moment of inertia.

$$\sigma_{a \text{ tension}} = \frac{My}{I} \quad (\text{A.3a})$$

$$\sigma_{a \text{ compression}} = -\frac{My}{I} \quad (\text{A.3b})$$

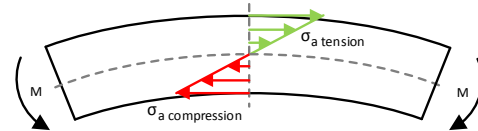


**Figure A.3:** Cylinder stresses due to bending.

**Axial tension** and **compression** loads purely introduce axial tensile- or compression stresses, respectively. These stresses are based on the applied load ( $F$ ) and cross-sectional area ( $A$ ) and are constant through-the-thickness (Equation (A.4) and Figure A.4).

$$\sigma_{a \text{ tension}} = \frac{F_a}{A} \quad (\text{A.4a})$$

$$\sigma_{a \text{ compression}} = \frac{-F_a}{A} \quad (\text{A.4b})$$

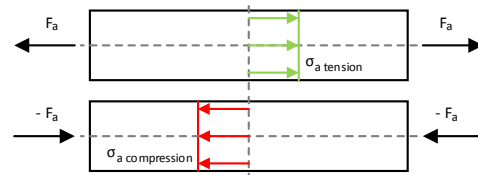


**Figure A.4:** Cylinder stresses due to axial tension (top) and compression (bottom) loading.

**Torsion** of a cylinder introduces shear stresses which depend on the amount of torque ( $T$ ), the radial position ( $r$ ) and the torsional constant ( $J$ ) (Equation (A.5)). The stresses vary linearly through-the-thickness, as in Figure A.5.

$$\tau = \frac{Tr}{J}$$

(A.5)

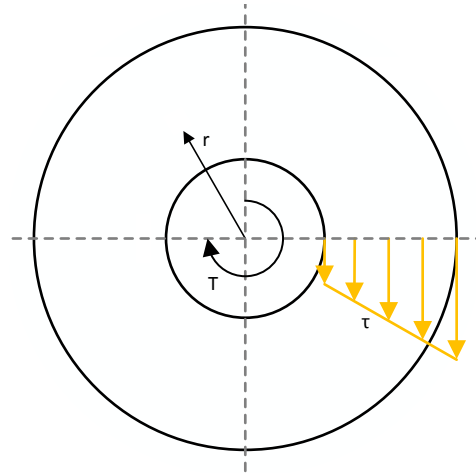


**Figure A.5:** Cylinder stresses due to torsion.





---

## Appendix B

---

# Gap assessment tool - Python code

```
1 from abaqus import *
2 from abaqusConstants import *
3 import numpy as np
4
5 #=====
6 # INPUT
7 #=====
8
9 myModel = 'model name'
10 myPart = 'part name'
11 myLayup = 'composite layup name'
12
13 gap_layer = 21          # change to the gap layer of interest
14 gapsize = 10           # change to the gap width of interest
15
16 mySet = ''             # Leave empty for automatic definition
17 ply_angle = ''        # Leave empty for automatic definition
18
19 layers_tot = 40        # Required if mySet and ply_angle are left empty
20 layers_per_elem = 4    # Required if mySet and ply_angle are left empty
21
22 elem_length = 5.559    # Change to avg. longitudinal element length
23 # with an element aspect ratio of 0.7 for a +-55 layup
24
25 #=====
26 # Print some information in the Abaqus message area to know what you are doing
27 #=====
28
29 print ' '
30 print '===== NEW SCRIPT ====='
31 print ' '
32 print 'Model          =', myModel
33 print 'Gaplayer        =', gap_layer
34 print 'Gap width        =', gapsize, 'mm'
35
36 #=====
```

```

37 # ORIENTATION GAP LAYER
38 # The orientation of the gap layer is extracted from the composite layup
39 #
40
41 if ply_angle == '':
42     ply_angle = mdb.models[myModel].parts[myPart].compositeLayups[myLayup]. \
43     plies[gap_layer - 1].orientationValue
44
45 print 'Ply angle of gap layer          =', ply_angle, 'deg'
46
47 #
48 # DETERMINE SET IN WHICH THE GAP LAYER IS LOCATED
49 # Can only be used if the an equal amount of layers is used in each set
50 #
51
52 if mySet == '':
53     for i in range(1, int(layers_tot / layers_per_elem + 1)):
54         if 0 < gap_layer <= (i * layers_per_elem):
55             mySet = 'R{}'.format(i)
56             break
57
58 print 'Set in which gap layer is present    =', mySet
59
60 #
61 # EXTRACT CENTROIDS OF ELEMENTS
62 # Calculate for all elements in a set the cartesian coordinate of the
63 # centroid by summing the coordinates in x, y and z for the nodes of an
64 # element and divide by the amount of nodes per element
65 #
66
67 centroid_car = []
68 elem_nr = []
69 for elem in mdb.models[myModel].parts[myPart].sets[mySet].elements:
70
71     n = len(elem.connectivity)
72     c = np.zeros(3)
73     for node in elem.connectivity:
74         c += mdb.models[myModel].parts[myPart].nodes[node].coordinates
75
76     c = c/n
77
78     centroid_car.append(c)
79
80     elem_nr.append(elem.label)
81
82 #
83 # CARTESIAN TO CYLINDRICAL COORDINATES
84 # x, y and z coordinates of all elements are transformed to r, theta and z
85 # in way that theta goes from 0 to 360 deg
86 # Cylindrical coordinates are stored in a dictionary with elem numbers
87 #
88
89 centroid_cyl = []
90 for cart in centroid_car:
91     x = cart[0]
92     y = cart[1]
93     z = cart[2]

```

```

94
95 r = np.sqrt(x**2 + y**2)
96 t = np.arctan(y / x)
97 z = z
98
99 if x < 0:
100 t += np.pi
101
102 if x > 0 and y < 0:
103 t += np.pi * 2
104
105 cyl_coord = [r,t,z]
106 centroid_cyl.append(cyl_coord)
107
108 element_dic = dict(zip(elem_nr, centroid_cyl))
109
110 # =====
111 # POINT TO LINE DISTANCE
112 # This function determines the shortest distance from a point to a line in
113 # 2D using the dot product
114 # line equation y = c1 x + c2
115 # =====
116
117 def distance(x,y,c1,c2):
118 a = c1
119 b = -1.
120 c = c2
121
122 d = np.abs(a*x+b*y+c)/np.sqrt(a**2+b**2)
123
124 return d
125
126 # =====
127 # NODES WHICH CENTROIDS ARE LOCATED IN THE GAP
128 # The coordinates of the centroids are transformed to 2D (z (x-axis) and
129 # r*theta (y-axis)) and the distance to the winding (which becomes a
130 # straight line in this 2D case) is calculated. The output are the element
131 # numbers of which the centroid is within the gapsize area
132 # =====
133
134 AR      = 1. / np.tan(np.deg2rad(ply_angle))      # Element aspect ratio
135 lcir    = elem_length / AR                       # Element circumferential length
136 x       = 0.5 * np.sqrt(elem_length**2 + lcir**2) # Distance node - centroid
137 y       = np.sin(np.deg2rad(180 - 2 * ply_angle)) * x
138 # Distance node - perpendicular to the element diagonal
139
140 gap_50_dist = gapsize / 2.
141 gap_100_dist = gap_50_dist - y
142 gap_90_dist = gap_50_dist - 0.4 * y
143 gap_80_dist = gap_50_dist - 0.3 * y
144 gap_70_dist = gap_50_dist - 0.2 * y
145 gap_60_dist = gap_50_dist - 0.1 * y
146 gap_40_dist = gap_50_dist + 0.1 * y
147 gap_30_dist = gap_50_dist + 0.2 * y
148 gap_20_dist = gap_50_dist + 0.3 * y
149 gap_10_dist = gap_50_dist + 0.4 * y
150 gap_00_dist = gap_50_dist + y

```

```
151
152 gap_all_elem = []
153 gap_100_elem = []
154 gap_90_elem = []
155 gap_80_elem = []
156 gap_70_elem = []
157 gap_60_elem = []
158 gap_50_elem = []
159 gap_40_elem = []
160 gap_30_elem = []
161 gap_20_elem = []
162 gap_10_elem = []
163
164 if ply_angle > 0:      # if a -theta layer is selected the helix orientation
165     orientation = 1    # should be multiplied by -1
166 else:
167     orientation = -1
168
169 for elem in element_dic:
170     z = element_dic[elem][2]
171     rt = element_dic[elem][0] * element_dic[elem][1]
172
173     circum = 2 * np.pi * element_dic[elem][0]
174
175     for i in range(0,3): # create lines, representing 3 windings
176         dist_to_gap = distance(z,rt,-np.tan(np.deg2rad(ply_angle)), i * \
177             orientation * circum + 275)
178
179     if dist_to_gap <= gap_00_dist:
180         gap_all_elem.append(elem)
181
182     if dist_to_gap <= gap_100_dist:
183         gap_100_elem.append(elem)
184
185     if gap_100_dist < dist_to_gap <= gap_90_dist:
186         gap_100_elem.append(elem)
187
188     if gap_90_dist < dist_to_gap <= gap_80_dist:
189         gap_90_elem.append(elem)
190
191     if gap_80_dist < dist_to_gap <= gap_70_dist:
192         gap_80_elem.append(elem)
193
194     if gap_70_dist < dist_to_gap <= gap_60_dist:
195         gap_70_elem.append(elem)
196
197     if gap_60_dist < dist_to_gap <= gap_50_dist:
198         gap_60_elem.append(elem)
199
200     if gap_50_dist < dist_to_gap <= gap_40_dist:
201         gap_50_elem.append(elem)
202
203     if gap_40_dist < dist_to_gap <= gap_30_dist:
204         gap_40_elem.append(elem)
205
206     if gap_30_dist < dist_to_gap <= gap_20_dist:
207         gap_30_elem.append(elem)
```

```
208
209 if gap_20_dist < dist_to_gap <= gap_10_dist:
210     gap_20_elem.append(elem)
211
212 if gap_10_dist < dist_to_gap <= gap_00_dist:
213     gap_10_elem.append(elem)
214
215 # =====
216 # CREATE SET WITH GAP NODES
217 # For each percentage of reinforcement in the gap area a set is created
218 # =====
219
220 setname0 = 'GapALL_{}mm'.format(gapsize)
221 mdb.models[myModel].parts[myPart].SetFromElementLabels(name=setname0, \
222     elementLabels=gap_all_elem)
223
224 setname1 = 'Reinforcement_0%_{}mm'.format(gapsize)
225 mdb.models[myModel].parts[myPart].SetFromElementLabels(name=setname1, \
226     elementLabels=gap_100_elem)
227
228 setname2 = 'Reinforcement_10%_{}mm'.format(gapsize)
229 mdb.models[myModel].parts[myPart].SetFromElementLabels(name=setname2, \
230     elementLabels=gap_90_elem)
231
232 setname3 = 'Reinforcement_20%_{}mm'.format(gapsize)
233 mdb.models[myModel].parts[myPart].SetFromElementLabels(name=setname3, \
234     elementLabels=gap_80_elem)
235
236 setname4 = 'Reinforcement_30%_{}mm'.format(gapsize)
237 mdb.models[myModel].parts[myPart].SetFromElementLabels(name=setname4, \
238     elementLabels=gap_70_elem)
239
240 setname5 = 'Reinforcement_40%_{}mm'.format(gapsize)
241 mdb.models[myModel].parts[myPart].SetFromElementLabels(name=setname5, \
242     elementLabels=gap_60_elem)
243
244 setname6 = 'Reinforcement_50%_{}mm'.format(gapsize)
245 mdb.models[myModel].parts[myPart].SetFromElementLabels(name=setname6, \
246     elementLabels=gap_50_elem)
247
248 setname7 = 'Reinforcement_60%_{}mm'.format(gapsize)
249 mdb.models[myModel].parts[myPart].SetFromElementLabels(name=setname7, \
250     elementLabels=gap_40_elem)
251
252 setname8 = 'Reinforcement_70%_{}mm'.format(gapsize)
253 mdb.models[myModel].parts[myPart].SetFromElementLabels(name=setname8, \
254     elementLabels=gap_30_elem)
255
256 setname9 = 'Reinforcement_80%_{}mm'.format(gapsize)
257 mdb.models[myModel].parts[myPart].SetFromElementLabels(name=setname9, \
258     elementLabels=gap_20_elem)
259
260 setname10 = 'Reinforcement_90%_{}mm'.format(gapsize)
261 mdb.models[myModel].parts[myPart].SetFromElementLabels(name=setname10, \
262     elementLabels=gap_10_elem)
263
264 reduced_set = list(elem_nr)
```

```
265 for elem in gap_all_elem:
266     reduced_set.remove(elem)
267
268     mdb.models[myModel].parts[myPart].SetFromElementLabels(name=mySet, \
269     elementLabels=reduced_set)
270
271 print 'Done :)'
```